

# REPORT DOCUMENTATION PAGE

AFRL-SR-AR-TR-04-

Public reporting burden for this collection of information is estimated to average 1 hour per response, including the time for reviewing instructional data needed, and completing and reviewing this collection of information. Send comments regarding this burden estimate or any other aspect of this burden to Department of Defense, Washington Headquarters Services, Directorate for Information Operations and Reports (0704-0188), 4302. Respondents should be aware that notwithstanding any other provision of law, no person shall be subject to any penalty for failing to provide a valid OMB control number. PLEASE DO NOT RETURN YOUR FORM TO THE ABOVE ADDRESS.

0350

1. REPORT DATE (DD-MM-YYYY) 06-25-2004		2. REPORT TYPE Final Technical		3. DATES COVERED (From - To) 01-01-2001 - 31-12-2003	
4. TITLE AND SUBTITLE  (U) Laser Diagnostics for Reacting Flows				5a. CONTRACT NUMBER	
				5b. GRANT NUMBER F49620-01-1-0145	
				5c. PROGRAM ELEMENT NUMBER 61102F	
6. AUTHOR(S)  Ronald K. Hanson				5d. PROJECT NUMBER 2308	
				5e. TASK NUMBER BV	
				5f. WORK UNIT NUMBER	
7. PERFORMING ORGANIZATION NAME(S) AND ADDRESS(ES)  Stanford University 651 Serra Street Stanford CA 94305				8. PERFORMING ORGANIZATION REPORT NUMBER	
9. SPONSORING / MONITORING AGENCY NAME(S) AND ADDRESS(ES) AFOSR/NA 4015 Wilson Boulevard Room 713 Arlington VA 22203-1954				10. SPONSOR/MONITOR'S ACRONYM(S)	
				11. SPONSOR/MONITOR'S REPORT NUMBER(S)	
12. DISTRIBUTION / AVAILABILITY STATEMENT  Approved for public release; distribution is unlimited					
13. SUPPLEMENTARY NOTES					
14. ABSTRACT Advanced optical diagnostic techniques relevant to propulsion were investigated. The techniques studied were based on laser spectroscopy, with emphasis on spectrally-resolved absorption and laser-induced fluorescence (LIF). Spectrally narrow, continuous wave (cw) lasers allowed innovative diagnostics based on spectral lineshapes, while pulsed lasers provided intense bursts of photons needed for techniques based on LIF. Accomplishments of note included: studies of fundamental ketone in support of PLIF imaging diagnostics for fuel vapor and temperature; fabrication of a high-pressure flat-flame burner and its use to develop quantitative strategies for PLIF imaging of NO and temperature in high-pressure combustion systems; the first observation of ultraviolet (UV) LIF of CO <sub>2</sub> ; continued development of a new imaging diagnostic based on infrared planar laser-induced fluorescence (IR PLIF); discovery of strong UV absorption by CO <sub>2</sub> at high temperatures and measurements of the absorption cross sections; investigations of the impact of UV CO <sub>2</sub> absorption on existing diagnostic strategies for NO; initial demonstrations of a new wavelength-multiplexed laser extinction diagnostic allowing measurements in multiphase fuel flows; and continued development of wavelength-multiplexed tunable diode laser absorption sensors and their application to measure temperature and species concentration in practical combustion environments, including scramjet and gas turbine combustor test rigs at the Air Force Research Laboratory Propulsion Directorate.					
15. SUBJECT TERMS Laser Diagnostics, Combustion, Propulsion, Absorption, High-Pressure, Fluorescence, Temperature					
16. SECURITY CLASSIFICATION OF:			17. LIMITATION OF ABSTRACT	18. NUMBER OF PAGES	19a. NAME OF RESPONSIBLE PERSON
a. REPORT Unclassified	b. ABSTRACT Unclassified	c. THIS PAGE Unclassified			Julian M. Tishkoff
			UL	79	19b. TELEPHONE NUMBER (include area code) (703) 696-8478

20040709 021

**Final Technical Report**

**LASER DIAGNOSTICS FOR REACTING FLOWS**

**Grant AFOSR F49620-01-1-0145**

**Prepared for**

**AIR FORCE OFFICE OF SCIENTIFIC RESEARCH**

**For the Period**

**January 1, 2001 to December 31, 2003**

**Submitted by**

**R. K. Hanson, Principal Investigator**

**HIGH TEMPERATURE GASDYNAMICS LABORATORY**  
**Mechanical Engineering Department**  
**Stanford University**

## Table of Contents

1.0	Introduction.....	3
2.0	Project Summaries.....	4
2.1.	Fuel tracer photophysics for quantitative PLIF .....	4
2.2	Quantitative LIF and PLIF measurements of in high pressure-flames.....	13
2.2.1	Strategies for quantitative NO LIF.....	14
2.2.2	Methods for LIF determination of T in high-pressure flames....	20
2.2.3	Quantitative imaging of NO in high-pressure flames.....	22
2.3	First observation of LIF and PLIF imaging of CO <sub>2</sub> .....	25
2.4	Infrared planar laser-induced fluorescence (IR-PLIF).....	29
2.5	UV absorption of CO <sub>2</sub> .....	38
2.5.1	UV absorption cross sections for CO <sub>2</sub> and H <sub>2</sub> O.....	39
2.5.2	A problem for NO LIF.....	43
2.5.3	An opportunity for temperature measurements.....	46
2.6	Multiphase diagnostics based on wavelength-multiplexed laser extinction..	52
2.7	2f spectroscopy for temperature measurements in combustion flows.....	61
3.0	Publications and Presentations.....	67
4.0	Personnel.....	75
5.0	Technology Transitions/Transfers .....	76
6.0	Inventions.....	78

## 1.0 Introduction

Advanced optical diagnostic techniques relevant to propulsion were investigated. The techniques studied were based on laser spectroscopy, with emphasis on spectrally-resolved absorption and laser-induced fluorescence (LIF). Laser sources included tunable cw near-infrared diode lasers and tunable (or fixed-wavelength) pulsed lasers operated at ultraviolet (UV) or infrared (IR) wavelengths. The cw lasers were spectrally narrow, allowing study of innovative diagnostics based on spectral lineshapes, while the pulsed lasers provided intense bursts of photons needed for techniques based on LIF. Accomplishments of note included: further experimentation and modeling on the fundamental photophysics of acetone, in support of planar laser-induced fluorescence (PLIF) imaging diagnostics for fuel vapor and temperature, and extension of these studies to 3-pentanone; development of a new high-pressure flat-flame burner and its use to study the high-pressure and high-temperature UV spectra of NO and O<sub>2</sub> as needed to enable PLIF imaging of these species in high-pressure combustion systems; the discovery of UV LIF of CO<sub>2</sub> and measurement of the first UV PLIF images of CO<sub>2</sub> in a high-pressure flame; continued development of a new imaging diagnostic based on infrared planar laser-induced fluorescence (IR PLIF), which offers first-time ability to monitor combustion species not accessible with established UV PLIF techniques; discovery of strong UV absorption by CO<sub>2</sub> and H<sub>2</sub>O at high temperatures and measurements of the absorption cross sections, which were enabled by a novel, rapid-response UV kinetic spectrograph; understanding the impact of UV CO<sub>2</sub> absorption on existing diagnostic strategies for NO and initial investigation of opportunities for new temperature diagnostic strategies using CO<sub>2</sub> absorption; initial development of a new wavelength-multiplexed laser extinction diagnostic allowing measurements in multiphase fuel flow; and continued development of wavelength-multiplexed tunable diode laser absorption sensors and their application to measure temperature and species in practical combustion environments, including scramjet and gas turbine combustor test rigs at Wright-Patterson AFB.



## 2.0 Project Summaries

### 2.1 Fuel Tracer Photophysics for Quantitative PLIF

Successful AFOSR-sponsored research on the photophysics of acetone has lead to a continuing program that investigates the fundamental photophysical properties of a range of molecules that are suitable for measuring flowfield properties in combustion-related applications. At the beginning of this grant, work was underway to examine the temperature, pressure, and excitation wavelength dependencies of the fluorescence of 3-pentanone, a member of the ketone family larger than acetone. In IC engine applications, 3-pentanone has been the tracer of choice because of its physical similarity to iso-octane. In general, it is also a better physical match for the heavier hydrocarbons that are frequently found in aeroengine fuels. Further, a slight increase in signal levels (~30%) over acetone may be possible due to a higher fluorescence quantum yield [2.1.1]. Despite its popularity, however, the absorption and fluorescence dependencies of 3-pentanone on various experimental conditions have not been understood fully, and thus it has been difficult to obtain quantitative results in PLIF applications. Results presented below concentrate on elucidating 3-pentanone's fundamental photophysical properties.

In addition to continuing 3-pentanone studies, we also have begun fundamental studies of toluene photophysics. As an aromatic, toluene's absorption and fluorescence behaviors are very different from the ketones, but it is attractive because it constitutes a significant fraction of several real fuels and exhibits the potential for straightforward fuel-air ratio imaging. Like 3-pentanone, however, data interpretation in practical systems is hindered by lack of basic knowledge of the fluorescence behavior under a range of relevant conditions. Results from absorption and fluorescence studies as functions of temperature and excitation wavelength are presented below as we begin an effort to remove this limitation. In addition, these results also suggest new ways in which multi-parameter imaging might be accomplished in complex flowfields.

#### Photophysics background

For ketones and aromatics, the fluorescence signal (in energy per unit volume) in the limit of weak excitation can be calculated from the following form of the fluorescence equation:

$$S_f = \eta_{opt} \frac{E}{hc/\lambda} n_{abs}(P, T) \sigma(\lambda, T) \phi(\lambda, P, T) \quad (2.1.1)$$

Here,  $\eta_{opt}$  is the efficiency of the collection optics,  $E$  is the laser fluence [ $\text{J}/\text{cm}^2$ ], and  $(hc/\lambda)$  is the energy [J] of a photon at the excitation wavelength  $\lambda$ . Quantities that vary with temperature, pressure, and composition are  $n_{abs}$ , the number density of absorbing molecules [ $\text{cm}^{-3}$ ];  $\sigma$ , the molecular absorption cross section of the tracer [ $\text{cm}^2$ ]; and  $\phi$ , the fluorescence quantum yield. The number density  $n_{abs}$  is proportional to  $\chi P / T$ , where  $\chi$  is the absorber mole fraction. The key to understanding the fluorescence signal in terms of temperature and pressure lies in the behavior of the photophysical properties,  $\sigma$  and  $\phi$ .

#### 3-pentanone

During the current funding period, we have further augmented our understanding of 3-pentanone photophysics by measuring the absorption spectrum at various temperatures,

the relative change in fluorescence with temperature, and the absolute value of the fluorescence quantum yield. We then formulated a fluorescence quantum yield model. Although highlights are given below, further details can be found in [2.1.3-2.1.5].

### Absorption

The near-UV absorption spectrum of shock-heated 3-pentanone is shown at a few temperatures in Fig. 2.1.1. Additional discrete points at 248, 266, and 308 nm come from laser excitation in a heated cell. At room temperature, 248 and 308 nm absorption are roughly equal, lying at the blue and red tails of the electronic system. As temperature increases, however, the overall strength of the system increases, and the peak of the spectrum shifts to the red. This results in nearly constant absorption at 248 and 266 nm, which are on the blue side of the peak, but a three-fold increase in absorption at 308 nm as temperature spans 300K to 1000K.

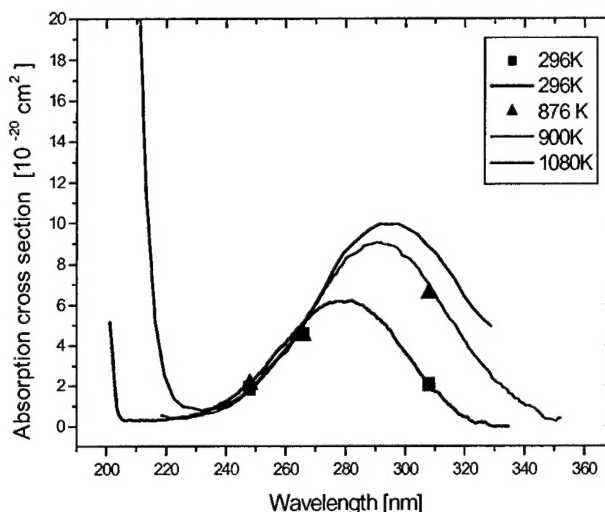


Fig. 2.1.1 Absorption spectrum of 3-pentanone between room temperature and 1000K.

Absorption cross sections for laser excitation and knowledge of the entire absorption spectrum are unique products of this research program and have not been studied previously in detail by the engineers who use 3-pentanone PLIF to investigate mixing in IC engines. Nonetheless, this knowledge is extremely useful during experimental design in practical applications. For example, optical thickness often plays a role in experiments with high pressures or locally high concentrations. While higher absorption leads to higher fluorescence signals, excessive laser attenuation can be detrimental. Also, the red shift of the absorption spectrum at elevated temperatures may warrant consideration when choosing the fluorescence collection bandwidth to avoid the effects of radiative trapping.

### Fluorescence

There are two interesting ways to map relative fluorescence to temperature. 1) In order to examine the molecule's basic behavior, one should look at the relative fluorescence signal per mole or per molecule. 2) In diagnostic applications, one may be more interested in how the mole or mixture fraction of the tracer varies in space, taking into account the change in overall number density due to temperature at constant pressure. Such interpretation requires examining the fluorescence per unit mole fraction, shown in Fig. 2.1.2.

When examining dependencies like the ones shown in Fig. 2.1.2, one may look for regions of high temperature sensitivity, like the 248 nm excitation, where good temperature measurements are possible in environments with constant seeding. Conversely, one may also look for regions of relative temperature independence to

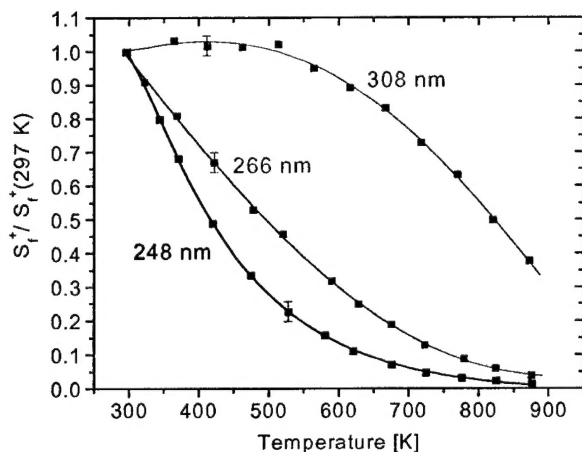


**Fig. 2.1.2** Relative 3-pentanone fluorescence signals per unit mole fraction as a function of temperature.  $p=1$  atm, nitrogen.

While reasonable uncertainty estimates are made possible with estimates of the temperature gradients and the curves of Fig. 2.1.2, a more complex experimental setup, utilizing two excitation wavelengths and two camera images, can quantify both the temperature ( $T$ ) and mixture fraction ( $\chi$ ) in complex flowfields (a technique developed under a previous AFOSR grant). For these  $T$ ,  $\chi$  measurements, the ratio of the fluorescence from two excitation wavelengths is a monotonic function of temperature, shown in Fig. 2.1.3. In general, one desires to use one temperature-sensitive and one temperature-insensitive wavelength in order to obtain best results; however, this desire must be balanced with the inherent tension between sensitivity and signal level. For example, while 248 nm excitation provides very high temperature sensitivity when combined with 308 nm excitation for 3-pentanone – even higher than the same scheme for acetone – the signal levels at high temperatures are only about 5% of room-temperature values at 700K (see Fig. 2.1.2). Thus, one may wish to augment signal levels at high temperatures by replacing 248nm with 266nm excitation, which has a higher absorption cross section and slightly less sensitivity to temperature (see Figs 2.1.1 and 2.1.2). For 3-pentanone, this scheme has roughly the same temperature sensitivity as the 308/248nm excitation combination for acetone, as shown in Fig. 2.1.3.

The 308/266nm technique has been demonstrated in an atmospheric, heated, turbulent ( $Re \approx 4000$ ) jet, shown in Fig. 2.1.4. 4.5% 3-pentanone in air was heated to about 650 K and injected through a nozzle into a coflow of 1.5% 3-pentanone/air at room temperature. (The stoichiometric mole fraction is about 3%.) Excited with 50 mJ laser

facilitate straightforward mole or mixture fraction imaging in non-isothermal environments. 308 nm excitation achieves this objective for temperatures ranging from 300K to about 500K.

### Multiparameter imaging

In the engine environments in which 3-pentanone PLIF has become popularized, flowfields may be neither uniformly seeded nor isothermal within the 300-500K limits of 308nm excitation; thus, good quantitative interpretation from a single image can be difficult.

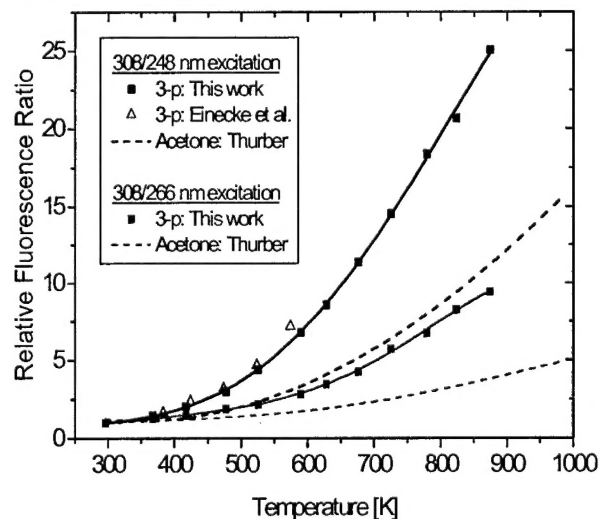


**Fig. 2.1.3** Fluorescence ratio from pairs of excitation wavelengths for 3-pentanone and acetone.

sheets, the fluorescence was captured with an interline-transfer, unintensified CCD camera. The laser pulses were separated by 1  $\mu$ s, a time scale short enough to minimize fluid motion between the two laser pulses. Resolution, given by RMS fluctuations in a small, uniform region of the flow, is about 15 K in temperature and 5% in jet fluid fraction. These results compare favorably with previously reported results using acetone in a similar configuration (7K and 2% resolution in a setup using 5 times as much ketone and heating to only 500K).

### **Fluorescence quantum yield**

In addition to the study of absorption and relative fluorescence as functions of temperature, we have developed an experimental method to quantify the fluorescence quantum yield (FQY) and its excitation wavelength dependence on an absolute basis by using nitrogen Rayleigh scattering as a calibration.

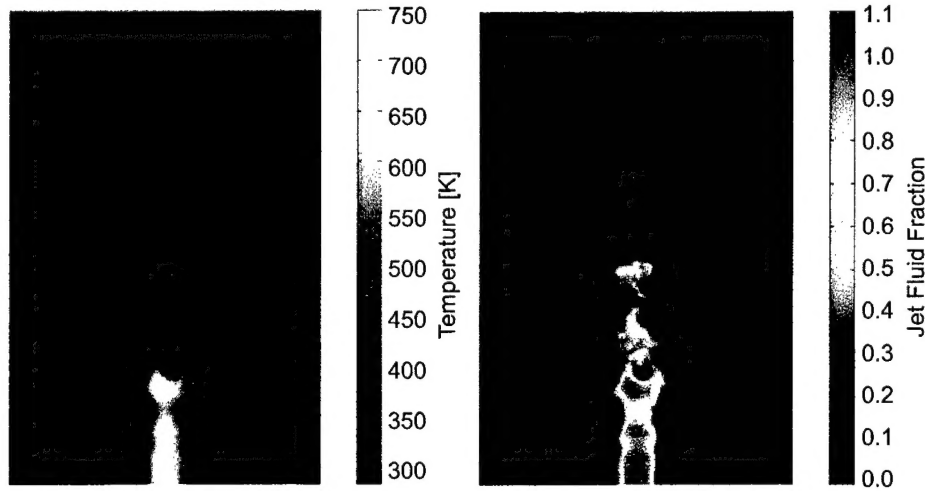


**Fig. 2.1.4** Images of a heated, turbulent jet using 308/266nm excitation of 3-pentanone. The jet core contains about 4.5% 3-pentanone while the co-flow contains 1.5%. RMS resolutions are 15K and 5% jet fluid fraction while peak temperatures are close to 670K (limited by capabilities of the heated jet facility).

Previous measurements of the FQY for the ketones have been made relative to other fluorescence standards and vary widely in the literature [2.1.1,2.1.5], leading to large uncertainties in the calculation of signal levels and modeling of the FQY. Furthermore, the excitation wavelength dependence of the FQY has been difficult to obtain in the past due to differing beam geometries and energy profiles among lasers.

The FQY ( $\phi$ ) for ketones and a variety of candidate tracers can be determined from the following equation:

$$\phi = \frac{S_{LIF} / (N_{ketone} I_{laser}^{LIF})}{S_{Ray} / (N_{N_2} I_{laser}^{Ray})} \frac{RSR_{Ray}}{RSR_{LIF}} \frac{d\sigma / d\Omega|_{90^\circ} 4\pi}{\sigma_{abs}} \quad (2.1.1)$$

where  $S_i / (N_i I_{laser}^i)$  is the signal per unit number density per unit laser energy from LIF or Rayleigh scattering,  $RSR_i$  is the relative spectral response of the detection system at either the LIF or Rayleigh wavelengths,  $d\sigma / d\Omega|_{90}$  is the differential Rayleigh scattering

cross section of nitrogen at ninety degrees from the linearly polarized laser's plane of vibration, and  $\sigma_{\text{abs}}$  is the absorption cross section of the tracer. Eqn. 2.1.1 shows that one can calculate the FQY by measuring 3 quantities on a fixed experimental setup with a given laser:

- 1) the energy-corrected fluorescence signal per ketone molecule (though not necessarily limited to ketones. This technique will work for a broad array of tracer candidates.)
- 2) the energy-corrected Rayleigh signal per nitrogen molecule (though not necessarily limited to nitrogen. Any molecule with a well-known Rayleigh cross section and measurable signal will work.)
- 3) The relative spectral response of the detection system.

One significant advantage of this technique is that Rayleigh scattering is well-founded in electromagnetic theory, and experimental measurements match very well with theoretical predictions. Thus, uncertainties in the Rayleigh cross sections, unlike the previously used fluorescence standards, are quite small. With careful measurements of items one through three above, the uncertainty in the FQY can be as low as 10-15%. Additionally, since the results are absolute using each laser excitation wavelength, experimental comparisons between laser wavelengths are now possible, and the relative fluorescence signals shown in Fig 2.1.3 now can be calibrated with a room temperature measurement at each wavelength.

The results of 3-pentanone FQY measurements made at room temperature are shown in Fig. 2.1.5 with the effect of added nitrogen up to 1 bar (the extent of the measurements at the time of this report). Qualitatively similar to the photophysical model developed for acetone and recently applied to 3-pentanone, the FQY is lowest for

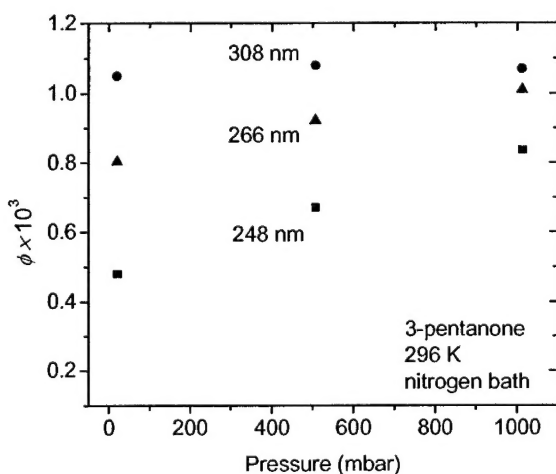


**Fig. 2.1.5** Absolute fluorescence quantum yield of 3-pentanone as a function of pressure at three excitation wavelengths.

is less than half of that, 0.11%.

The Rayleigh-calibrated FQY measurements provide a vital piece of the information needed to compare expected signal levels among tracers and the merits of

the shortest excitation wavelength. Also in accord with the model, the FQY appears to approach a high pressure limit, independent of the excitation wavelength. Previous measurements of the FQY indicated that there was no change with excitation wavelength and thus were a source of discrepancy between experimental data and our photophysical model [2.1.1]. This discrepancy seems to be resolved in favor of our model with these new data. The FQY in the high pressure limit was also in question, since previous measurements were largely uncertain. Whereas Hansen [2.1.1] assigned an FQY of about 0.25%, our measurement

various excitation/detection schemes. As an example, similar measurements using acetone resulted in an FQY about 70% of that for 3-pentanone when using 308 nm excitation at 1 bar; however, when 248 nm excitation was used, 3-pentanone's FQY was 2.5 times greater at 1 bar. As more tracers are explored for new types of measurements and applications, this tool can enable an optimal choice of excitation/detection schemes and tracers through accurate calculations of fluorescence signal levels.

### Toluene

While the effects of pressure and gas composition can be relatively small with the ketones, the FQY from aromatics, including toluene, often is dominated by the proclivity of oxygen to quench its excited state:

$$\phi = \frac{A}{A+Q} \approx \frac{A}{k_q[O_2]} \quad (2.1.2)$$

if  $k_q[O_2]$  is the dominant quenching term and is much bigger than the spontaneous emission rate,  $A$ . While this oxygen sensitivity historically has been considered a reason to avoid the use of aromatics as fluorescent tracers, recent research has shown that the fluorescence signal from toluene can be directly proportional to the local equivalence ratio.

$$S_f \propto n_{tol} \sigma \phi \propto \frac{n_{tol}}{[O_2]} \propto \Phi \quad (2.1.3)$$

For the FQY to be linear with local equivalence ratio in combustion-related environments, one again must neglect possible temperature and other dependencies of the absorption cross section and the fluorescence quantum yield (including the temperature or energy dependence of the oxygen quenching coefficients  $k_q$  and other possible quenching mechanisms). By historical analogy with the ketones, temperature dependencies, though heretofore neglected, may not be negligible. We thus have undertaken fundamental studies of toluene absorption and fluorescence between room temperature and about 1000K as part of an ongoing program to quantify the properties of these tracers under combustion-relevant conditions. Initial findings are given in the following and in more detail in [2.1.6].

### Absorption

Figure 2.1.6 shows the near UV absorption spectrum of toluene at room temperature and after shock heating up to 1100K. Absorption is accessible using two popular laser wavelengths: 248 and 266nm. Though the spectrum is highly structured above 255 nm at room temperature, it broadens and smooths by 588K (the

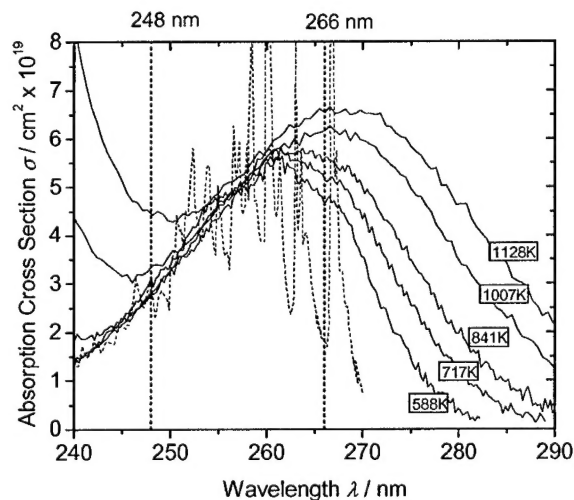


**Fig. 2.1.6** Near UV absorption spectrum of room temperature and shock-heated toluene. Dashed lines show room temperature spectrum from Burton [2.1.7].



lowest temperature accurately achievable in our shock tube). The strong structure at room temperature around 266nm indicates that laser absorption will change rapidly with temperature, while 248 nm excitation remains essentially constant until the red shift from the stronger S<sub>2</sub> system starts to play a role around 1000 K. Like the ketones, the red shift of the absorption at high temperatures may cause systematic errors in the detection of fluorescence without careful consideration.

### Fluorescence

The fluorescence of toluene has been resolved spectrally at various temperatures and is shown for 248nm excitation in Fig. 2.1.7. Unlike the ketones, the shape of the toluene

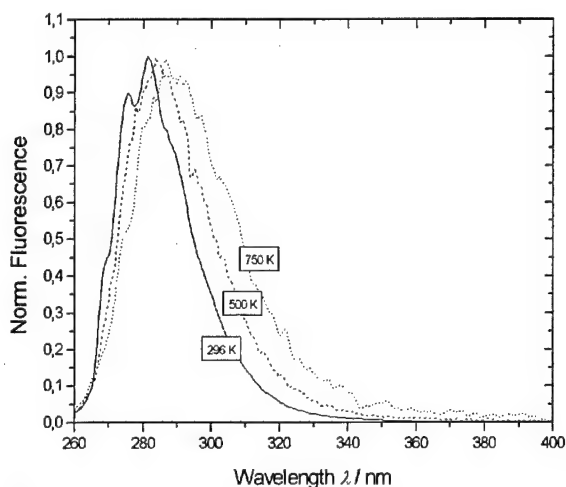


**Fig. 2.1.7** Shape of toluene fluorescence spectrum at a few temperatures when excited with 248 nm at 1 bar total pressure.

spectrum shifts to the red as temperature increases, and presents a potential complication because the temperature dependence will vary somewhat with the detection bandpass. This complexity is overcome fairly easily, however, since the shift is not too large and the detection band is usually easy to estimate for a given setup. As will be discussed further below, this shift may offer a simpler way to perform multi-parameter imaging than is accomplished with the two-laser, two-camera technique for the ketones.

The relative temperature dependencies of toluene's fluorescence quantum yield for 248 and 266 nm excitation are shown in Fig. 2.1.8 and 2.1.9, respectively. While yields from the ketones change by about 1 order of magnitude for 248 nm excitation, toluene is seen here to be even more sensitive to temperature, changing by over 3 orders of magnitude over the 600 K range studied. For 266nm excitation the decrease is slightly less dramatic but still much stronger than the ketones. This strong decrease in the fluorescence quantum yield dominates the overall fluorescence signal's dependence on temperature. There are a couple of key implications from these data. First, dramatic errors can be made when interpreting concentrations from single-line fluorescence images with even slight temperature gradients in the visualized field. On the other hand, in applications with uniform concentration, temperature imaging using toluene promises even more sensitivity than the ketones.

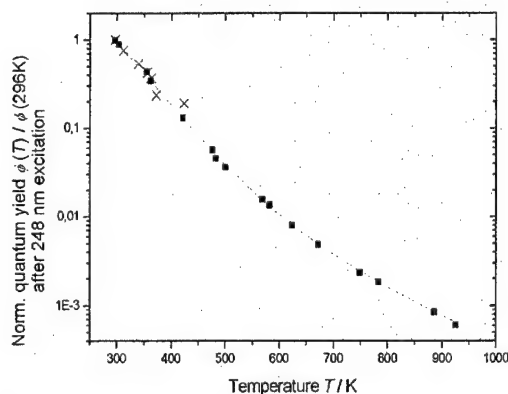


**Fig. 2.1.8** [■] Relative fluorescence quantum yield of toluene after 248 nm excitation. p=1 bar, nitrogen. [×] shows previous measurements from Burton [2.1.7].

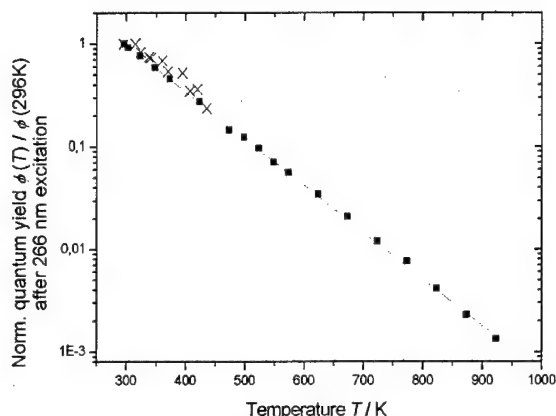


**Fig. 2.1.9** [■] Relative fluorescence quantum yield of toluene after 266 nm excitation. p=1 bar, nitrogen. [×] shows previous measurements from Burton [2.1.7].

fluorescence with 266 nm excitation detected around the peak of the emission spectrum ( $280 \pm 5$  nm, called “BP280”) and the signal in the long-wavelength tail ( $> 335$  nm, called “WG335” according to the Schott long-pass filter suggested for this purpose). The sensitivity of this signal ratio is of the same order as that of the two-line techniques for the ketones.

One might suspect that signal intensities may suffer from collecting only part of the spectrum; however, fluorescence signals in toluene are expected to be almost 500 times larger than for the ketones at ambient conditions, given the 10x larger absorption cross sections and the 50x larger fluorescence quantum yields (though this potential increase in signal has yet to be confirmed in our lab). The large drop in fluorescence signals, as indicated by Fig. 2.2.9, then should result in toluene signal levels at high temperatures on the same order as the ketones but with a simpler experimental arrangement.

In inhomogeneous, non-isothermal applications, the two-line techniques that have measured temperature and mole fraction successfully using ketones require the use of two lasers and two cameras. With toluene, the red shift in the fluorescence spectrum with temperature may eliminate the use of one laser, representing a significant cost savings. If two cameras collect data from different regions of the fluorescence spectrum, the ratio of the signals has a monotonic temperature dependence. Fig 2.1.10 shows the signal ratio of

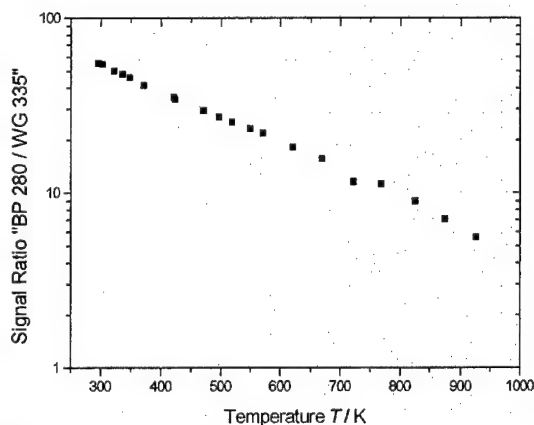


**Fig. 2.1.10** Fluorescence signal ratio from two regions of the emission spectrum after 266nm excitation.

### References for Section 2.1

- 2.1.1. Hansen, D. and Lee, E., "Radiative and Nonradiative-Transitions in First Excited Singlet-State of Symmetrical Methyl-Substituted Acetones," *J. Chem. Phys.* **62**, 183-189 (1975).
- 2.1.2. Koch, J.D. and Hanson, R.K., "Temperature and Excitation Wavelength Dependencies of 3-Pentanone Absorption and Fluorescence for PLIF Applications," *Appl. Phys. B.* **76**, 319-324 (2003).



- 2.1.3. Koch, J.D. and Hanson, R.K., "A Photophysics Model for 3-Pentanone PLIF: Temperature, Pressure, and Excitation Wavelength Dependences," *AIAA Paper 2003-0403* (2003).
- 2.1.4. Koch, J.D., Koban, W., Schulz, C. and Hanson, R.K., "Rayleigh-Calibrated Fluorescence Quantum Yield Measurements of Acetone and 3-Pentanone," *Appl. Opt.* (2004) in press.
- 2.1.5. Halpern, A. and Ware, W., "Excited Singlet State Radiative and Nonradiative Transition Probabilities for Acetone, Acetone-D<sub>6</sub>, and Hexafluoroacetone in Gas Phase, in Solution, and in Neat Liquid," *J. Chem. Phys.* **54**, 1271-1276 (1971).
- 2.1.6. Koban, W., Koch, J.D, Hanson, R.K. and Schulz, C., "Absorption and Fluorescence of Toluene at Elevated Temperatures," *Phys. Chem. Chem. Phys.* (2004) in press.
- 2.1.7. Burton, C. S. and Noyes, W. A., "Electronic Energy Relaxation in Toluene Vapour," *J. Chem. Phys.* **49**, 1705. (1968).

## ***2.2 Quantitative LIF and PLIF measurements in high pressure flames***

### **Background**

Laser-based detection of combustion species has proven to be an effective tool for combustion research [2.2.1, 2.2.2]. Such non-intrusive techniques enable optical diagnostics of practical combustors such as automobile engines and gas turbines, where imaging measurements can provide valuable information required for efficiency optimization and pollution control. Many of these combustors inherently operate with high pressures, where laser-induced fluorescence (LIF) is complicated by laser attenuation, interference, collisional quenching and pressure broadening. Previous spectroscopic studies of high-pressure combustion have not addressed these issues systematically, nor has any notable study been published in high-pressure flames exceeding 15 bar. The aim of this project is to investigate and develop LIF imaging strategies specifically optimized for application in high-pressure flames in the range of 5–60 bar. Much of the study has been focused on LIF strategies for the detection of nitric oxide (NO) (see below) and carbon dioxide (CO<sub>2</sub>) (see section 2.3), and temperature field imaging in high pressure flames using NO tracers (see below). In the past three years, we have made significant progress in both fundamental spectroscopic investigation and in practical imaging applications. Much insight has been gained, and new strategies have been proposed in an extensive effort that has resulted in over 15 publications.

### **Experimental Facility (High-Pressure Burner)**

To facilitate our research, a high-pressure burner was constructed in the High Temperature Gasdynamics Laboratory (HTGL) at Stanford University. Originally designed at the DLR in Stuttgart, Germany, this burner stabilizes a laminar, premixed methane/air flame on a porous sintered stainless steel matrix 8 mm in diameter, has an operating pressure range of 1–60 bar, and is capable of supporting flames up to 120 bar (Fig. 2.2.1).

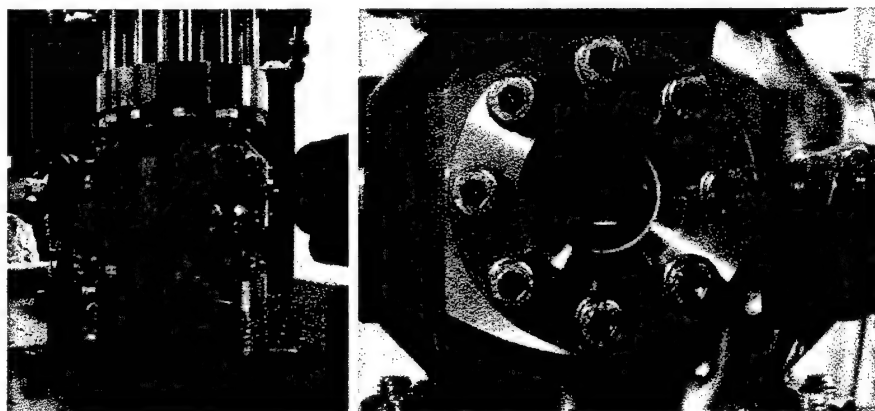


**Fig. 2.2.1** High Pressure Burner in HTGL, Stanford University.

The burner is mounted in a stainless steel housing with an inner diameter of 60 mm and pressure stabilization of  $\pm 0.1$  bar. The flame is stabilized, and pressure is regulated primarily by a jet of secondary air around the circumference of the burner matrix. Optical access to the flame is possible via four quartz windows. For NO-LIF, laser light (2mJ @ 220–260 nm, 0.25 cm<sup>-1</sup> FWHM) from a Nd:YAG-pumped (Quanta

Ray GCR250) frequency-doubled (BBO) dye laser (LAS, LDL205) was used for both single point measurements and laser sheet imaging. The pulse energy was measured with a photodiode (LaVision). Fluorescence signals were collected at right angles to the laser beam and focused with a  $f=105$  mm,  $f/4.5$  achromatic UV-lens (Nikon) onto an intensified CCD camera (LaVision Dynamight). An imaging spectrometer (Chromex 250IS) equipped with 300, 600 and 1200 grooves/mm gratings was integrated into the configuration for wavelength-resolved studies. A typical experimental setup for wavelength-resolved, line image and single-point work is shown in Fig. 2.2.2.

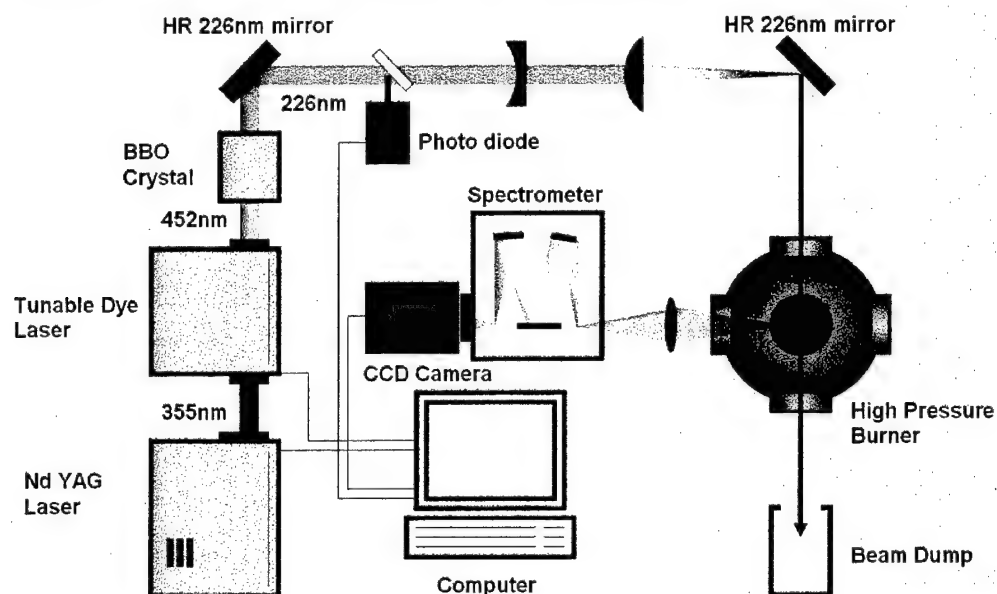


Fig. 2.2.2 Typical experimental setup for wavelength-resolved measurement (excitation at 226nm).

Typically, the signal light was separated from elastically scattered light using a combination of band-pass or long-pass dielectric filters. High-reflection mirrors or transmitting band-pass filters were used for isolation of specific detection wavelength regions. A typical focus size of the laser beam for single-point and/or line image measurements was 1.5mm diameter, while the beam was expanded to a sheet for imaging measurements with a typical cross section of  $3\text{--}10 \times 0.5 \text{ mm}^2$ . All measurements were conducted with excitation in the 220–260 nm wavelength region.

### 2.2.1 Strategies for Quantitative NO-LIF

#### NO-LIF Strategies with $A-X(0,0),(0,1),(0,2)$ Excitation/Detection

LIF has proven to be a reliable technique for nitric oxide (NO) diagnostics in practical combustion systems. Spectroscopy of NO-LIF has been studied extensively, and this literature is well-documented. Several approaches for NO excitation are suggested in the literature, including excitation in the  $D-X(0,1)$  band and in several  $A-X$  vibrational bands. Fig. 2.2.3 shows a potential energy diagram of the relevant electronic states of NO with transitions typically used for LIF diagnostics.

Application of NO LIF at high pressures is faced with a number of problems [2.2.3]. It was recognized in earlier work that interference from LIF of other species, mainly  $\text{O}_2$ , is a serious problem [2.2.4]. Hot  $\text{O}_2$  is the main contributor to LIF interference

in lean and non-premixed flames. The  $B^3\Sigma^- - X^3\Sigma^+$  Schumann-Runge bands of  $O_2$  overlap with the  $A^2\Sigma^+ - X^2\Pi$  NO gamma bands over a wide range of excitation wavelengths, resulting in overlapping absorption features and fluorescence signals. Fig. 2.2.4 shows excitation spectra for NO and  $O_2$  in a wavelength region of 225–248 nm, where the pervasive nature of the  $O_2$  spectra can be observed clearly. Other problems include pressure broadening and collisional quenching of the NO-LIF signal, which can be significant at pressures exceeding 40 bar. LIF from PAHs also can become an issue in rich flames, for  $\phi > 1.6$  in the premixed flames studied here. In the course of this work, we also discovered that absorption by hot  $CO_2$  can be a serious problem for NO-LIF, and significant effort was expended in quantifying these results. This  $CO_2$  absorption severely limits the transmission of light in high-pressure flames in the short UV wavelength region ( $< 200$  nm) and eliminates the use of NO  $D-X(0,1)$  LIF at 193 nm as a viable detection strategy. Our absorption studies of  $CO_2$  are discussed in detail in section 2.5 of this report.

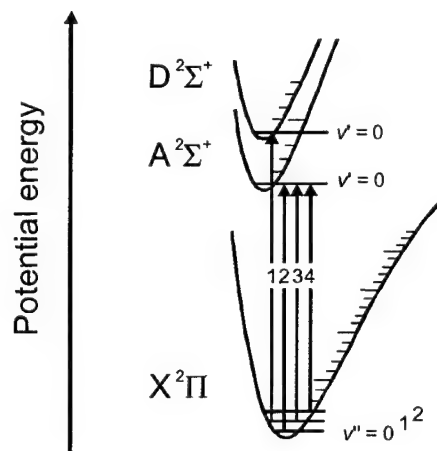


Fig. 2.2.3 Potential energy diagram of the NO  $X$ ,  $A$  and  $D$  states.  $D-X(0,0)$  near 193nm,  $A-X(0,0)$  near 225nm,  $A-X(0,1)$  near 236nm and  $A-X(0,2)$  near 248nm are shown with arrows.

Although a wide variety of different excitation and detection strategies have been proposed in the literature, no clear guidelines have been given for the optimum strategy applicable in a particular diagnostic situation. In this project, detailed spectroscopic investigation within the excitation region of 220–250 nm was conducted using wavelength-resolved LIF measurements in premixed methane/air flames at pressures between 1 and 60 bar and a range of fuel/air ratios. Excitation lines within the  $A-X(0,0)$ ,  $(0,1)$  and  $(0,2)$  bands of NO were scrutinized individually for LIF signal intensity, interference from hot  $O_2$ , and temperature dependence. The culmination of this extensive search has yielded five diagnostic strategies that are optimized for application in high-pressure flames. No one strategy can be recommended for all combustion situations, and the optimum choice is a trade-off among selectivity, signal intensity, optical accessibility, and signal quality in terms of laser and signal absorption. An important part of our work was to establish clear selection criteria for selection among these five viable strategies for NO-LIF detection in high-pressure flames.

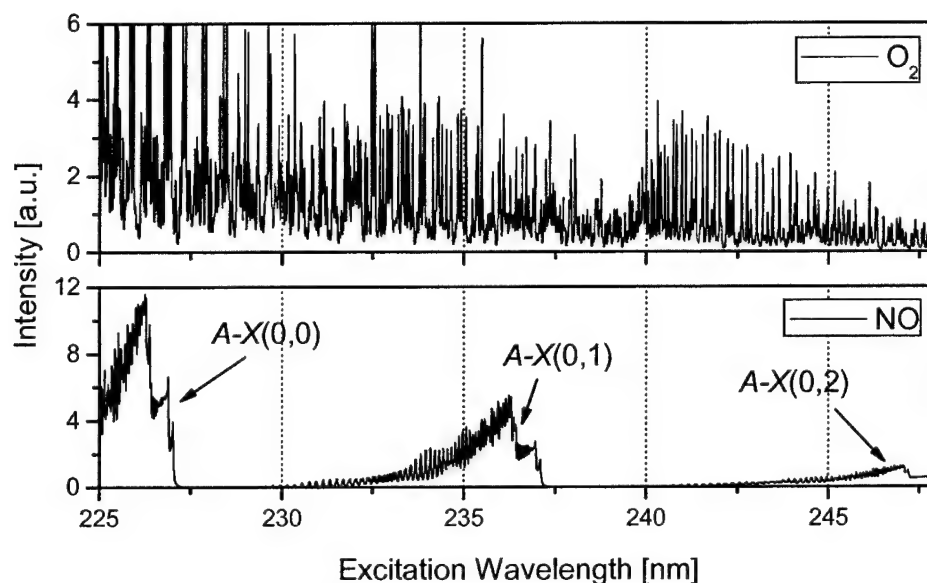


Fig. 2.2.4 Excitation spectra for NO and O<sub>2</sub> in wavelength region 225–248 nm.  $A-X(0,0)$ ,  $A-X(0,1)$  and  $A-X(0,2)$  transitions are shown with arrows.

The first strategy utilizes excitation of 226.03 nm in the  $A-X(0,0)$  transition with detection red-shifted of the laser. The  $A-X(0,0)$  transition of NO is the most frequently used method in the literature and extends over a region of 224–227 nm. It is the standard technique for NO detection and the only method that has sensitivity to cold NO. Detailed spectral investigations, along with numerical simulations, have shown that an excitation wavelength of 226.03 nm, proposed by M. Dirosa et al. at Stanford [2.2.5], offers the best performance [2.2.6] in the  $A-X(0,0)$  manifold. The  $A-X(0,0)$  approach clearly has advantages in terms of signal strength and selectivity. It is the strategy of choice for combustion diagnostics at all pressures as long as laser attenuation is acceptably low. It is, therefore, especially suitable for high-pressure combustion with small flame diameters. The temperature sensitivity allows measurement of NO concentrations without detailed knowledge of the temperature field. However, the red-shifted detection of potential PAH and CO<sub>2</sub> LIF interference may complicate or limit this approach.

The second and third strategies utilize excitation in the  $A-X(0,1)$  band. We have shown similarly that excitation at 235.87 nm provides the best performance for high-pressure combustion applications [2.2.7]. The two strategies utilize red- and blue-shifted detection of the laser wavelength, respectively. Red-shifted detection of the  $A-X(0,1)$  excitation is promising because it reduces laser beam attenuation while providing relatively strong signals ( $\approx$ one third of  $A-X(0,0)$ ); therefore, it can be applied to flames in which the path traveled by the laser beam is substantially longer. Signal purity from O<sub>2</sub> interference is still good at intermediate NO concentrations (around 300 ppm). The low temperature sensitivity allows measurement of NO mole fractions without knowledge of the temperature distribution. However, the red-shifted detection suffers from PAH and CO<sub>2</sub> LIF interference. Additionally, the blue-shifted detection after (0,1) excitation offers no particular advantage in signal strength, signal purity, or transmission properties.

The last two strategies utilize excitation in the  $A-X(0,2)$  band, with red- and blue-shifted detection of the laser wavelength. The blue-shifted detection has been employed widely in high-pressure, high-temperature detection. It is also popular due to the availability of the strong tunable KrF excimer laser that can provide the appropriate wavelength to excite the  $O_2$  bandhead at 247.94 nm. This approach, first proposed by Schulz et al. [2.2.8] to avoid the strong laser and signal attenuation observed in other transitions, is most effective in minimizing PAH interference, although the lack of signal strength makes it unfeasible for lasers that cannot provide enough power. Excitation within the (0,2) band with red-shifted detection suffers both in signal strength and in interference and is not recommended. All five strategies are summarized in table. 2.2.1, and the selection criteria are discussed in detail in reference [2.2.9].

Strategy	1	2	3	4	5
NO $A-X$ Band	(0,0) excitation (0,1)+(0,2) detection	(0,1) excitation (0,0) detection	(0,1) excitation (0,2)+(0,3) detection	(0,2) excitation (0,0)+(0,1) detection	(0,2) excitation (0,3)+(0,4) detection
1 bar excitation wavelength	226.031 nm	235.870 nm	235.870 nm	247.941 nm	247.941 nm
Detection bandpass	232-252 nm	217-232 nm	243-263 nm	220-240 nm	255-275 nm

**Table 2.2.1** Excitation and detection strategies for NO detection in high-pressure flames.

Comparisons of different excitation/detection strategies are governed by the combined effects of signal strength, signal interference, and pressure and temperature dependence [2.2.9]. We have been able to quantify and compare these effects by utilizing spectrally resolved measurements of NO-LIF, along with numerical simulation models. In particular, during the course of our studies, one of our collaborators (Wolfgang Bessler, University of Heidelberg) has developed a versatile numerical model for simulation of NO and  $O_2$  LIF spectra, LIFSim [2.2.10], which was tested extensively and implemented in our high-pressure flame diagnostics research. One of the major criteria in the comparison of the different  $A-X$  excitation strategies was signal strength. In high-pressure systems, where line-broadening and line-shifting severely influence the excitation efficiency, it is of significant importance to use NO transitions with a large ground state population at flame temperatures and high oscillator strength. Signal strengths calculated from simulated LIF signals, as well as from experimental data for the five different detection strategies proposed above, are shown in Fig. 2.2.5. The signal intensity decreases as we move from  $A-X(0,0)$  to (0,1) and to (0,2).

Another major criterion is the assessment of interference signals. High-pressure NO-LIF suffers from two types of interference: (i) *narrowband* in excitation and emission ( $O_2$  LIF) and (ii) *broadband* in excitation and emission ( $CO_2$  and PAH LIF). The choice of the vibrational band used for excitation influences the broadband interference problem, while the choice of a particular rotational absorption feature within the vibrational band is responsible largely for the contribution of narrowband  $O_2$ -LIF interference. We have assessed quantitatively the interference signals involved by separating the overlapping LIF signals of NO,  $O_2$  and  $CO_2$  in the emission spectra for the different strategies involved. A nonlinear least-square fitting procedure was used to separate the various overlapping LIF spectra and the contribution of elastically scattered light (Rayleigh). The

fits were performed with simulated spectra (generated by LIFSim), which allows for a more precise fit over a wider wavelength region. Figure 2.2.6 shows emission spectra and fitting results for the different excitation strategies proposed.

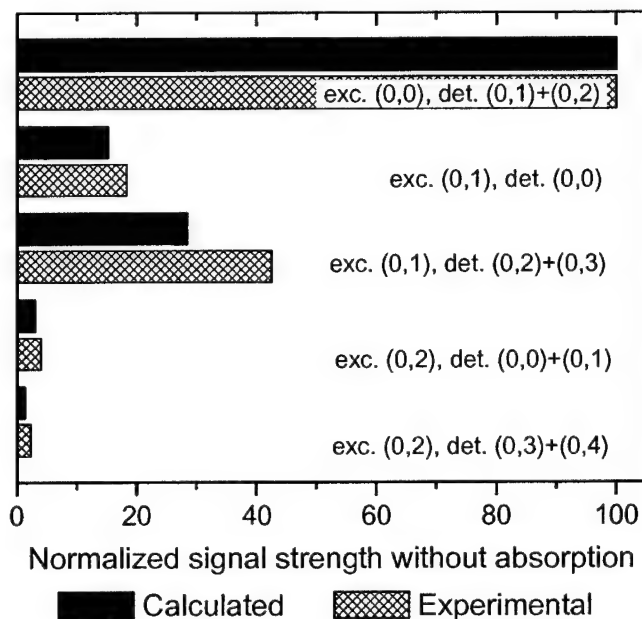


**Fig. 2.2.5** Calculated experimental signal strengths for a 10 bar flame with excitation/detection in the NO  $A-X$  system.

While the main criteria of comparison are signal strength and interference, other effects can cause considerable distortion of the LIF signal. Absorption from  $H_2O$ , and  $CO_2$  cannot be ignored at short wavelengths ( $<250nm$ ) and at high pressures, which results in the attenuation of the laser, as well as the fluorescence light. Another issue is the dependence of the LIF signal on temperature and pressure. Quantitative NO concentration measurements without knowledge of local temperature distribution require a choice of transition that has minimal temperature sensitivity. The main temperature influence of NO-LIF signal strength (on a per-molecule basis) arises from the ground state population of the laser-coupled levels. Since line-broadening and line-shifting is temperature-dependent, the overlap of the spectral features with the spectral shape of the laser also shows temperature dependence. Temperature furthermore influences the fluorescence quantum yield by changing collisional frequencies and quenching cross sections. The combined temperature effects of ground state population, spectral overlap, and quantum yield were calculated for the different strategies in the 10 bar flame with the  $0.4\text{ cm}^{-1}$  laser FWHM based on a steady-state three-level NO LIF model, and the sensitivity results are shown in Fig. 2.2.7.

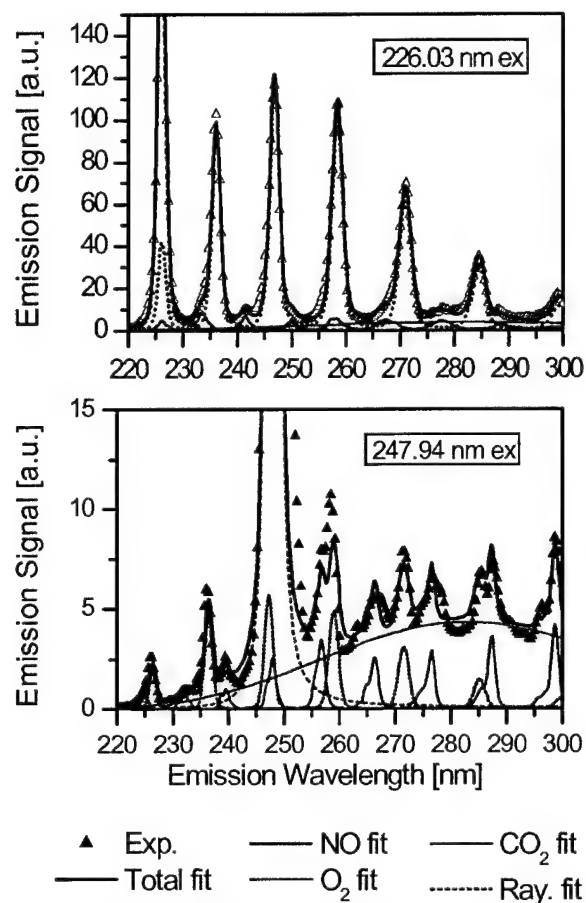


**Fig. 2.2.6** Examples of the nonlinear least-square fit of simulated NO, O<sub>2</sub>, CO<sub>2</sub> and Rayleigh emission spectra for the different excitation strategies at  $p=60$  bar and  $\phi=0.83$ . Intensity units are the same for each panel.

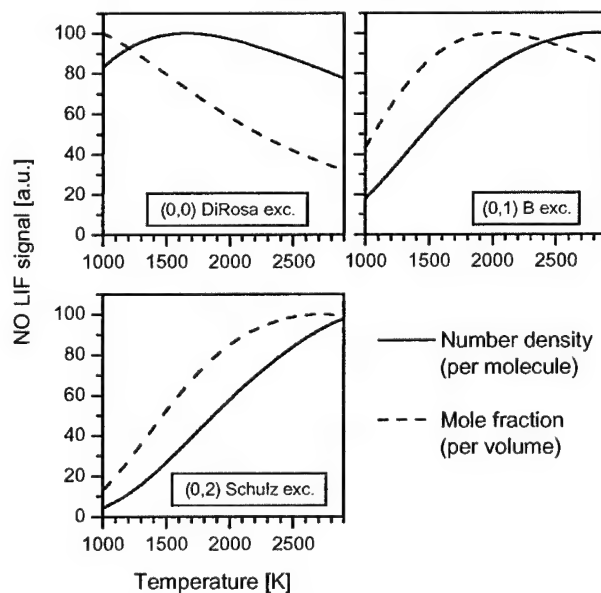


**Fig. 2.2.7** Simulated temperature dependence of the NO LIF signal at fixed number densities or mole fractions. ( $p=10$  bar,  $T=1900$  K).



The LIF signal depends on pressure through the change in excitation efficiency (line broadening and shifting) and fluorescence quantum yield (quenching). The overall effect leads to a stronger nonlinear decrease in LIF signal with pressure. The simulated pressure dependence of the NO-LIF signal for constant number density and mole fraction is shown in Fig 2.2.8. We have found that the LIF signal strength decreases by more than 2 orders of magnitude between 1 and 40 bar. In practice, this decrease is compensated partly by the effect of an increasing number density with pressure, leading to strong LIF signals even at elevated pressures. As pressure is increased, the excitation wavelength is shifted slightly to account for a pressure shift of the excitation spectrum.

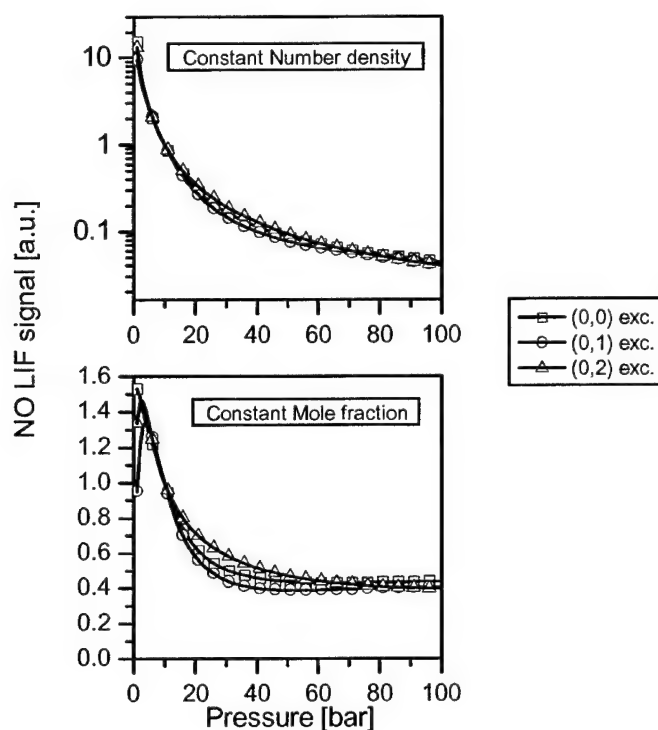


**Fig. 2.2.8** Simulated pressure dependence of the NO LIF signal at constant number densities or mole fractions, normalized to the 10 bar value.

A detailed spectral investigation of A-X(0,0),(0,1),(0,2) transitions and a discussion regarding comparison of specific excitation and detection strategies have been published in a series of papers in Applied Optics [2.2.6, 2.2.7, and 2.2.9].

### 2.2.2 Methods for LIF determination of Temperature in High-Pressure Flames

Accurate and precise measurement of temperature fields in high-pressure flames is a practical and important issue. Since LIF is a species-selective technique that allows probing of the population of specific rotational, vibrational, or electronic ground states, the temperature of the molecules can be inferred from the LIF signal. NO-LIF intensity  $I_{LIF}$  for weak, non-perturbing laser excitation is shown in Eqn. 2.2.1, where  $I_{laser}$  is the laser intensity,  $N(T)$  is the number density,  $\Gamma$  is the spectral overlap, and the two ratios are the Boltzmann fraction and the fluorescence yield.

$$I_{LIF} = c I_{laser} N(T) \frac{g \exp(-\epsilon/kT)}{Z(T)} B \Gamma(p, T) \frac{A}{A + Q(p, T)} \quad (2.2.1)$$

For our high-pressure combustion research, we have implemented both a two-line technique (Eqn. 2.2.2), where two ground states are probed and the temperature is inferred from the ratio of the two LIF signals, and a multi-line technique (Eqn. 2.2.3), where three or more ground states are probed and temperature is inferred from a Boltzmann plot or by fitting spectral simulations. The signals  $I_{LIF,i}$  and the laser intensity  $I_{laser,i}$  are measured, and  $g_i$ ,  $A_i$  and  $B_i$  are spectroscopic constants in calculating the Boltzmann plot.

$$R_{12} = \frac{I_{LIF,1}}{I_{LIF,2}} = \frac{c_1 I_{laser,1} g_1 \exp(-\epsilon_1/kT) B_1 \Gamma_1(p, T) A_1 / (A_1 + Q_1(p, T))}{c_2 I_{laser,2} g_2 \exp(-\epsilon_2/kT) B_2 \Gamma_2(p, T) A_2 / (A_2 + Q_2(p, T))} \quad (2.2.2)$$

$$\ln \left( \frac{I_{LIF,i}}{I_{laser,i}} \frac{g_i}{A_i B_i} \right) = -\frac{1}{T} \frac{\epsilon_i}{k} - \ln \left( \frac{Z(T)}{c N(T) \Gamma(p, T) Q(p, T)} \right) \quad (2.2.3)$$

In practical applications involving high-pressure flames, a number of effects such as simultaneous excitation of multiple lines, as well as the presence of background signals, complicate the simple analysis given above. Accurate LIF thermometry techniques need to include a full description of these effects. We have been able to develop a detailed spectroscopic model to deal with these issues which has led to the development of an NO-LIF multi-line thermometry technique. The thermometry approach uses a multi-line LIF imaging technique of transitions within the NO  $A-X(0,0)$  band, and the schematic of its implementation is shown in Fig. 2.2.9 [2.2.11].

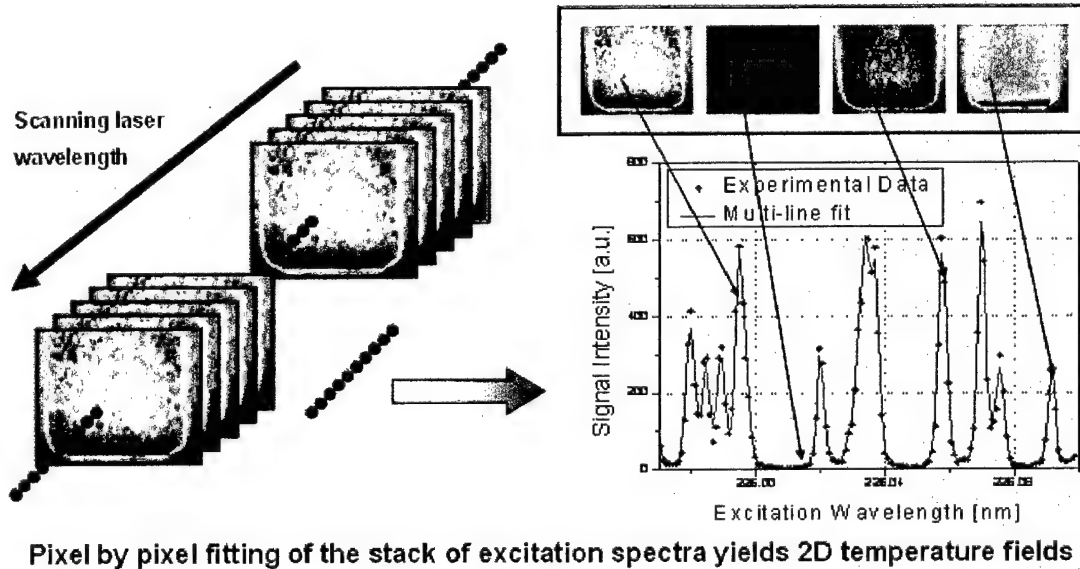


Fig. 2.2.9 Schematic of NO-LIF multi-line temperature fitting technique. Stacks of wavelength-scanned images are used to reconstruct 2D temperature fields.

The laser is tuned over a range of excitation wavelengths, and a 2D image is recorded at each spectral position. The resulting data set consists of a stack of 2D images

with different excitation wavelengths, yielding a three-dimensional data structure with two spatial axes and one excitation axis. For each pixel (corresponding to a local flame position), a LIF excitation spectrum can be extracted from this stack along the wavelength axis. The temperature at each pixel is evaluated by fitting a simulated spectrum to the experimental data using a Levenberg-Marquadt non-linear least-square fit. A 2D temperature field then can be reconstructed from the individual fitting results. We have been able to obtain temperature fields in flames ranging from 1 to 60 bar in pressure. While further refinement of this technique is underway for improved accuracy, preliminary results are shown in Fig. 2.2.10, revealing good precision for the uniform burnt gas temperature in this premixed flame and good accuracy for the comparison of the measured temperature to the equilibrium value.

### 2.2.3 Quantitative Imaging of Nitric Oxide in High-Pressure Flames

Based on the spectroscopic studies obtained from single-point measurements in high-pressure flames, we have published planar laser induced fluorescence (PLIF) images of NO concentrations from 1–60 bar with  $A-X(0,0)$  band excitation. To our knowledge, these are the first quantitative PLIF images of NO at elevated pressures exceeding 30 bar [2.2.12]. NO concentrations were calibrated with flames where NO was seeded in precise quantities (100 ppm intervals with  $\pm 10$  ppm error). Temperatures were inferred from the two-dimensional, multi-line thermometry technique described in the preceding section. Temperature fields were used to apply numerical corrections to the NO concentration from the temperature-dependent variation of the NO spectra, Boltzmann fraction, the total number density, the quenching rate, and  $T_{trans}$ , the total transmission factor. Corrections were made for the non-resonant background contributions, primarily from LIF of hot molecular oxygen and carbon dioxide. The impact of each correction was quantified to assess the error introduced in the NO measurements in practical high-pressure

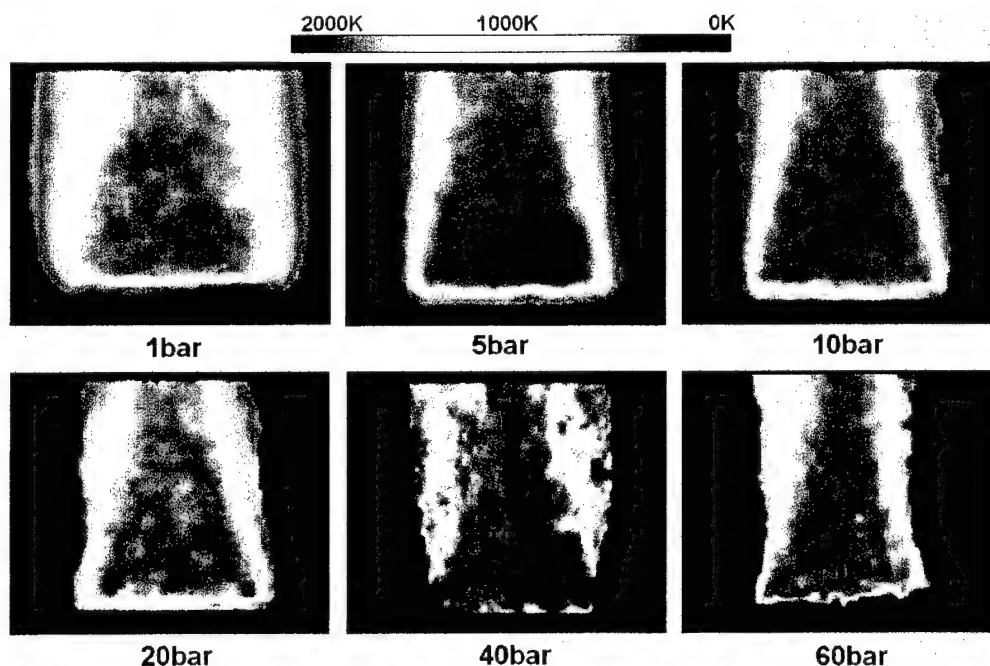


Fig. 2.2.10 Temperatures images of flames from 1 to 60 bar ( $\phi=0.95$ ,  $\text{CH}_4/\text{air}$  flame).

combustors, where simultaneously measuring temperature, background fluorescence, and laser and signal attenuation are not feasible. Despite choosing a NO excitation and detection scheme with minimum O<sub>2</sub>-LIF contribution, interference from O<sub>2</sub> was found to produce errors up to 25 % in a slightly lean ( $\phi=0.95$ ) 60 bar flame. We also have found that the attenuation caused by hot CO<sub>2</sub> and H<sub>2</sub>O traversing an 8mm path length in a 60 bar flame may reach 40 %. Quantification of NO was carried out for both number density and mole fraction, and the results from the imaging analysis are shown in Fig. 2.2.11. The NO imaging technique developed here is limited to stable flames where excitations scans can be performed over a specified wavelength region for temperature field extraction. Note the increased formation of NO in high-pressure flames. Work currently is underway to enable a single-shot method for quantitative NO imaging.

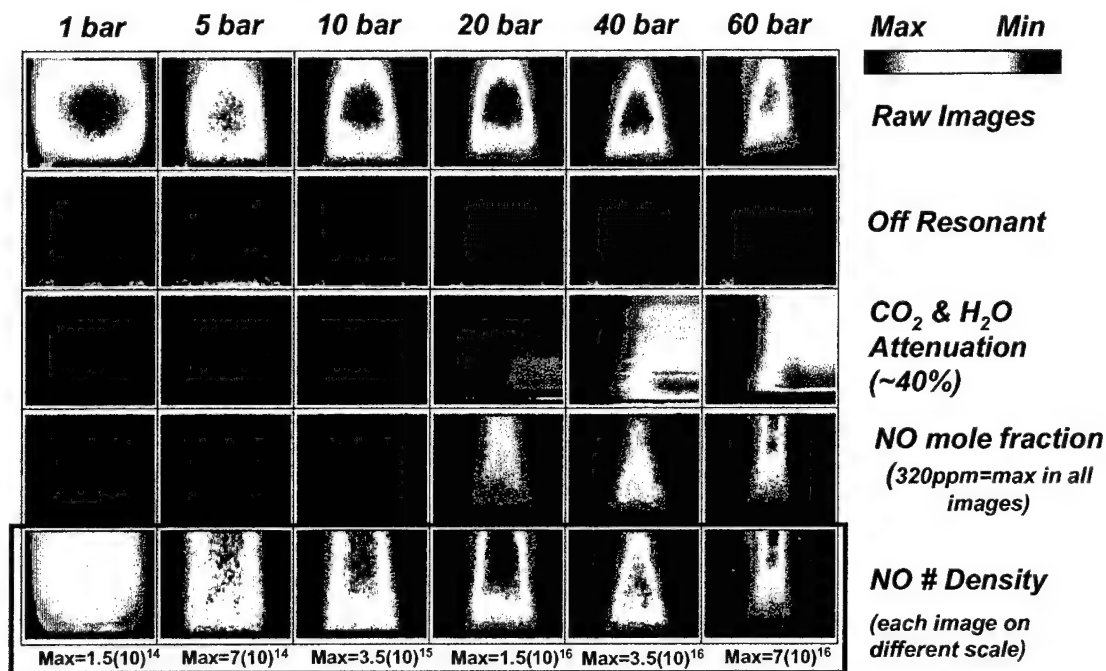


Fig. 2.2.11 Results of the imaging analysis from CH<sub>4</sub>/air flame ( $\phi=0.95$ , no NO seeding) at various pressures.

## References for section 2.2

- 2.2.1. Kohse-Höinghaus, K., Jeffries, J. B., (eds.) **Applied Combustion Diagnostics**, Taylor and Francis, New York, (2002).
- 2.2.2. Eckbreth, A. C., **Laser Diagnostics for Combustion, Temperature, and Species**, 2nd ed., Gordon and Breach, Amsterdam, The Netherlands, (1996).
- 2.2.3. Lee, T., Shin, D.-I., Jeffries, J. B., Hanson, R. K., Bessler, W. B., Schulz, C., "Laser-Induced Fluorescence Detection of NO in High-Pressure Flames with A-X(0,0), (0,1), and (0,2) Excitation," *AIAA-2002-0399* (2002).
- 2.2.4. Schulz, C., Jeffries, J. B., Davidson, D. F., Koch, J., Wolfrum, J., Hanson, R. K., "Impact of UV Absorption by CO<sub>2</sub> and H<sub>2</sub>O on NO LIF in High-Pressure Combustion Applications," *Proc. Combust. Inst.* **29**, 2725-2742 (2002).
- 2.2.5. Dirosa, M. D., Klavuhn, K. G., Hanson, R. K., "LIF Spectroscopy of NO and O<sub>2</sub> in High-Pressure Flames," *Combust. Sci. Technol.* **118**, 257-283(1996).
- 2.2.6. Bessler, W. G., Schulz, C., Lee, T., Shin, D.-I., Jeffries, J.B., Hanson, R.K.,

- “Strategies for Laser-Induced Fluorescence Detection of Nitric Oxide in High-Pressure Flames: I. A-X (0,0) Excitation,” *Appl. Opt.* **41**, 3547-3557 (2002).
- 2.2.7. Bessler, W. G., Schulz, C., Lee, T., Jeffries, J.B., Hanson, R.K., “Strategies for Laser-Induced Fluorescence Detection of Nitric Oxide in High-Pressure Flames: II. A-X (0,1) Excitation,” *Appl. Opt.* **42**, 2031-2042 (2003).
  - 2.2.8. Schulz, C., Yip, B., Sick, V., Wolfrum, J., “A laser-induced fluorescence scheme for imaging nitric oxide in engines,” *Chem. Phys. Lett.* **242**, 259-264 (1995).
  - 2.2.9. Bessler, W. G., Schulz, C., Lee, T., Jeffries, J.B., Hanson, R.K., “Strategies for Laser-Induced Fluorescence Detection of Nitric Oxide in High-Pressure Flames: III. Comparison of A-X Strategies,” *Appl. Opt.* **42**, 4922-4936(2003)
  - 2.2.10. Bessler, W. G., Schulz, C., Sick, V., Daily, J., “A Versatile Tool for Nitric Oxide LIF Spectra,” 3rd Joint Meeting of the US Section of the Combustion Institute, Chicago (2003) <http://www.pci.uni-heidelberg.de/pci/lifsim/>.
  - 2.2.11. Lee, T., Jeffries, J.B., Hanson, R.K., Bessler, W.G., Schulz, C., “Quantitative Multi-line Temperature Imaging in High Pressure Flames A-X(0,0), (0,1), and (0,2) Excitation,” *AIAA-2003-0583* (2003).
  - 2.2.12. Bessler, W. G., Schulz, C., Lee, T., Shin, D.-I., Hofmann, M., Jeffries, J. B., Wolfrum, J., Hanson, R. K., “Quantitative NO-LIF Imaging in High-Pressure Flames,” *Appl. Phys. B* **75**, 0946-2171 (2002).

### 2.3 First observation of UV LIF and PLIF Imaging of CO<sub>2</sub>

We have been able to identify and report first observations of CO<sub>2</sub>-LIF using UV excitation and emission in high-pressure flames, which has led to the development of a novel technique for imaging CO<sub>2</sub> under combustion conditions. While studying NO-LIF in high-pressure flames, we found that attenuation of the laser and fluorescence light across the path of the laser was significant. In practical applications using UV excitation in this spectral range, absorption from hot, vibrationally excited carbon dioxide (CO<sub>2</sub>) and water (H<sub>2</sub>O) are found to be the cause of such attenuation. These absorption results and their impact on NO-LIF studies are discussed in detail in section 2.5. Recent work on this grant has concluded that some of this absorption leads to LIF from CO<sub>2</sub> as broadband emission (200 – 450 nm) with a faint superimposed structure [2.3.1]. This broadband LIF emission was found to be present in spectrally resolved measurements of CH<sub>4</sub>/air and CH<sub>4</sub>/Ar/O<sub>2</sub> flames at elevated pressures. Figure 2.3.1 shows a spectrally resolved emission containing CO<sub>2</sub> LIF from a 60 bar CH<sub>4</sub>/air flame ( $\phi=0.83$ ). The LIF contribution from individual species has been quantified using numerical fitting of the emission spectra with LIFSim simulations.

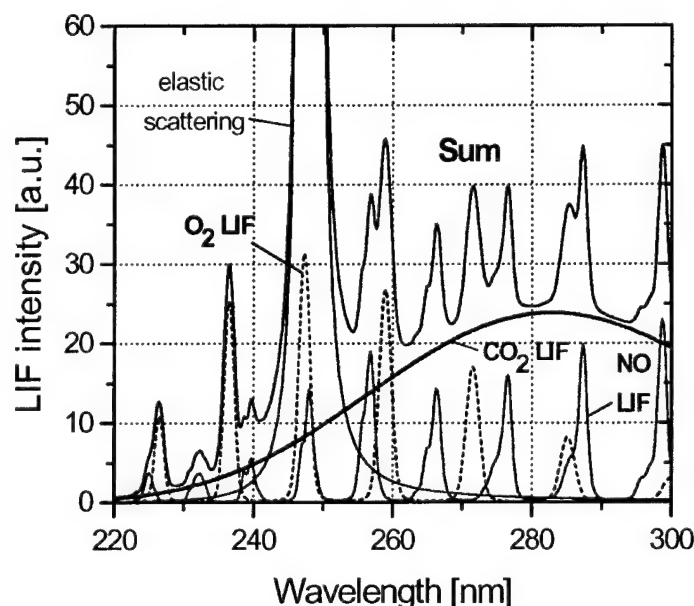
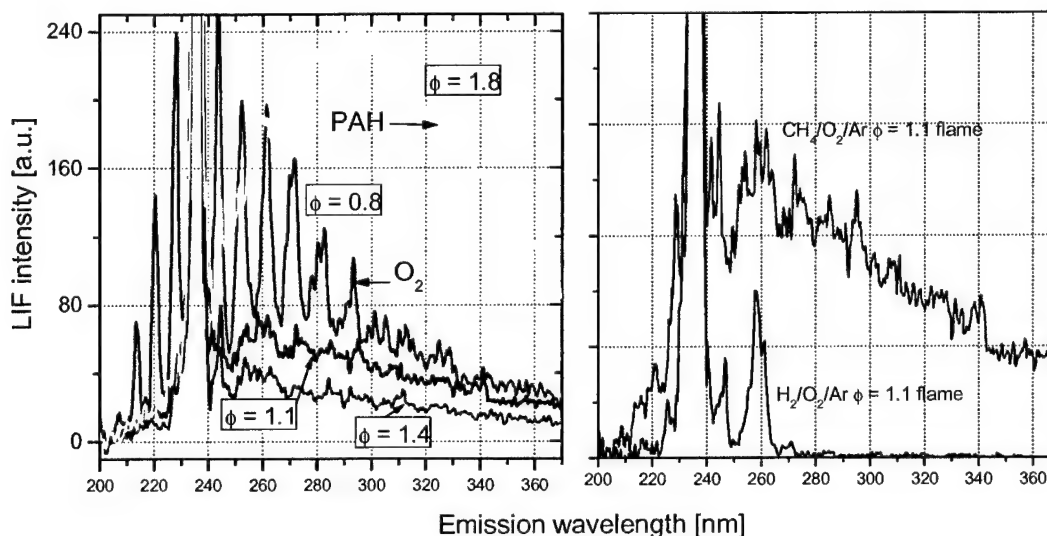


Fig. 2.3.1 Spectrally resolved emission from a 60 bar,  $\phi=0.83$  CH<sub>4</sub>/air flame. Broadband emission extending from 220–400 nm is LIF emission from CO<sub>2</sub>.

The variation of this broadband signal with excitation wavelength, equivalence ratio, and flame temperature correlated well with CO<sub>2</sub> absorption cross sections recently taken on shock-heated carbon dioxide [2.3.2]. Measurements were carried out in both CH<sub>4</sub>/air flames, as well as CH<sub>4</sub>/O<sub>2</sub>/argon flames, to confirm that nitrogen played no part in the formation of the broadband emission. Of the two dominantly absorbing species (CO<sub>2</sub> and H<sub>2</sub>O), LIF from H<sub>2</sub>O was ruled out as a possible source when no trace of the broadband LIF emission was detected in a 20 bar H<sub>2</sub>/O<sub>2</sub>/Ar flame. By a similar process of elimination, PAH-LIF also was excluded when spectrally resolved emission profiles with

variation in equivalence ratio showed that PAH-LIF appears under fuel-rich conditions only ( $\phi > 1.6$  for our flame) and has a profile characteristically different from the broadband  $\text{CO}_2$ -LIF, with a maximum at a longer wavelength. Results from measurements at different equivalence ratios and a comparison of the  $\text{CH}_4/\text{O}_2/\text{argon}$  and  $\text{H}_2/\text{O}_2/\text{Ar}$  flames are shown in Fig. 2.3.2. No broadband features are observed in an  $\text{H}_2/\text{O}_2/\text{Ar}$  flame, where the post products are mainly water.



**Fig. 2.3.2** Left diagram : Emission spectra with 235.88 nm excitation in the 20 bar  $\text{CH}_4/\text{O}_2/\text{Ar}$ -flame with  $\phi=0.8, 1.1, 1.4$  and  $1.8$ . Right diagram : Emission spectra with 235.88 nm excitation in  $\text{CH}_4/\text{O}_2/\text{Ar}$  (upper trace) and  $\text{H}_2/\text{O}_2/\text{Ar}$  (lower trace). The signals are accumulated over 1000 pulses.

Following this discovery, we have been able to report 2D PLIF images of hot  $\text{CO}_2$  using UV excitation in a high-pressure laminar flame [2.3.3,2.3.4]. To our knowledge, these are the first  $\text{CO}_2$  images published using UV-excitation and detection. Detection of  $\text{CO}_2$  UV-LIF in high-pressure flames is complicated by the following issues. Excitation of  $\text{CO}_2$  in the 200–300 nm spectral region directly overlaps with excitation of the  $\text{A}^2\Sigma^- - \text{X}^2\Pi$   $\gamma$  bands of NO and the  $\text{B}^3\Sigma^- - \text{X}^3\Sigma^+$  Schumann-Runge bands of  $\text{O}_2$ . Pressure broadening increases this overlap. Finding an excitation wavelength where both species are minimized is difficult due to the widely pervasive nature of  $\text{O}_2$  bands in this region [refer to Fig. 2.2.4]. For imaging measurements, we have chosen a strategy to use excitation wavelengths that completely avoid overlap with NO transitions in the region, while, at the same time, minimize the overlap with the multiple vibrational bands of  $\text{O}_2$ . Excitation wavelengths were chosen to be 239.34 nm and 242.14 nm. Both of these wavelengths are located between the A-X(0,1) and A-X(0,2) bands of NO. They also minimize the contributions of  $\text{O}_2$ , as predicted by numerical simulations and confirmed through experimental excitation scans with wavelength-resolved detection in a lean high-pressure flame ( $\phi = 0.8$ ,  $p = 10$  bar), where excess  $\text{O}_2$  yields a stronger LIF signal in the burnt gas. The resulting images were corrected for laser sheet inhomogeneities and the signal attenuation along the path of the laser beam caused by hot  $\text{CO}_2$  and  $\text{H}_2\text{O}$  absorption. Correction of attenuation utilizes recently quantified absorption cross section data [2.3.2] of hot  $\text{CO}_2$ , as well as flame temperatures obtained from multi-line fitting of NO LIF excitation scans using LIFSim. A first-order correction for  $\text{O}_2$  contamination



using additional spectrally-resolved images was carried out by taking spectrally-resolved images extracting the spatial distribution of  $O_2$  across the flame, and subtracting it from the  $CO_2$ -LIF image. For this correction, spectrometer measurements were taken at a location 3 mm above the burner matrix using a beam instead of an expanded laser sheet. The slit of the spectrometer provided the spatial resolution across the horizontal span of the flame.  $CO_2$  imaging results from a 20 bar  $CH_4$ /air flame are shown in Fig 2.3.3, including the temperature distribution and the laser beam attenuation.  $O_2$  contamination is stronger near the edges of the cone structure because co-flow air is entrained into the burnt gases by flame flicker.

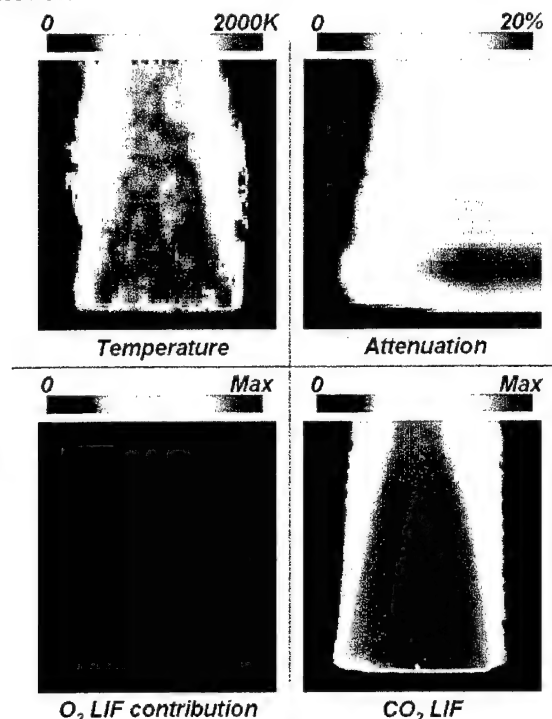


Fig. 2.3.3 Results from the  $CO_2$  imaging analysis from a 20 bar,  $\phi=1.1$   $CH_4$ /air flame.

For consideration of practical applicability as a diagnostics tool, the response of  $CO_2$  fluorescence signal to pressure and laser fluence is of interest. Pulses from a high-power Nd:YAG laser are typically a few ns (7 ns in our case), where concentrated laser fluence easily can exceed the saturation levels of the target molecule. The dependence of LIF intensity with laser strength was tested with a single-point measurement whereby the saturation probability was increased greatly by focusing the laser beam. Fig. 2.3.4 (left plot) shows that in the region of interest ( $0 \leq 700 \mu J/pulse$ ), the  $CO_2$  fluorescence signal is linear with laser fluence (laser sheet cross section of  $10 \times 0.5 mm^2$ ).

The  $CO_2$ -LIF signal also increases linearly with pressure in the 1–40 bar range, as shown in Fig. 2.3.4 (right plot) for various excitation wavelengths. This signal variation would indicate that the fluorescence lifetime is not limited by collisional quenching in the studied pressure range of 1–40 bar. Our current hypothesis is that dissociation and a fast intersystem-crossing are dominant lifetime-determining mechanisms. The electronic ground state of  $CO_2$  is a  $^1\Sigma_g^+$  state with ( $D_{\infty h}$ ) symmetry. The structure of the  $CO_2$  molecule indicates that interaction with UV light in the 200 – 300 nm range results in



population mostly of the bent  $^1B_2$  state 5.74 eV above the ground state energy and a small proportion in the  $^1A_2$  state. Previous studies of chemiluminescence 'CO flame bands', identified by Dixon [2.3.5] can populate the same excited state by the  $CO(^1\Sigma^+) + O(^3P)$  recombination reaction via intersystem crossing ( $^3B_2 \rightarrow ^1B_2$ ). However, the exact pathway involved in UV-excitation of  $CO_2$  has yet to be identified rigorously.

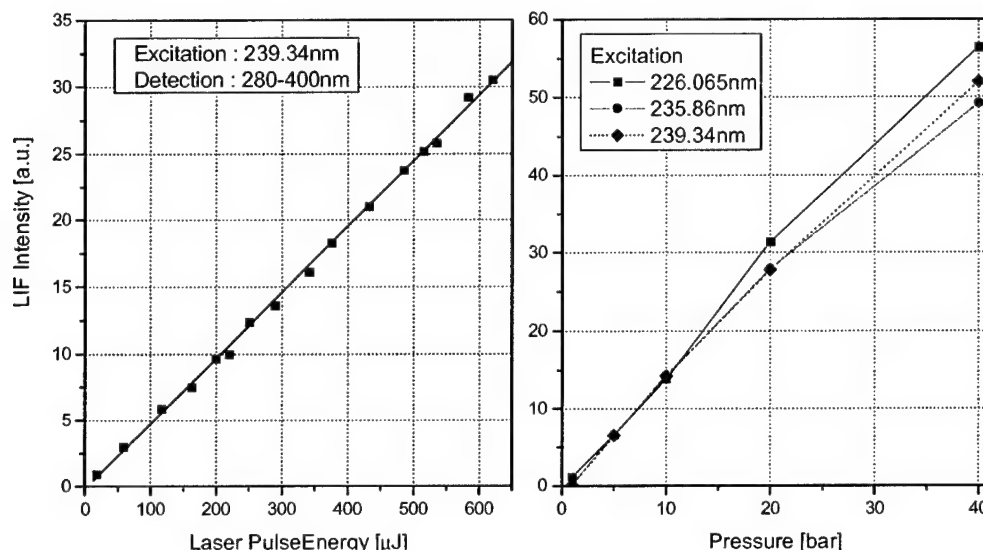


Fig. 2.3.4  $CO_2$  UV-LIF intensity versus laser pulse energy (left, 1 bar  $CH_4$ /air flame) and pressure (right,  $CH_4$ /air flame).

Further work is underway to image higher pressure regions (~60 bar) and to quantify the temperature and wavelength dependence of the  $CO_2$  fluorescence yield. The current methods are limited to stable flames. However, additional investigations into single-shot measurement techniques also are being addressed.

### References for section 2.3

- 2.3.1 Bessler, W. G., Schulz, C., Lee, T., Jeffries, J.B., Hanson, R.K., "Carbon Dioxide UV Laser-Induced Fluorescence in High-Pressure Flames," *Chem. Phys. Lett.* **375**, 344-349 (2003).
- 2.3.2 Schulz, C., Koch, J. D., Jeffries, J. B., Davidson, Hanson. R. K., "Ultraviolet Absorption Spectra of Shock-Heated Carbon Dioxide and Water Between 900 and 3050 K," *Chem. Phys. Lett.* **355**, 82-88 (2002).
- 2.3.3 Lee, T., Jeffries, J.B., Hanson, R. K., Bessler, W. G., Schulz, C., "Carbon Dioxide UV Laser-Induced Fluorescence Imaging in High-Pressure Flames," *AIAA-2004-0386* (2004).
- 2.3.4 Lee, T., Bessler, W. G., Schulz, C., Patel, M., Jeffries, J.B., Hanson, R. K., "UV Planar Laser Induced Fluorescence Imaging of Hot Carbon Dioxide in a 20 bar High-Pressure Flame," *Applied Physics B*, (2004), in preparation.
- 2.3.5 Dixon, R. N., "The Carbon Monoxide Flame Bands," *Discuss. Faraday Soc.* **35**, 105-112 (1963).

## ***2.4 Infrared Planar Laser-Induced Fluorescence (IR-PLIF)***

### **Background**

Many of the major product species resulting from hydrocarbon combustion ( $\text{CO}_2$ ,  $\text{CO}$ ,  $\text{H}_2\text{O}$ , unburned fuel species) do not have easily accessible single-photon electronic spectra. Therefore, these molecules lack relatively straightforward techniques for planar laser-induced fluorescence (PLIF) imaging. Because of the importance of these molecules to the combustion process, the spatially and temporally resolved data given by PLIF would contribute significantly to the design and analysis of combustion systems. Infrared (IR) excitation and subsequent fluorescence is possible for these molecules if they have an IR-active vibrational mode. With the advent of IR cameras with suitable integration properties and the ever growing number of high power lasers commercially available in the IR, IR PLIF of these molecules is now realizable. By exploiting new technological developments in the IR, we have made significant progress in research aimed at exploring the potential of IR PLIF.

In a prior funding period we demonstrated the first IR PLIF diagnostic for  $\text{CO}$  and  $\text{CO}_2$  [2.4.1-2.4.3]. These molecules were chosen due to their relevance to propulsion and their strong and relatively simple infrared spectra. The diagnostic strategies involved linear excitation and took advantage of the availability of short gate FPA IR cameras as well as IR laser sources (OPA/OPO systems). We were able to demonstrate that IR PLIF could be used to obtain high-quality single-shot images in a variety of environments, including flames.

During the current funding period we have continued the development of IR PLIF diagnostics for  $\text{CO}_2$  [2.4.3,2.4.4] and began work on the extension of IR PLIF to hydrocarbon molecules, in particular  $\text{C}_2\text{H}_4$ . The continued development of  $\text{CO}_2$  IR PLIF led to a new excitation strategy, saturated excitation, with a new laser source, a TEA  $\text{CO}_2$  laser. Saturated excitation potentially can simplify the interpretation of PLIF signals and generate the high signal levels necessary for imaging. The TEA  $\text{CO}_2$  provides a simple, robust, and economic means of excitation when compared to the optical parametric oscillator/amplifier (OPO/OPA) system used previously. The initial work that has been done on  $\text{C}_2\text{H}_4$  tests the ability to use IR PLIF on polyatomic molecules, where the increased density of energy states results in fast vibrational-to-vibrational (V-V) energy transfer. Our demonstrations of saturated IR PLIF of  $\text{CO}_2$  highlight our accomplishments during the current grant. We believe that with continued development IR PLIF diagnostics show great promise for a variety of applications, e.g., evaluating the fuel-oxidizer mixing process ( $\text{CH}_4$ ,  $\text{C}_2\text{H}_4$ , and higher hydrocarbons), investigation of exhaust gas mixing ( $\text{CO}_2$ ), and measurement of temperature distributions ( $\text{CO}_2$ ) and localized heat release ( $\text{CO}_2$ ,  $\text{H}_2\text{O}$ ), all of which expand the Air Force's ability to design and characterize hydrocarbon-fueled chemical propulsion systems.

### **Theory**

The work completed in the previous funding period focused on linear excitation of  $\text{CO}$  using an OPO/OPA system as a means of excitation. Our initial approach for  $\text{CO}_2$  imaging, therefore, utilized the same strategy. Because of the multiple vibrational modes present in  $\text{CO}_2$ , many possible excitation options are available, including combination bands at  $2.0\text{ }\mu\text{m}$  ( $20^0 1_{II} \leftarrow 00^0 0$ ) and  $2.7\text{ }\mu\text{m}$  ( $10^0 1_{II} \leftarrow 00^0 0$ ) and difference bands at  $9.6$

$\mu\text{m}$  ( $00^01 \leftarrow 10^00_{\text{II}}$ ) and  $10.6 \mu\text{m}$  ( $20^01_{\text{II}} \leftarrow 10^00_{\text{I}}$ ). Figure 2.4.1 is an energy level schematic of  $\text{CO}_2$  with the different possible excitation wavelengths and fluorescence wavelength shown. In all cases fluorescence is collected via the fundamental  $\nu_3$  band at  $4.3 \mu\text{m}$ . Use of the absorption band at  $2.7 \mu\text{m}$  for the excitation of  $\text{CO}_2$  poses experimental challenges due to the strong absorption by  $\text{H}_2\text{O}$  in this region, while excitation at the  $9.6 \mu\text{m}$  and  $10.6 \mu\text{m}$  bands become nonlinear at low fluences, making them more suitable for saturated excitation. Therefore, all of the work done using linear excitation of  $\text{CO}_2$  utilized  $2.0 \mu\text{m}$  excitation.

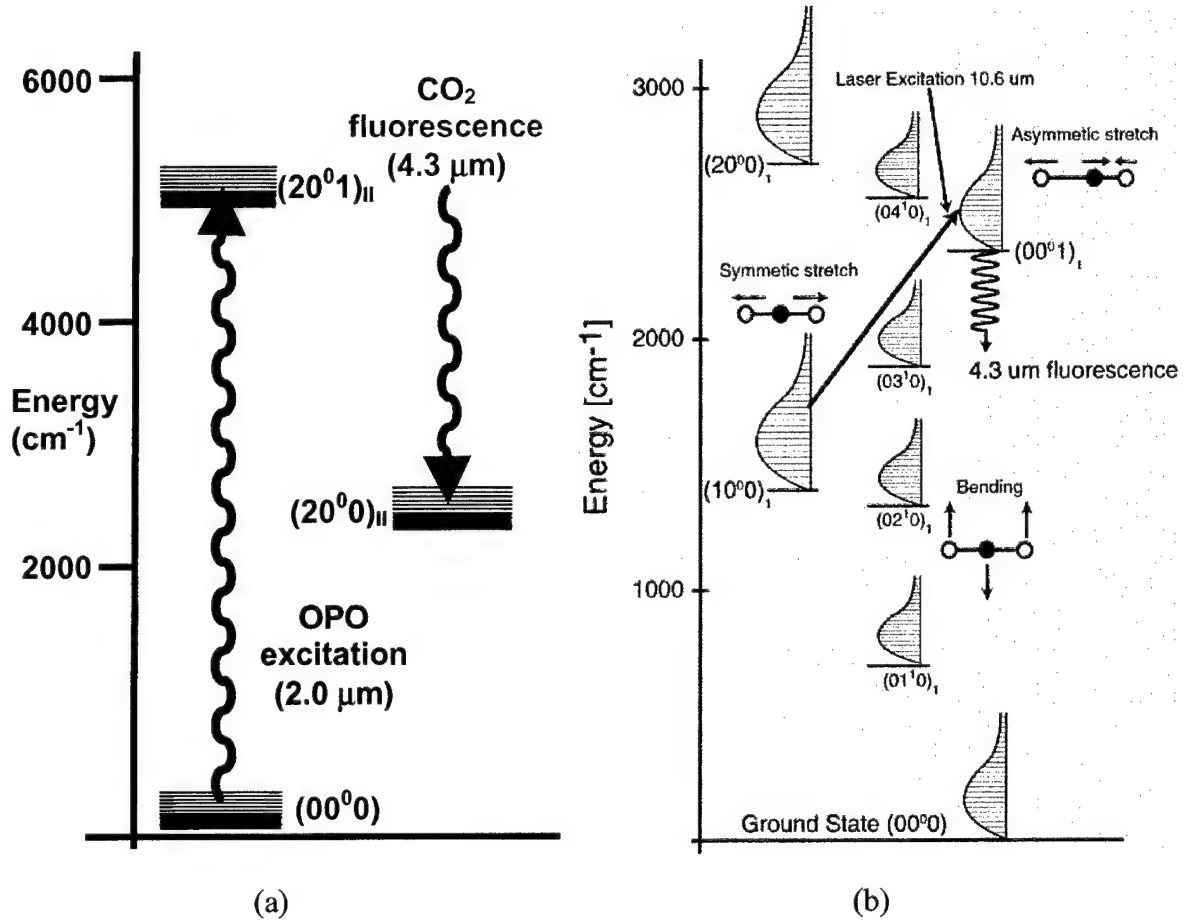


**Fig. 2.4.1** (a) Simplified energy level diagram of  $\text{CO}_2$  showing  $2.0 \mu\text{m}$  excitation; (b) simplified energy level diagram showing  $10.6 \mu\text{m}$  excitation of  $\text{CO}_2$ .

For linear excitation we quantify the fluorescence signal through the use of the linear fluorescence equation:

$$S_f = \frac{E}{h\nu} gSl \frac{P\chi_{\text{abs}}}{kT} \phi\eta_c \quad (2.4.1)$$

where  $S_f$  (photons per camera pixel) is the fluorescence signal;  $E$  (J) is the laser pulse energy incident on the imaged pixel volume;  $h\nu$  (J) is the energy per photon;  $g$  (cm) is the convolution of the laser and absorption lineshapes;  $S$  (cm) is the line strength per number

density, which takes into account the Boltzmann fraction of the absorbing species in the lower state of the laser transition;  $l$  (cm) is the length of the area imaged onto the pixel;  $P\chi_{abs}/kT$  ( $\text{cm}^{-3}$ ) is the number density of the species;  $\phi$  is the fluorescence quantum yield; and  $\eta_c$  is the collection efficiency of the optics and camera. The fluorescence signal for isobaric flows is a function of the imaged species mole fraction, bath gas concentrations (through energy transfer rates and their effect on fluorescence yield), and temperature (through energy transfer rates, number density, and state distributions). The temperature dependence can be limited through careful choice of the excitation line. However, for linear excitation of  $\text{CO}_2$  the influence of the bath gas concentrations on the uniformity of the fluorescence yield can be significant for typical integration times used in these experiments ( $\sim 1\text{-}2\ \mu\text{s}$ ). This complication motivates the use of saturated excitation.

The fluorescence yield encompasses all of the details of the vibrational transfer. For the collection of  $\nu_3$  fluorescence from  $\text{CO}_2$  the laser-induced excess of vibrational energy is depleted by non-resonant intermodal V-V transfer (upon collisions with any molecule M), by near-resonant transfer (upon collisions with molecules such as CO and  $\text{N}_2$ ), and by non-resonant intermolecular transfer (upon collision with molecules such as  $\text{H}_2\text{O}$ ). The short characteristic time ( $\sim 100\ \text{ns}$ ) associated with near resonant V-V transfer with  $\text{N}_2$  causes dilution of the fluorescence signal. In the limit of very high dilution by  $\text{N}_2$  this process dominates, and the fluorescence yield approaches  $A/k_{VV}$ , where  $A$  is the Einstein A coefficient and  $k_{VV}$  is the rate of near-resonant V-V transfer between  $\text{N}_2$  and  $\text{CO}_2(\nu_3)$ .

The strong influences of  $\text{N}_2$  and  $\text{H}_2\text{O}$  can cause significant variation in  $\phi$  if the concentrations of these species vary throughout the field of view. Figure 2.4.2 shows the impact of these effects on the fluorescence quantum yield. For the experimental conditions used in Fig. 2.4.2 it is apparent that generating a uniform fluorescence quantum yield for situations with significant variation in concentration would be difficult. These results show the care with which experimental design must be undertaken to minimize these effects. They also motivate the use of saturation-based excitation techniques that can be made insensitive to the details of the energy transfer, and therefore, have the potential to simplify the interpretation of the  $\text{CO}_2$  IR PLIF signal.

By saturating the laser transition the population in the upper and lower states is driven to be equal (neglecting differences in the degeneracy of the two states). Ideally the laser pulse saturates the transition completely throughout the entire integration time so that the populations remain constant during the camera integration. Saturated excitation leads to a different modeling approach than was used for linear excitation. In particular, instead of dealing with a linear fluorescence quantum yield, for saturated excitation it is more convenient to define a saturated fluorescence yield, defined as the number of emitted photons normalized by the number of absorbing molecules in the laser-excited volume:

$$\Psi_{sat} = \sum_j \int_0^\tau \frac{\Delta N_j(t)}{n_{abs} V} A_j dt \quad (2.4.2)$$

where  $\Delta N_j(t)$  is the instantaneous laser-induced change in population;  $n_{abs}$  ( $\text{cm}^{-3}$ ) is the absorbing species number density;  $V$  ( $\text{cm}^3$ ) is the volume of the laser sheet;  $\tau$  (s) is the

camera integration time; and  $A_j$  is the Einstein A coefficient (emission rate for the state). With this definition the fluorescence equation can be rearranged to give:

$$S_f = \frac{\Psi_{sat}}{T} \chi_{abs} \frac{PV}{k} \eta_c \quad (2.4.3)$$

where for isobaric flows the only unknown parameter is  $\Psi_{sat}/T$  (assuming  $V$  and  $\eta_c$  are easily calibrated). This fact greatly simplifies signal interpretation since it can be shown that this parameter is relatively insensitive to the bath gas composition and temperature for certain conditions.

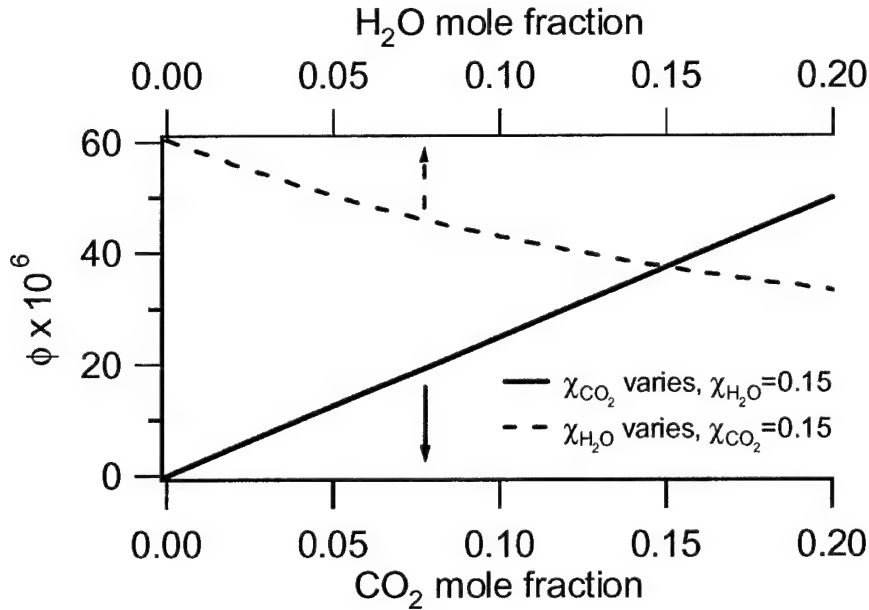


**Fig. 2.4.2** Variation of linear fluorescence quantum yield shown as a function of the bath gas concentrations. Nominal gas mixture is 15% H<sub>2</sub>O, 15% CO<sub>2</sub>, balance N<sub>2</sub>, at 1000K. The fluorescence yield ( $\phi$ ) approaches  $A/k_{VV}$ , which is quite low, as the CO<sub>2</sub> mole fraction approaches zero.

In order to investigate the dependence of  $\Psi_{sat}$  on temperature and bath gas concentrations it usually is necessary to model the full state-to-state energy transfer. However, for CO<sub>2</sub> an investigation of the characteristic rates of transfer show that a three-temperature model is adequate for most situations. A comparison of the characteristic rates of transfer is shown in Fig. 2.4.3, where the rates representative of rotational energy transfer (RET), laser pumping, intramodal transfer, and intermodal transfer are plotted versus temperature. Because the RET rate is fast, the rotational distribution in each vibrational level is Boltzmann, with a well-defined rotational temperature equal to the translational temperature ( $T_{tr}$ ). Rapid intramodal transfer implies that each vibrational mode has an individual Boltzmann distribution and, therefore, a well-defined temperature. Furthermore, the accidental degeneracy between the  $v_1$  and  $v_2$  modes results in fast transfer between these modes. Thus  $T_1$  is equal to  $T_2$ . Finally, the intermodal rate between  $v_3$  and the other two modes is slow, so the temperature  $T_3$  is independent of the other two modes. Accordingly, only three independent parameters ( $T_{tr}$ ,  $T_1$ ,  $T_3$ ) are

required to describe the laser-generated nonequilibrium vibrational distribution in the CO<sub>2</sub> molecules.

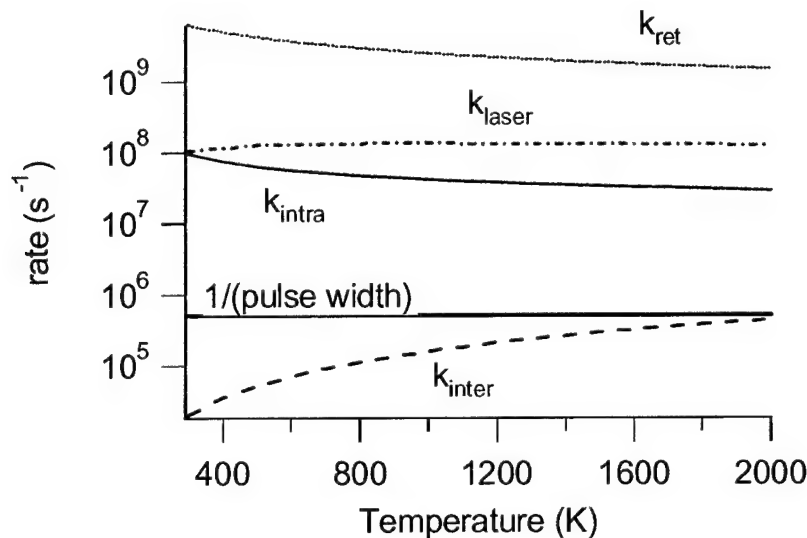


Fig. 2.4.3 Comparison of rates for various energy transfer processes in CO<sub>2</sub>

Vibrational temperatures are compact descriptors of the vibrational population distributions and consequently are the most useful parameters for describing PLIF signal levels. For each vibrational mode the temperature can be directly related to the emission rate from that mode in a straightforward manner. Assuming that the temperature of the emitting mode ( $T_3^*$ ) remains constant during the camera integration period, the saturation fluorescence yield is given by:

$$\Psi_{sat} = A\tau \left[ \frac{1}{\exp(\Theta_3/T_3^*) - 1} - \frac{1}{\exp(\Theta_3/T) - 1} \right] \quad (2.4.4)$$

where  $\Theta_3$  (K) is the characteristic temperature of the vibrational mode of interest ( $v_3$ );  $T_3^*$  (K) is the laser-perturbed temperature of the mode;  $A$  is the Einstein A coefficient for  $v_3$  ( $425 \text{ s}^{-1}$ );  $\tau$  (s) is the camera integration time; and  $T$  (K) is the initial temperature prior to laser excitation.

Equation 2.4.4 relates the saturated fluorescence yield to the vibrational temperature of the emitting mode; however, this temperature still needs to be determined. Because the rate of laser pumping is significantly higher than the intermolecular transfer rate,  $T_3^*$  can be found by ignoring these transfer rates and assuming that the transition is fully saturated. Under these assumptions the populations in the lower and upper laser levels are driven to be equal. If the harmonic oscillator assumption is used, along with conservation of energy,  $T_3^*$  can be determined as a function of the initial temperature. Figure 2.4.4 shows  $T_3^*$  and  $\Psi_{sat}$  plotted versus the initial temperature. It is apparent in Fig. 2.4.4 (a) that  $\Psi_{sat}$  has significant dependence on the initial temperature. However, we must remember that the quantity of interest for saturated fluorescence is not  $\Psi_{sat}$ , but

$\Psi_{\text{sat}}/T$ . The dependence of  $\Psi_{\text{sat}}/T$  on temperature is shown in Fig. 2.4.4 (b), along with a comparison of the three temperature model predictions with detailed model calculations.

The three-temperature model agrees very well with the detailed model over the entire range. As was stated earlier, the quantity  $\Psi_{\text{sat}}/T$  shows little dependence on temperature for certain conditions; in particular for temperatures above 1500K the quantity varies little over a wide temperature range. In Figs. 2.4.4 (c) and 2.4.4 (d) the insensitivity of saturated excitation to bath gas concentrations is demonstrated. These results indicate that saturated fluorescence is less sensitive to the bath gas concentration than linear excitation. The reduced sensitivity suggests that it should be easier to insure a uniform fluorescence yield throughout the imaged region, allowing for a more direct signal interpretation.

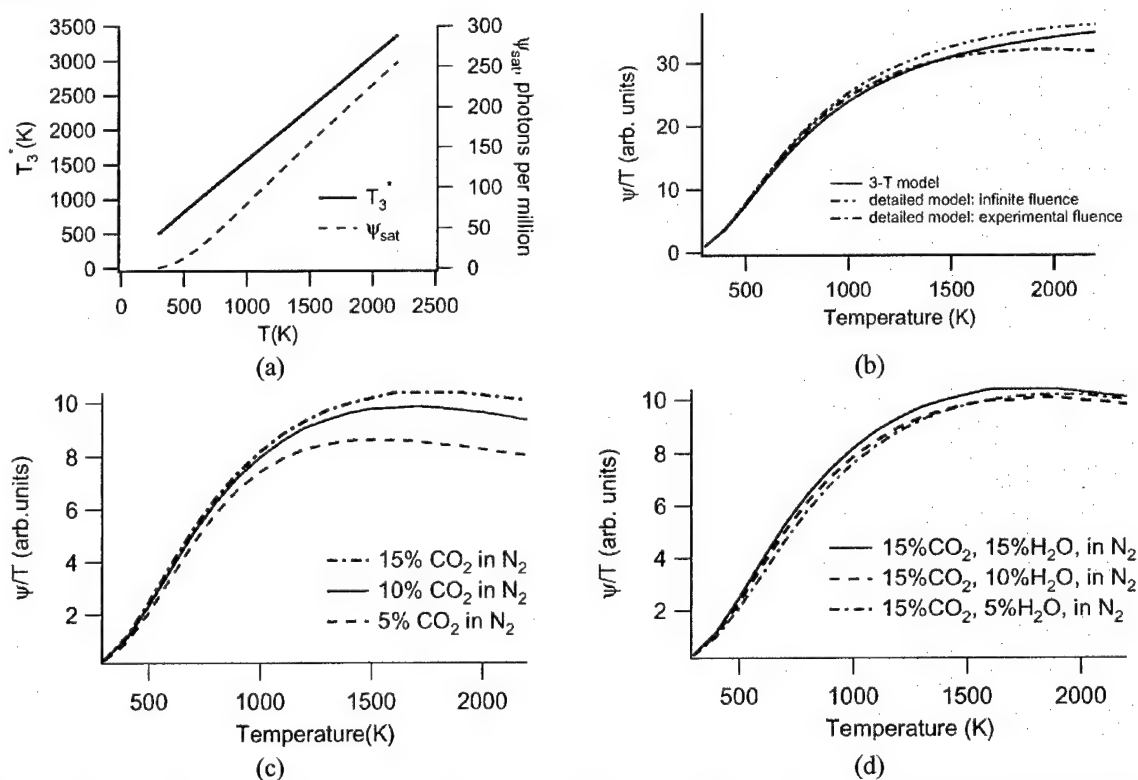


**Fig. 2.4.4** (a) Predictions of the three-temperature model for  $v_3$  mode temperature ( $T_3^*$ ) and fluorescence yield; (b) Comparison of LIF signal levels at constant  $\text{CO}_2$  mole fraction as predicted by the three-temperature model and a detailed rate equation model; (c) Influence of varying  $\text{N}_2$  mole fraction on  $\text{CO}_2$  LIF signal; (d) Influence of varying  $\text{H}_2\text{O}$  mole fraction on  $\text{CO}_2$  LIF signal.

Using insights gained from our work with  $\text{CO}_2$ , which has three vibrational modes, we have begun evaluating IR PLIF of  $\text{C}_2\text{H}_4$  which has twelve vibrational modes. The large increase in vibrational modes has significant implication on the vibrational energy transfer. For molecules with many vibrational modes the energy spacing between states becomes significantly reduced, and at high levels of vibrational energy a quasi-continuum of states exists due to the large number of possible combination and overtone bands. Collisionless intramolecular vibrational energy transfer becomes important once the molecule becomes larger than propane for hydrocarbon molecules [2.4.5]. The

properties of polyatomic molecules point towards fast equilibration within the vibrational manifold. However, even if the vibrational manifold reaches a partial equilibrium during the time period of the laser pulse, the vibrational and translational modes may remain in a nonequilibrium state. This nonequilibrium distribution allows for opportunities to image polyatomic molecules using IR PLIF.

The fast equilibration of the vibrational modes for large hydrocarbons suggests a simple method for modeling these molecules. If one assumes the vibrational equilibration rates are of the same order of magnitude as the laser excitation rate or faster, then a single vibrational temperature may exist for the species, and one only needs to keep track of the energy flow into and out of the vibrational manifold to determine that temperature as a function of time during the laser pulse. This simplified procedure is the approach that we have taken so far. Figure 2.4.5 shows some preliminary results comparing the model-predicted signal and the measured fluorescence of ethylene for single point excitation. The temporal behavior of the fluorescence matches the model well. However, further work needs to be done to improve the model for quantitative prediction of fluorescence yields. The significant difference in predicted signal level is likely due to uncertainties in the collection efficiency and the laser absorption lineshape overlap integral.

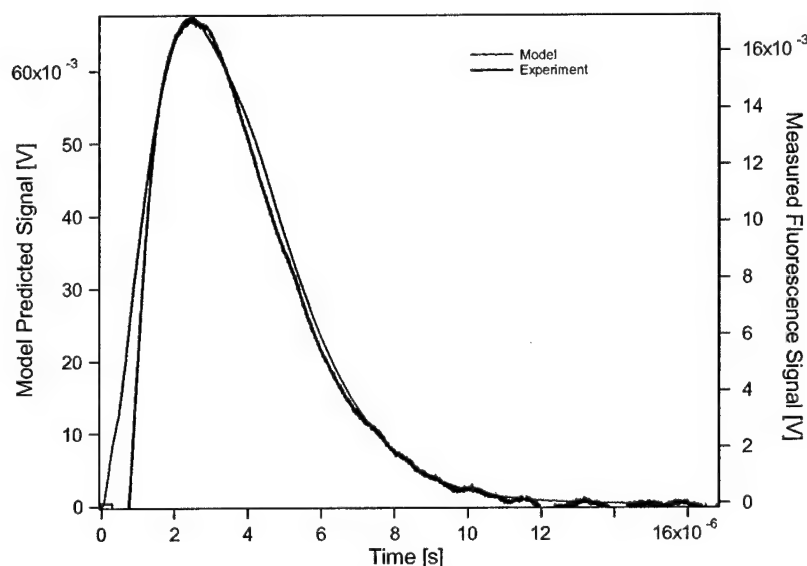


**Fig. 2.4.5** Single-point measurement of ethylene fluorescence as a function of time: fluorescence collected for the 4.5-5.0  $\mu\text{m}$  region, TEA  $\text{CO}_2$  laser pulse of 0.2 J/pulse, ethylene pressure of 10 torr diluted to 1 atm with  $\text{N}_2$ . Difference in magnitude due to uncertainty in collection efficiencies and laser pumping rate.

The fast equilibration of the vibrational modes causes significant signal dilution, and unique collection strategies may be necessary to image molecules like  $\text{C}_2\text{H}_4$  successfully. Some possible solutions to this problem include collecting fluorescence from multiple modes simultaneously and using collection at longer wavelengths to collect fluorescence from lower energy modes, where significantly more population exists.



### Imaging Setup

A typical setup for saturated excitation of  $\text{CO}_2$  is shown in Fig. 2.4.6. Excitation is provided by a TEA  $\text{CO}_2$  laser, which operates primarily on the  $\text{P}20$  transition of the  $00^0_1 \leftarrow 10^0_1$  band at  $944.194 \text{ cm}^{-1}$ . The laser provides pulses of approximately  $5 \mu\text{s}$  duration with  $5 \text{ J}$  of energy. The fluorescence was imaged by two  $256 \times 256$  pixel InSb cameras (Santa Barbara Focalplane SBF 134) through  $4.1\text{--}4.5 \mu\text{m}$  interference filters. Only one camera is necessary to image the fluorescence, but in unsteady flows with luminous backgrounds the second camera is used to record the flow luminosity just before the laser pulse and correct for it. Details of dual-image techniques have been described previously [2.4.3]. Because IR PLIF signals in the saturated limit are proportional to sheet thickness, images are normalized by averaged reference images of uniform-concentration isothermal flow fields. The incomplete saturation in the extreme spatial and temporal parts of the laser sheet causes small errors ( $\sim 5\%$ ).

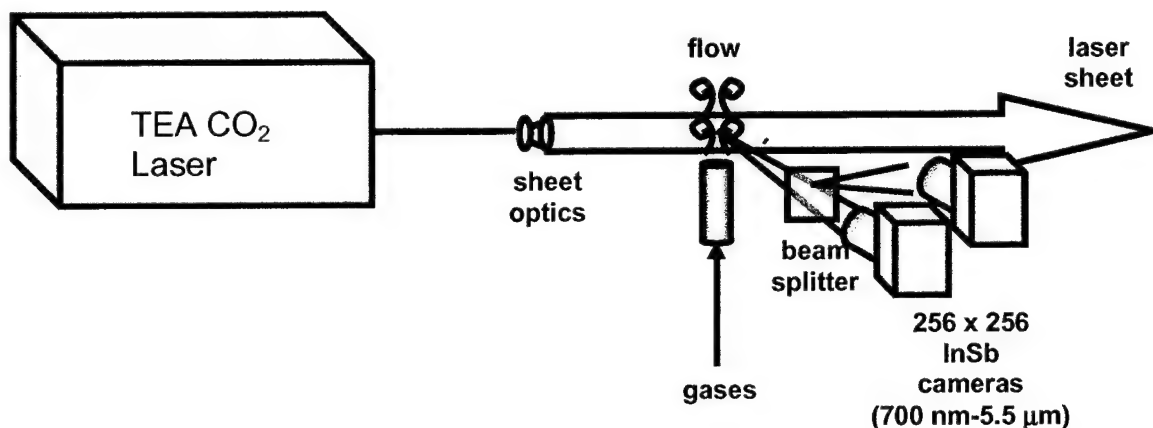


Fig. 2.4.6 Schematic of typical experimental setup for saturated excitation of  $\text{CO}_2$

### Imaging Experiments

Two examples of saturated excitation of  $\text{CO}_2$  are shown in Figs. 2.4.7 (a) and 2.4.7 (b). Figure 2.4.7 (a) depicts a transverse jet of  $\text{CO}_2$  heated to  $425 \text{ K}$  in an air crossflow imaged using the dual-camera technique. The second image in Fig. 2.4.7 (b) is of a flame fueled with  $50\% \text{CO}/50\% \text{Ar}$  mixture ( $\sim 2\% \text{H}_2$  added for stability). Because the flow was steady a single camera could be used to acquire both the data and background images.

The  $425\text{K}$  jet highlights the ability to image  $\text{CO}_2$  at low temperatures using saturated excitation. For this flow an exposure time of  $2 \mu\text{s}$  was used, and background luminosity was quite minor ( $\text{S/B} = 20$ ) for the flow, but a background correction still was performed. The background image was triggered  $4 \mu\text{s}$  before the start of the PLIF image, giving an effective temporal resolution of approximately  $6 \mu\text{s}$ . For this flow the signal is proportional to  $\text{CO}_2$  concentration, with some small errors caused by variation of the saturated fluorescence yield throughout the field of view. These variations are much smaller than the large gradients in the image, so their influence is relatively small for this

image. The peak signal-to-noise (SNR) for single-shot images was typically 50, giving a minimum detectable concentration at 425K and 1 atm of  $2.7 \times 10^{17}$  molecules/cm<sup>3</sup> (1000 ppm mole fraction).

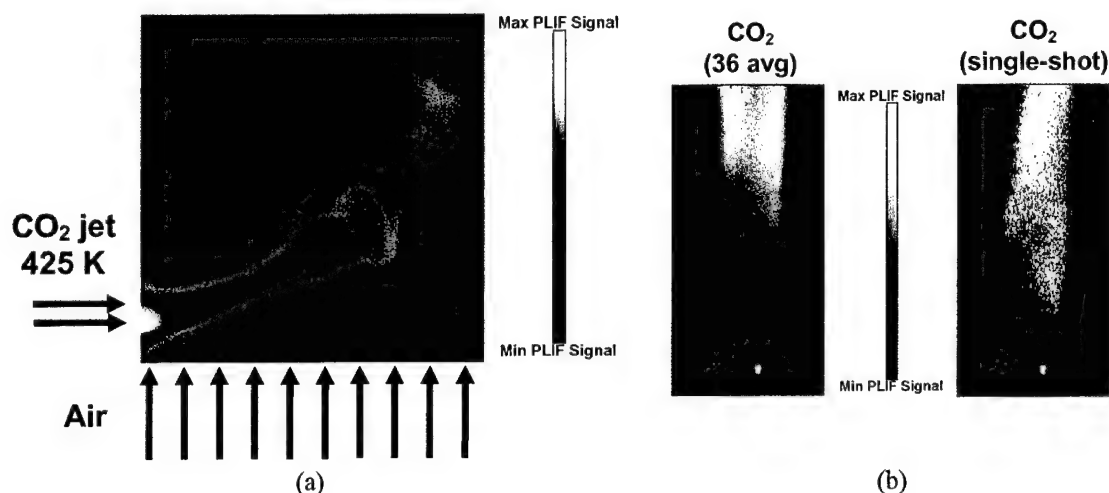


Fig. 2.4.7 (a) IR PLIF image of 425 K jet of CO<sub>2</sub> in air crossflow; (b) IR PLIF image of 50%CO/50%Ar (2% H<sub>2</sub> added for stability) flame.

In addition to visualization of low-temperature mixing processes, as shown in Fig. 2.4.7 (a), saturated IR PLIF of CO<sub>2</sub> is capable of imaging high temperature flows such as the flame fueled with 50%CO/50%Ar mixture (~2% H<sub>2</sub> added for stability) in Fig. 2.4.7 (b). The peak SNR for single-shot images was ~6 for these conditions, a value substantially less than those observed for the 425K jet due to the reduced number density in the flame. The minimum detectivity under these conditions was  $1.4 \times 10^{17}$  molecules/cm<sup>3</sup> (2% CO<sub>2</sub> mole fraction). The camera exposure time for these images was 1  $\mu$ s. As was discussed previously, for the high temperatures present in the flame  $\Psi_{\text{sat}}/T$  is almost constant, making the fluorescence nearly proportional to the CO<sub>2</sub> mole fraction.

#### References for section 2.4

- 2.4.1 Kirby, B.J. and Hanson, R.K., "Infrared PLIF Imaging of CO and CO<sub>2</sub>," *AIAA-99-0775* (1999).
- 2.4.2 Kirby, B.J. and Hanson, R.K., "Planar Laser-Induced Fluorescence Imaging of Carbon Monoxide Using Vibrational (Infrared) Transitions," *Appl. Physics B* **69**, 505-507 (1999).
- 2.4.3 Kirby, B.J. and Hanson, R.K., "Imaging of CO and CO<sub>2</sub> Using Infrared Planar Laser-Induced Fluorescence," *Proc. Comb. Inst.* **28**, 253-259 (2000).
- 2.4.4 Kirby, B.J. and Hanson, R.K., "CO<sub>2</sub> Imaging with Saturated Planar Laser-Induced Vibrational Fluorescence," *Appl Optics* **40**, 6136-6144 (2001).
- 2.4.5 Nesbitt, D.J. and Leone, S.R., "Infrared Fluorescence Studies of Intramolecular Vibrational Relaxation in C<sub>1</sub>-C<sub>4</sub> Hydrocarbons Following Pulsed Laser Excitation of the First CH Stretch Overtone," *Chem Phys Lett* **87**, 123-127 (1982).
- 2.4.6 Kirby, B.J. and Hanson, R.K., "Linear Excitation Schemes for IR Planar-Induced Fluorescence Imaging of CO and CO<sub>2</sub>," *Appl Optics* **41**, 1190-1201 (2002).

## 2.5 UV Absorption of CO<sub>2</sub>

### Background

UV absorption of hot H<sub>2</sub>O and CO<sub>2</sub> has been an important topic of study during the grant period, and three important results were obtained. Section 2.5.1 reports measurements of absorption cross sections made in high-temperature shock-heated flows, Section 2.5.2 describes work to understand the influence of this absorption on quantitative LIF measurements of NO, and Section 2.5.3 reports our initial investigation of the potential to extract the gas temperature from UV absorption measurements of CO<sub>2</sub> in the burnt gases of high-pressure combustors.

A few years ago, Knapp et al. [2.5.1], and more recently Hildenbrand et al. [2.5.2], discovered very strong laser attenuation during their attempts to make PLIF measurements of NO in the cylinder of piston engines. Although there were some previous measurements of UV absorption by high temperature CO<sub>2</sub> and H<sub>2</sub>O, these results were not well known to combustion researchers. There were previous measurements of UV absorption by shock-heated CO<sub>2</sub> and H<sub>2</sub>O at temperatures as high as 4500 K in the Russian literature [2.5.3,2.5.4], and, although this work was performed in the 1960s, the results were not published freely until 1990 when they found their way into a rather obscure translations journal [2.5.5]. Only a few other UV absorption measurements of heated CO<sub>2</sub> and H<sub>2</sub>O have been reported. The most extensive are the measurements in the astronomy literature of CO<sub>2</sub> absorption between 230 and 355 nm in an electrically heated furnace at four temperatures between 1500 and 2300 K [2.5.6], and CO<sub>2</sub> absorption measurements in the burnt gases of methane/oxygen flames at 1500 and 1700 K between 200 and 270 nm [2.5.7]. There was even less known about high temperature water vapor absorption. Only two 193 nm absorption measurements are published: in a heated flow between 300 and 1100 K [2.5.8] and in shock-heated gas for 1700 K < T < 3500 K [2.5.9].

The puzzling observation of strong UV attenuation in engines and the sparse literature on the subject motivated an investigation of high temperature UV absorption of the primary combustion products CO<sub>2</sub> and H<sub>2</sub>O. In section 2.5.1 we describe the temperature-dependent absorption cross section measurements for 1000 < T < 3300 K supported by this grant. [2.5.10] This work led to the realization that at high temperature and pressure, both CO<sub>2</sub> and H<sub>2</sub>O are significant absorbers of UV light at wavelengths below 200 nm.

These cross section results explain the difficulties reported in the literature by others in their attempts to make quantitative NO PLIF images at elevated pressure using D-X absorption of 193 nm ArF laser light (see section 2.5.2). Although room temperature CO<sub>2</sub> is transparent for wavelengths longer than 205 nm, we found that the CO<sub>2</sub> absorption spectrum is strongly temperature dependent and that at temperatures of 3000 K there is significant absorption for wavelengths as long as 350 nm. This temperature-dependent absorption significantly constrains the optimum LIF detection strategies for NO detection at elevated pressures (see section 2.5.2). However, the strong temperature dependence of this CO<sub>2</sub> absorption also provides a promising new opportunity for measuring temperature in hot, post-combustion flows (see section 2.5.3).

### 2.5.1 UV absorption cross sections for CO<sub>2</sub> and H<sub>2</sub>O

Motivated by the observation of strong UV attenuation in hot post combustion gases in piston engines at elevated pressures, absorption cross section measurements were made as a function of temperature for the primary combustion product CO<sub>2</sub> at temperatures between 880 and 3050 K and for H<sub>2</sub>O between 1230 and 2860 K [2.5.10]. The gases were shock-heated, and time-resolved absorption measurements were acquired using a kinetic spectrograph developed previously with partial support from this program and the Office of Naval Research. Detailed finite-rate chemistry was used to model the temporal evolution after the shock heating, enabling correction for the cooling of the test gas by thermal decomposition, and for changes in the gas composition. Above 2300 K these corrections become significant. The thermal decomposition of the target gas increases rapidly with increasing temperature, and by 3000 K more than 25% of CO<sub>2</sub> or H<sub>2</sub>O decompose within 1 ms. The measurements presented here cover the nominal temperature range (1000-3000 K) and the wavelength range (>190 nm) needed to model the absorption in hot, post-combustion gases for quantitative optical diagnostics.

Absorption measurements were made behind reflected shock waves (see fig. 2.5.1). Shock waves were generated in a high-purity turbo-pumped stainless steel shock tube, 15.24 cm in diameter. Reflected shock conditions were calculated from measured incident shock velocities using a standard ideal-gas chemically-frozen shock code [2.5.11]. First-order corrections to the highest temperature shocks were made from the kinetic modeling. Shock-heated samples of CO<sub>2</sub> or H<sub>2</sub>O diluted in argon provided a nearly stationary, isothermal gas sample for test times of 1-2 ms.

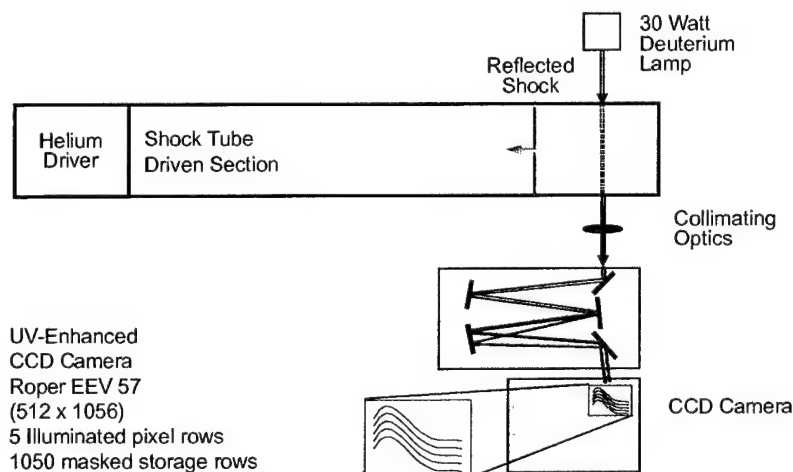


Fig. 2.5.1 Experimental setup

Gas samples of 2% CO<sub>2</sub> or 1.5% H<sub>2</sub>O diluted in argon were made manometrically with research grade gases. Absorption measurements were made through UV-grade fused silica windows centered 20 mm from the shock-tube end wall. Initial shock-tube pressures,  $P_1$ , ranged between 6 and 200 mbar, resulting in reflected shock pressures,  $P_5$ , of 0.7 – 7 bar (although the most of the data are acquired for  $P_5 = 1-2$  bar). Actual post-shock gas temperatures ranged from 880 to 3050 K.

The kinetic spectrograph provided absorption spectra from 190 to 320 nm with a 10  $\mu$ s time resolution. This diagnostics system was comprised of a deuterium lamp, collimating optics, monochromator, and a modified frame-transfer CCD camera. A deuterium lamp (Oriol, 30W) provided high-intensity ultraviolet light, which traversed the heated test gas and was focused at f/4 onto the entrance slit of a 150 mm imaging spectrometer (f/4 Acton), and was detected on an unintensified Lumogen-coated EEV 57 frame-transfer CCD camera (Roper Scientific). A mechanical mask covering all but the first 5 rows of pixels was installed to convert the fast-framing EEV 57 chip to a kinetics format. Every 2  $\mu$ s the pixels were displaced one row, and the five-row window produced a 10  $\mu$ s exposure time. The 2.9 nm (fwhm) spectral resolution was limited by the 150  $\mu$ m monochromator slit width. The optical setup was purged with N<sub>2</sub> to avoid the contribution of O<sub>2</sub> absorption.

The initial light intensity can be acquired immediately prior to firing the shock-tube, because the CO<sub>2</sub> or H<sub>2</sub>O is transparent at 300 K. The absorption cross section was derived from the Beer-Lambert Law,  $T(\lambda) = \exp(-\sigma(\lambda) N L)$ , with the number density  $N$  of CO<sub>2</sub> or H<sub>2</sub>O and the absorption path length  $L$ . Replicated measurements of the baseline intensity had an uncertainty of  $\pm 0.2\%$ ; thus, absorption cross sections were not derived for fractional absorption less than 0.5%.

The heated test gas was modeled with finite rate chemistry using GRI-Mech 3.0 [2.5.12] to determine the extent of thermal dissociation of the target CO<sub>2</sub> or H<sub>2</sub>O and the subsequent changes in the chemical composition versus time assuming constant internal energy and volume for the test gas. After 1 ms, less than 0.04% of the CO<sub>2</sub>, or less than 0.5% of the H<sub>2</sub>O, was dissociated for initial temperatures below 2300 K, and no corrections for reactive chemistry were applied to data at lower temperatures for either target gas.

At temperatures above 2300 K corrections for chemistry were required. Figure 2.5.2 shows the calculated variation of shock-heated CO<sub>2</sub> and dissociation products for an initial temperature of 3170 K. One ms after the shock, 30% of the CO<sub>2</sub> had decomposed, and the temperature had cooled by 230 K. We calculated the absorption cross section using the average value for CO<sub>2</sub> concentration and gas temperature during a 1ms test time, as justified by the nearly linear variation illustrated in Fig 2.5.2 for the highest temperature (thus largest thermal decomposition). These values were predicted by the model 500  $\mu$ s after the shock. Corrections also were made for absorption by the predicted quantities of dissociation products CO and O<sub>2</sub>. At the highest temperature reported, 3055 K, the O<sub>2</sub> correction at 190 nm accounts for 2.2% of the observed absorption, and CO accounts for 0.7%; at 220 nm both corrections are less than 0.05 %. Note that precise measurements of CO<sub>2</sub> absorption above 3000K will require precise knowledge of the thermal decomposition rate constant.

Similar model calculations for the thermal decomposition of H<sub>2</sub>O are illustrated in Fig. 2.5.3 at an initial temperature of 2900 K. Although 20% of the water had dissociated after 1 ms, the temperature cooled by only 80 K. Again we assumed that the average H<sub>2</sub>O concentration and temperature were the values 500  $\mu$ s after the shock and calculated the average absorption. At the highest temperature (2860 K) the observed absorption at

190 nm was corrected by 3% for absorption by the  $O_2$  formed in the post-shock chemistry.

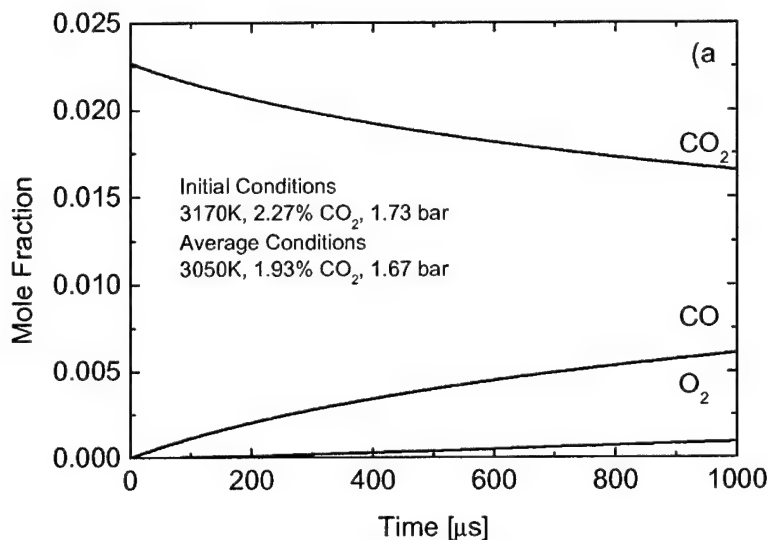


**Fig. 2.5.2** Model calculations:  $CO_2$  decomposition and  $CO$  and  $O_2$  production versus time after shock heating for  $T_s=3170$  K;  $T_{ave}=3050$  K

Precise measurements of the absorption cross sections for  $CO_2$  or  $H_2O$  above 3200 K require a significantly shorter measurement time because of the fast thermal decomposition. The 1 ms test time used here allows the light intensity to be averaged for precise measurements of  $I$  and  $I_0$ , and a decreased test time would require a more powerful UV lamp. Increasing the absorber number density can be used to reduce the test time for small absorption cross sections, but at wavelengths with large absorption cross sections we typically absorb 60% of the light, and an increase of the number density will reduce the precision.

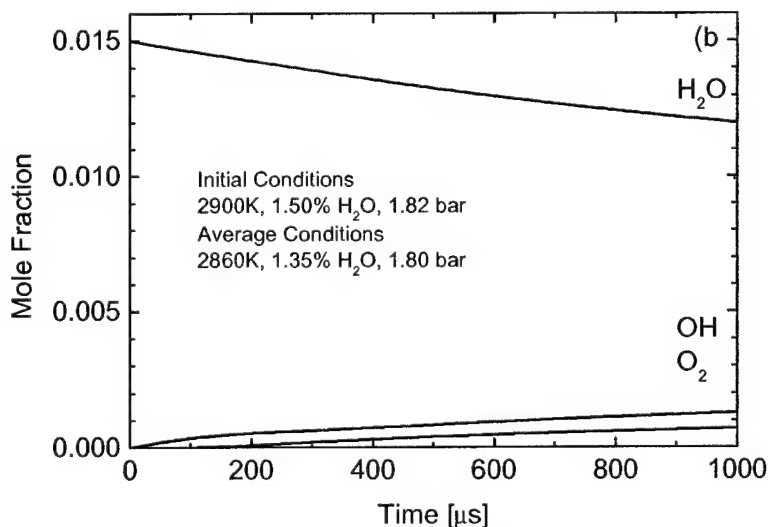


**Fig. 2.5.3** Model calculations:  $H_2O$  decomposition and  $OH$  and  $O_2$  production versus time after shock heating for  $T_s=2900$  K;  $T_{ave}=2860$  K.

The absorption cross section of CO<sub>2</sub> versus wavelength is plotted in Fig. 2.5.4. The top panel shows eleven temperatures that span the temperature range studied here. The measurements reported here are representative of the forty-six measurements conducted. Shocks at similar temperatures have excellent reproducibility, and no systematic variations with target gas density were observed. Consistent with the 2.9 nm spectral resolution, five-point adjacent averaging is used to smooth the data. We observe no spectral structure in the absorption cross section.

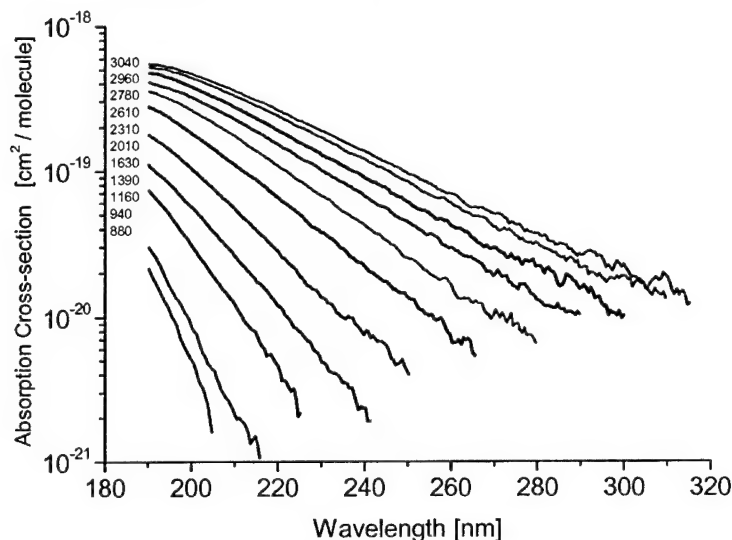


Fig. 2.5.4 Measured CO<sub>2</sub> absorption cross section for eleven temperatures

Our measured CO<sub>2</sub> absorption cross sections are in excellent agreement with the Russian measurements [2.5.4]. Even though published Russian work concentrates on measurements at high initial post-shock temperatures (up to 4500 K) where our chemical model predicts a large thermal decomposition that they neglect, their parameterization of the cross section agrees quite well with our data. (We assume they have reported the sign of  $A$  in their equation 9 and  $\theta$  in their equation 10 incorrectly.)

Our measurements are also in good agreement with the studies of Jensen et al. [2.5.6] at their lowest temperature (1523 K) measurement; however, as the temperature rises, they find a larger change in the cross section, and our measurements are 40% smaller at their highest temperature (2273 K). This deviation is significantly outside the statistical error that they report. Their cross section at 2073 K has the same magnitude and variation with wavelength as our measurement at 2310 K. We suspect they have an error in their temperature measurements and calculated path lengths; correction of their data using this assumption would account for the differences.

The CO<sub>2</sub> absorption cross section has quite strong temperature dependence. The measured 193 nm cross section at 2000 K is five orders of magnitude larger than the reported value at 300 K [2.5.13]. This variation may be the result of an increase in the transition probability for excited vibrational levels of CO<sub>2</sub>. Molecules in vibrationally excited bending or asymmetric stretching modes of the ground state have significantly better Franck-Condon overlaps with bent singlet and triplet valence excited electronic states.



Figure 2.5.5 shows the absorption of H<sub>2</sub>O versus wavelength for a set of representative temperatures between 1230 and 2860 K. Again, five-point smoothing is used, and no spectral structures are observed. A total of thirteen measurements were made, and six are shown here for clear presentation. The low-temperature data reported by Zuev and Starikovskii [2.5.5] is 25-40% lower than our measurements, as illustrated in Fig. 2.5.5 at 2000 K (squares) and 2800 K (circles). This disagreement is well within the combined uncertainty. The cross section for H<sub>2</sub>O absorption at 193 nm measured here improves upon earlier work by Davidson *et al.* [2.5.9]. The new measurements use lamp light with significantly lower fluence and a longer (1 ms) measurement time. Thus, we believe the new measurements are more accurate.

The uncertainties in the measured cross sections vary with their magnitude. At the smallest cross section values, the uncertainty was dominated by the uncertainties in  $I_0$  and illustrates the need for powerful broadband UV light sources. Replicated measurements of  $I_0$  indicate a total uncertainty of  $\pm 0.2\%$  over the wavelength range, and the analysis is limited to 0.5% measured absorption. Thus, the lowest cross sections

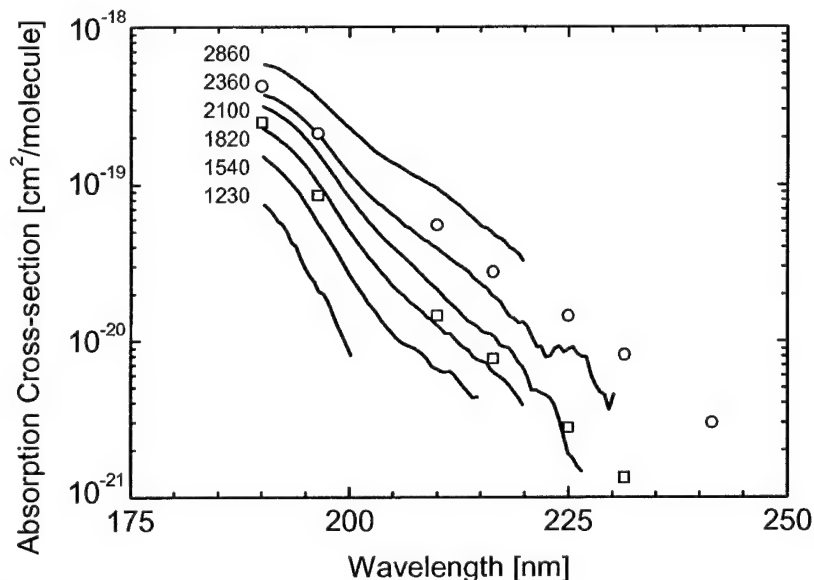


Fig. 2.5.5 Measured H<sub>2</sub>O absorption cross section for six temperatures (solid lines) and from ref. 5.5 at 2000 K (squares) and 2800 K (circles).

shown in Fig. 2.5.4 or 2.5.5 can have large errors. The estimated uncertainties for these measurements are sufficient to estimate the influence of CO<sub>2</sub> and H<sub>2</sub>O absorption on LIF measurements of NO in high-pressure combustors (see Section 2.5.2); however, more precise cross section data are desirable at selected wavelengths as the use of CO<sub>2</sub> absorption is developed into a temperature diagnostic (see Section 2.5.3).

## 2.5.2. UV absorption by hot H<sub>2</sub>O and CO<sub>2</sub>: A problem for high pressure NO LIF

The influence of ultraviolet (UV) light absorption by hot CO<sub>2</sub> and H<sub>2</sub>O was evaluated for laser-induced fluorescence (LIF) measurements of NO in high-pressure combustors [2.5.14]. UV lasers are used ubiquitously to measure LIF from species such as NO, OH, HCO, and O<sub>2</sub>, as well as Raman and Rayleigh scattering in combusting environments. However, the attenuation of the laser probe and/or signal by optical



absorption from major combustion species seldom is considered. Work done here reveals that neglecting UV attenuation by major product species (e.g.,  $\text{CO}_2$  and  $\text{H}_2\text{O}$ ) may lead to large errors in combustion measurements. In particular, the absorption cross section of  $\text{CO}_2$  has very strong temperature dependence and increases by four orders of magnitude at 193nm between 300 and 2000K. LIF measurements of NO in a high-pressure burner were adjusted for  $\text{CO}_2$  and  $\text{H}_2\text{O}$  absorption to demonstrate the importance of these corrections.

NO LIF was chosen as a test case to evaluate and illustrate the influence of optical absorption of  $\text{CO}_2$  and  $\text{H}_2\text{O}$  on UV combustion diagnostics. Excitation wavelengths for NO LIF range from 193 to 248nm. Each excitation has several possible detection wavelengths in the same range (see section 2.2). In high-pressure combustors we find significant absorption contributions to both the excitation laser and the fluorescence signal. The common excitation strategies for NO LIF use 193nm to excite D-X (0,1), 226nm for A-X (0,0), and 248nm for A-X (0,2). Each of these laser wavelengths is absorbed by hot combustion products  $\text{CO}_2$  and  $\text{H}_2\text{O}$ , as illustrated dramatically in Fig. 2.5.6. Using the newly measured absorption cross sections the attenuation for light at all three NO LIF excitation wavelengths is calculated as it traverses through the  $\text{CO}_2$  and  $\text{H}_2\text{O}$  combustion products at 13 bar and 2400K. This attenuation is plotted in Fig. 2.5.6 on a logarithmic scale, and the 193nm light intensity is found to decrease by a factor of  $10^8$  over the 7.5cm path. This severe attenuation serves to illustrate why previous workers have had significant difficulties trying to visualize NO distributions in high-pressure combustors with D-X excitation. Under the same conditions, the laser light is attenuated 91% for 226nm and 56% for 248nm, suggesting that these two LIF strategies are far more amenable than with 193nm excitation for practical high-pressure combustion diagnostics. The attenuation by NO self-absorption is not significant for these conditions (see below).

The high-pressure laminar flat-flame seeded with NO discussed above in section 2.2 is an ideal test bed to validate the quantitative understanding of absorption by major combustion products. Premixed methane/air flames at pressures between 1 and 60 bar were supported on an 8-mm stainless steel porous plug burner, and the flame was isolated by an air coflow. NO at 300 ppm was seeded into a stoichiometric methane/air mixture, and the LIF signal was collected from a horizontal collimated laser beam in the burnt gases of the flat flame. This fluorescence was dispersed in a small monochromator and detected on a 2-D CCD camera. Although there is a temperature gradient at the edges of the column of burnt gases, we assume a uniform adiabatic flame temperature and an equilibrium gas composition.

In addition to the correction for attenuation of the excitation laser, a correction also must be applied for the attenuation of signal light in the cylindrical engine volume. Measurements of NO LIF using three A-X excitation strategies are shown in Fig. 2.5.7 for a stoichiometric 40-bar flame: excite (0,0), detect (0,1); excite (0,1), detect (0,2); and excite (0,2), detect (0,1). The raw uncorrected NO LIF signal (dashed line) and the NO LIF signal corrected for  $\text{CO}_2$  and  $\text{H}_2\text{O}$  absorption (solid line) are shown as functions of position across the flame. Panel d shows the total attenuation correction, which ranges from 40% for the 226nm excitation to 20% for 248nm excitation. The curvature near the right side of the figure is due to the cylindrical geometry and the absorption of the fluorescence signal. When these corrections are applied to the three NO LIF raw signals

in panels a-c, we find that the NO LIF signal is symmetric, as expected in this cylindrical laminar flat flame. The NO self-absorption of the laser and fluorescence makes less than a 3% correction for these conditions and is neglected here. The temperature dependence of the quantum-state population in the level excited by the LIF is evident near the edge of the flame, where there is a temperature gradient. The excited feature at 226.03nm [ $P_1(23.5)$ ,  $Q_1+P_{21}(14.5)$ ,  $Q_2+R_{12}(20.5)$ ] is temperature-independent at flame temperatures, and the uniform seeding of NO in the flat flame near the burner surface is recovered by the absorption correction. The lower-state populations for the (0,1) and (0,2) LIF excitation transitions are progressively more temperature dependent in the temperature gradients near the edge of the flame. An added correction for the variation of the NO LIF signal with temperature in these two cases is required to recover the uniform NO distribution across the flames.

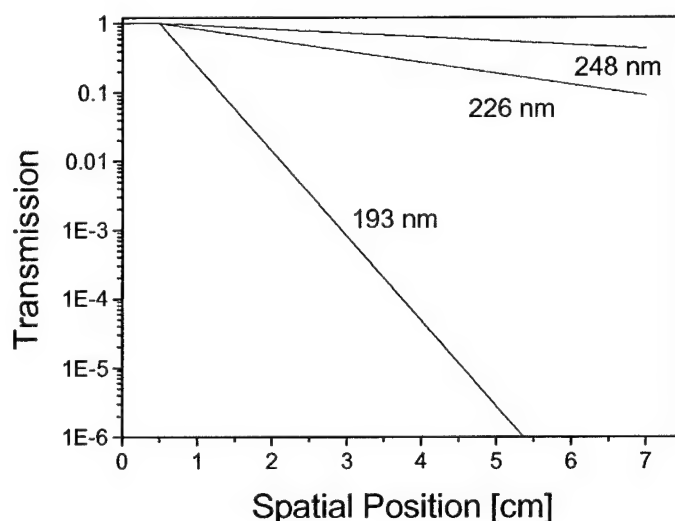


**Fig. 2.5.6** Absorption of input laser light at 193, 226, and 248nm versus distance from a the laser window located at 0.5cm for 13 bar of 2400K combustion products (9.4% CO<sub>2</sub>, 12.5% H<sub>2</sub>O, and 78.1% N<sub>2</sub>)

The absorption correction is dominated by CO<sub>2</sub> absorption for NO A-X absorption strategies. For (0,0) excitation the H<sub>2</sub>O absorption correction is less than 10% that for CO<sub>2</sub>, and the H<sub>2</sub>O contribution to the absorption correction is even smaller for (0,1) and (0,2) excitation. However, quantitative measurements of NO LIF require correction for both CO<sub>2</sub> and H<sub>2</sub>O absorption.

For most flames NO self-absorption is small compared to that by hot CO<sub>2</sub>; however, its contribution is pressure-dependent. The NO LIF excitation spectrum is resolved rotationally at 1 bar, whereas, the CO<sub>2</sub> and H<sub>2</sub>O absorptions are broad and unstructured, as seen in Fig. 2.5.4 and 2.5.5. Thus, increased pressure tends to reduce the peak NO self-absorption, but the unstructured absorption by CO<sub>2</sub> and H<sub>2</sub>O is not affected. For example, as the pressure of a stoichiometric flame (2200K) increases from 1 to 20 to 40 bar, the CO<sub>2</sub> absorption at 226nm is equivalent to the NO self-absorption by 2700, 6500, and 10500-ppm, respectively. Thus, for high-pressure and high-temperature measurements in practical combustors, self-absorption by 500ppm NO is less than 10% of the absorption by typical CO<sub>2</sub> combustion products.

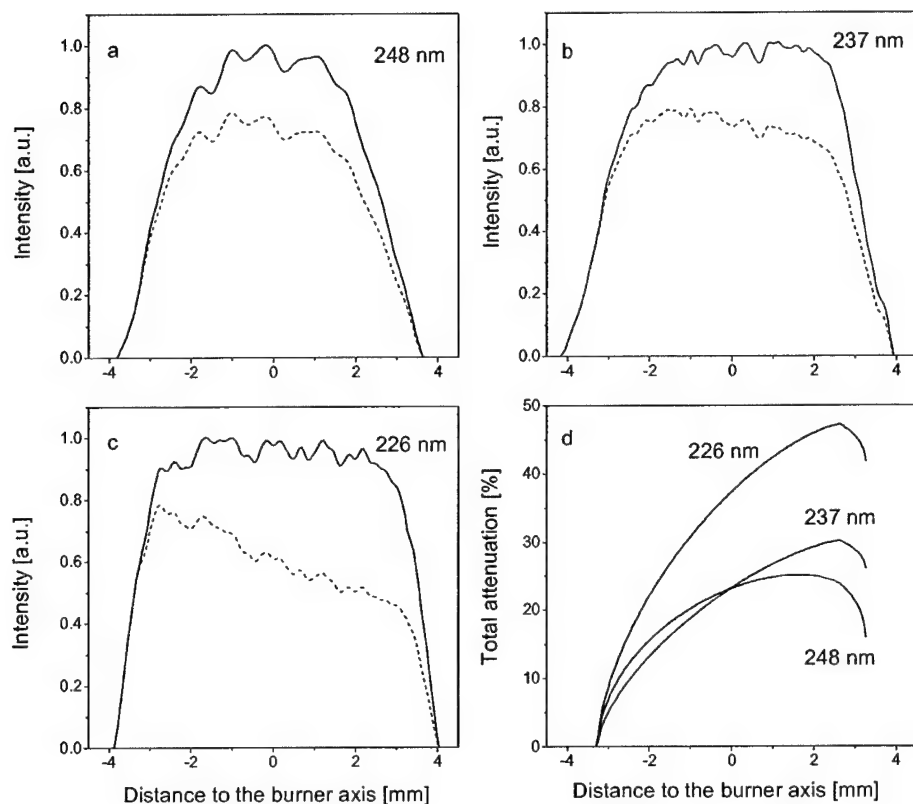


**Fig. 2.5.7** NO LIF raw signal (dashed lines) and corrected for  $\text{CO}_2$  and  $\text{H}_2\text{O}$  absorption (solid lines) above a premixed laminar flat-flame at 40-bar using A-X transitions: (a) excite (0,2), detect (0,1); (b) excited (0,1), detect (0,2); (c) excite (0,0), detect (0,2); (d) correction factors for laser and signal absorption assuming cylindrical symmetry.

The measurements of  $\text{CO}_2$  and  $\text{H}_2\text{O}$  absorption cross sections reported in Section 2.5.1 indicated that absorption by hot combustion products requires significant correction to UV diagnostics below 250nm at elevated pressures. NO LIF schemes were examined to investigate quantitatively the impact of absorption UV diagnostics in high-temperature flame gases. The  $\text{H}_2\text{O}$  and  $\text{CO}_2$  absorption is so strong at 193nm that the use of D-X (0,1) excitation of NO LIF is quite problematic in practical combustors. Quantitative NO LIF with A-X excitation requires correction of both the laser excitation light and the fluorescence signal.

### 2.5.3 UV absorption by hot $\text{CO}_2$ : An opportunity for temperature measurements

Because both the magnitude of the  $\text{CO}_2$  absorption cross section and the shape of the UV absorption spectrum vary strongly with temperature and because  $\text{CO}_2$  is present at large mole fractions in combustion effluents, measurements of the UV optical absorption spectra offer the potential to infer gas temperature in combustion systems. Recently, preliminary measurements were made to demonstrate this potential [2.5.15]: (1) Transmission measurements of cw laser light at 266nm were used to determine the time-resolved temperature in shock-heated  $\text{CO}_2$ . (2) Similar transmission measurements were used to infer the time-resolved temperature behind a detonation wave in a pulse-detonation engine using the absorption from equilibrium concentrations of the  $\text{CO}_2$

combustion product. These examples demonstrate that temperature measurements based on UV optical absorption of CO<sub>2</sub> have good potential for use in a wide variety of hydrocarbon combustion applications.

The temperature dependence in the CO<sub>2</sub> cross section shown in Fig. 2.5.4 illustrates the potential to infer temperature ( $T$ ) from the UV absorption of CO<sub>2</sub>. CO<sub>2</sub> is a major product of hydrocarbon combustion and thus is present in significant quantities in the hot burnt gases. For many practical systems, the pressure and the feedstock gas composition are known, and the CO<sub>2</sub> concentration is in chemical equilibrium. For such a system, we demonstrate that a measurement of the UV attenuation at a single wavelength can be used to determine the temperature. However, both the magnitude of the absorption cross section and the shape of the absorption spectrum vary with temperature. Thus, in systems with unknown CO<sub>2</sub> concentration, the temperature can be determined via attenuation measurements at two or more wavelengths.

Measurement of  $T$  from UV absorption of CO<sub>2</sub> provides a new diagnostic tool complementing other laser-based optical techniques. Like other absorption methods, the most straightforward application provides path-integrated temperature. Such measurements do not have the spatial resolution offered by LIF; however, absorption-based measurements can provide real-time measurements with the potential for control applications, and the optical access requirements are modest, offering the potential for measurements in production engines or industrial applications. The CO<sub>2</sub> absorption diagnostic discussed here is most applicable to high temperatures and pressures, which is a regime where other optical methods (especially LIF) have great difficulty. The CO<sub>2</sub> absorption signal is strongest at high  $T$  and thus is relatively immune to the interference from the dense, cold boundary layers that are a problem for Rayleigh and Raman methods.

### **The Temperature Measurement Strategy**

Optical absorption of light at wavelength  $\lambda$  and intensity  $I_0$  by a mole fraction  $X_i$  of species  $i$  in a gas of density  $n$  at pressure  $p$  can be written:

$$I(\lambda) = I_0(\lambda) \exp\left(-\int_0^l \sigma_i(\lambda, T) X_i(T, x) n(p, T, x) dx\right) \quad (2.5.1)$$

where  $I$  is the transmitted intensity,  $\sigma_i$  is the absorption cross section (a function of  $\lambda$  and  $T$ ), and, in general,  $X_i$  and  $n$  vary with position along the path  $dx$  with total length  $l$ .

For CO<sub>2</sub>, the cross section  $\sigma$  was fitted in the range 200-320nm and 900-3050K to a semi-empirical form:

$$\ln \sigma_{\text{CO}_2}(\lambda, T) = a + b \lambda \quad (2.5.2)$$

where  $a = c_1 + c_2 T + c_3/T$  and  $b = d_1 + d_2 T + d_3/T$ . The cross section is given in units  $10^{-19} \text{cm}^2$ , with  $T$  in 1000 K,  $\lambda$  in 100nm, and  $c_1=17.2456$ ,  $c_2=-3.1813$ ,  $c_3=0.8836$ ,  $d_1=-7.0094$ ,  $d_2=1.6142$ , and  $d_3=-3.1777$  [2.5.14].

For the measurements below, except for a thin cold boundary layer,  $p$ ,  $T$ , and  $X_{\text{CO}_2}$  are all constant over the path length, the number density is expressed as an ideal gas ( $pV=nRT$ ), and the absorbance  $A_\lambda$  becomes:

$$A_\lambda = \ln \left( \frac{I_0(\lambda)}{I(\lambda)} \right) = X_{\text{CO}_2}(T) \frac{pV}{RT} l \sigma(T, \lambda). \quad (2.5.3)$$

For known  $\text{CO}_2$  concentrations and  $p$ , the measured absorbance at a single wavelength can be used directly to infer  $T$ . Fig. 2.5.8 shows  $A_\lambda$  at 266 nm versus  $T$  for a 2%  $\text{CO}_2$  mixture at 1bar for a 15cm path length.

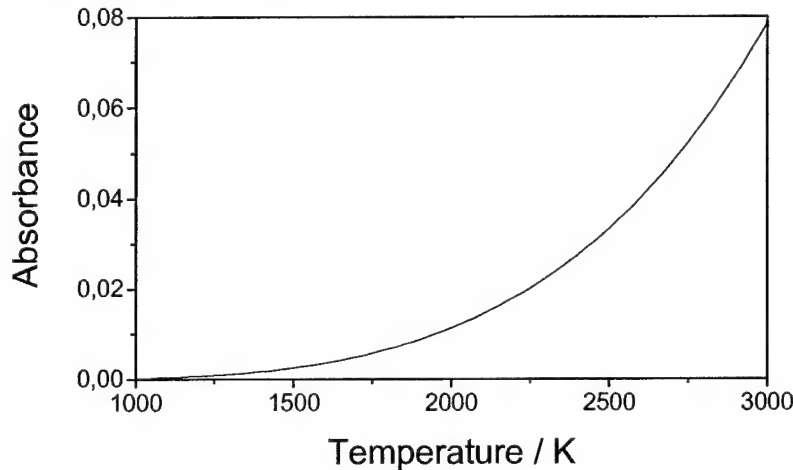


**Fig. 2.5.8** Absorbance expected from equations (2) and (3) for 2%  $\text{CO}_2$  in argon across (15.24cm) the shock tube at 266 nm from 1000-3000K.

A mixture of 2%  $\text{CO}_2$  diluted in argon is heated by a gas-driven incident shock and subsequent reflected shock, providing a nearly stationary, isothermal gas sample. The experiment is performed in a high-purity, turbo-pumped, stainless steel shock tube (15.24cm diameter) illustrated in Fig. 2.5.1. The initial reflected shock wave conditions were calculated from measured incident shock speeds using standard ideal-gas shock wave relations. Fig. 2.5.9 shows these ideal pressure and temperature ( $p_5$  and  $T_5$ ) conditions

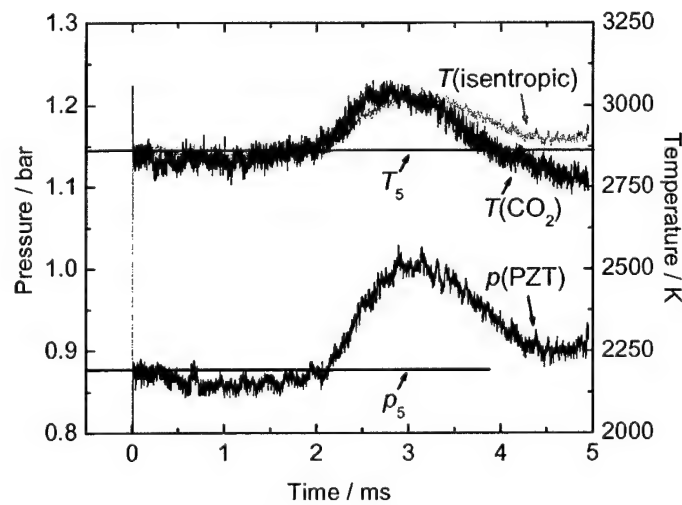


**Fig. 2.5.9** Time-resolved temperature and pressure measured in shock-heated mixture of 2%  $\text{CO}_2$  in Ar. Time zero is the arrival of the reflected shock. The horizontal lines mark the  $T_5$  and  $p_5$  temperature and pressure expected from shock heating an ideal gas.

as straight lines at 0.876 bar and 2867K. For this gas mixture and reflected-shock  $T$ , there is no appreciable  $\text{CO}_2$  thermal decomposition. The pressure is measured by a high-speed piezo-electric transducer. After 2ms, a pressure rise to  $\sim 1.0$  bar is observed. This pressure rise originates from an interaction of the reflected shock with the contact surface between the driver gas (He) and the test gas mixture. For the non-reactive gas mixture  $T$  can be calculated from the measured pressure trace assuming an isentropic process.

The attenuation of 266nm cw laser light by the heated  $\text{CO}_2$  is used to infer the time-resolved  $T$  after the reflected shock passes (time zero in Fig. 2.5.9). The output of a frequency-doubled, diode-pumped, cw Nd:YAG laser (Coherent, 5W@532nm) is doubled in an external BBO crystal, providing  $\sim 1\text{mW}$  of light at 266nm. This laser light passes un-attenuated across the shock tube in the room-temperature test gas, but undergoes  $\sim 2.5\%$  attenuation after the reflected shock passes. The observed attenuation, together with the measured  $p$  and the  $T$ -dependent  $\text{CO}_2$  absorption cross section, provides the gas temperature with  $1\mu\text{s}$  time-resolution that agrees with the ideal gas  $T$ -prediction within 1% at time zero. The resulting  $T$  agrees ( $\pm 30\text{K}$ ) with the simulated  $T$  until approximately 3.5ms after the shock, when the isentropic assumption breaks down. This measurement illustrates the potential to use  $\text{CO}_2$  absorption to extract precise time-resolved gas temperature.

The attenuation of the 266nm cw laser radiation in the combustion gases behind a detonation wave in a pulse detonation engine (PDE) provides the time-resolved gas  $T$ , as shown in Fig. 2.5.10. The experiment is performed in the Stanford PDE, which is 3.8cm in diameter and 160cm in length and instrumented with a variety of optical access, pressure, and ion probe ports. The tube is fueled at 1bar with premixed, stoichiometric  $\text{C}_2\text{H}_4/\text{O}_2$ , as monitored with a tunable diode laser sensor [2.5.16]. The 266nm laser absorption is measured 144cm from the head end of the tube. There is no attenuation prior to the detonation wave, and significant attenuation is observed after the detonation wave arrives, when  $p$  and  $T$  rise to Chapman-Jouguet (CJ) values of  $\sim 40\text{bar}$   $\sim 3930\text{K}$ . This temperature exceeds the temperature range for which  $\text{CO}_2$  absorption cross section data are reported in ref. [2.5.10] and are outside the valid  $T$ -range of equation (2) [2.5.14]. Therefore, the needed high- $T$  (3000-4500K)  $\text{CO}_2$  absorption cross section data were measured at 266nm in a shock tube with known  $\text{CO}_2$  concentrations. Variations in  $\text{CO}_2$

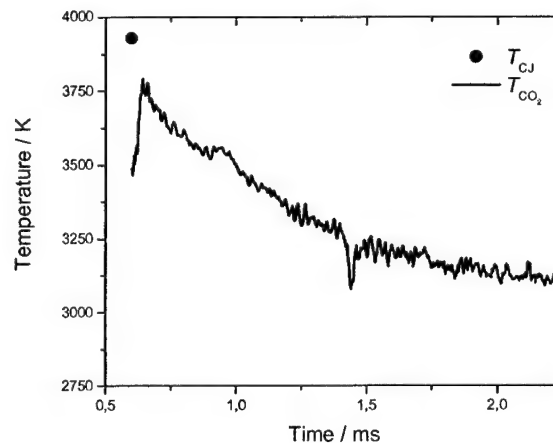


**Fig.2.5.10** Time-resolved gas temperature in the gases behind a detonation wave in a stoichiometric  $\text{C}_2\text{H}_4/\text{O}_2$  mixture. The point denotes the CJ value.

concentration due to thermal decomposition were taken into account by extrapolating the measured attenuation to  $t=0$ . Work to refine the cross section data to increase the temperature range and provide precise data for selected wavelengths is underway.

The peak  $T$  inferred from  $\text{CO}_2$  absorption in the PDE is 3850K. Given the difficulties of optical measurements disrupted by the passage of a detonation wave (and a pressure change from 1 to 40bar) and the large values of 266nm absorbance, we consider this measurement in good agreement with the Chapman-Jouguet prediction. A second laser beam near 390nm, where the gas is transparent is used to account for the beam steering by the denotation wave. The pressure is measured independently using a pressure transducer. The absorption-based  $T$  is an absolute measurement that does not rely on any calibration. Only the assumption that the  $\text{CO}_2$  concentration is in chemical equilibrium is needed. Finite rate chemical modeling suggests that the  $\text{CO}_2$  concentration in the post-detonation gases reaches equilibrium with a sub- $\mu\text{s}$  time constant, thus confirming the use of an equilibrium assumption to reduce the 266nm absorption data. Fig. 2.5.10 shows the time-resolved measurements as the pressure drops from the Chapman-Jouguet value to  $\sim 3\text{bar}$  and  $T$  drops to  $\sim 3000\text{K}$ . There is good agreement between recent computational model predictions and measurements of  $T$  [2.5.17].

The  $T$ -dependence of  $\text{CO}_2$  absorption in the UV is used for the first time to determine the gas temperature. Experimental demonstration experiments were conducted to illustrate the potential for precise, time-resolved,  $T$ -measurements in the burnt gases of hydrocarbon combustion applications. The shock-heated  $\text{CO}_2$  temperature is well known shortly after the reflected shock, and these measurements validate the  $\text{CO}_2$  absorption thermometry technique. The  $\text{CO}_2$  absorption measurements yield values in very good agreement ( $\pm 50\text{-}100\text{K}$ ) with the expected result. The predicted CJ  $T$  of the detonation experiment is only 100K above the  $\text{CO}_2$  absorption-based temperature that assumes chemical equilibrium. Therefore, we conclude that  $\text{CO}_2$  absorption-based determination of gas  $T$  has excellent promise for precise gas temperature measurements above 1500K, including systems with elevated pressure. Three of the examples are at high pressure (premixed flame, pulse detonation engine, and piston engine), and the two engine examples show the utility of this new  $T$  diagnostic for time-resolved measurements where  $p$  and  $T$  vary rapidly in time.

The excellent potential of this temperature diagnostic suggests the value of further research to extend the utility and operating regime of  $\text{CO}_2$  UV absorption-based temperature measurement. For the evaluation of detonation temperatures, the absorption cross sections must be determined up to 4500K. Furthermore, the extension of the absorption cross section data base to longer wavelengths (320-400nm) might provide excellent diagnostics possibilities in long path-length practical combustors.

### **References for section 2.5**

- 2.5.1 Knapp, M., Luczak, A., Schlüter, H., Beushausen, V., Hentschel, W., Andresen, P., "Crank-Angle-Resolved Laser-Induced Fluorescence Imaging of NO in a Spark-Ignition Engine at 248 nm and Correlations to Flame Front Propagation and Pressure Release," *Appl. Opt.*, **35**, 4009-417 (1996).
- 2.5.2 Hildenbrand, F., Schulz, C., Sick, V., Wagner, E., "Investigation of Spatially Resolved Light Absorption in a Spark-Ignition Engine Fueled with Propane/Air," *Appl. Opt.* **38**, 1452-1458 (1999); Hildenbrand, F., Schulz, C. "Measurements



- and Simulation of In-Cylinder UV-Absorption in Spark Ignition and Diesel Engines," *Appl. Phys.* **B73**, 165 (2001).
- 2.5.3 Generalov, N.A. Losev, S. A. Maksimenko, V.A., "The Decomposition of Carbon Dioxide Molecules at High Temperatures," *Dokl. Akad. Nauk. SSSR*, **150**, 839-841(1963).
  - 2.5.4 Losev, S.A. and Terebenia, L.B. "The Kinetics of the Dissociation of Carbon Dioxide Molecules Behind a Shock Wave," *Zh. Prikl. Mekh. Tekh. Fiz*, **4** (1966) 133-138.
  - 2.5.5 Zuev, A.P. and Starikovskii, A.Yu., Absorption Cross Sections of Molecular Oxygen, Nitrogen Monoxide, Nitrous Oxide, Carbon Dioxide, Water, and Nitrogen Dioxide in the UV Spectral Range," *J. Appl. Spectrosc.*, **52** (1990) 304-313.
  - 2.5.6 R.J. Jensen, R.D. Guettler, J.L. Lyman, "The Ultraviolet Absorption Spectrum of Hot Carbon Dioxide," *Chem. Phys. Lett.*, **277** (1997) 356-360.
  - 2.5.7 T. Joutsenoja, A. D'Anna, A. D'Alessio, M.I. Nazzaro, "Ultraviolet absorption spectra of carbon dioxide and oxygen at elevated temperatures," *Appl. Spect.*, **55** (2001) 130-135.
  - 2.5.8 W. J. Kessler, K.L. Carleton, W.J. Marinelli, "Absorption coefficients for water vapor at 193 nm from 300 to 1073 K," *J. Quant. Spectrosc. Radiat. Transfer*, **50** (1993) 39-46.
  - 2.5.9 D.F. Davidson, A.Y. Chang, K. Kohse-Höinghaus, R.K. Hanson, , "High Temperature Absorption Coefficients of O<sub>2</sub>, NH<sub>3</sub> and H<sub>2</sub>O for Broadband ArF Excimer Laser Radiation," *J. Quant. Spectrosc. Radiat. Transfer*, **42** (1989) 267-278.
  - 2.5.10 C. Schulz, J.D.Koch, D.F. Davidson, J.B.Jeffries, and R.K. Hanson, "Ultraviolet Absorption Spectra of Shock-Heated Carbon Dioxide and Water between 900 and 3050 K," *Chem Phys Lett*, **355**, 82-88 (2002).
  - 2.5.11 G Ben-Dor, O. Igra, T. Elperin eds., **Handbook of Shock Waves** Vols. 1-3, Academic Press San Diego 2001.
  - 2.5.12 G P. Smith, D. M. Golden, M. Frenklach, N. W. Moriarty, B. Eiteneer, M. Goldenberg, C. T. Bowman, R. K. Hanson, S. Song, W. C. Gardiner, V. Lissianski, Z. Qin: *GRI-Mech 3.0 web site*, [http://www.me.berkeley.edu/gri\\_mech/](http://www.me.berkeley.edu/gri_mech/) (1999).
  - 2.5.13 M. Ogawa, "Absorption Cross Sections of O<sub>2</sub> and CO<sub>2</sub> Continua in the Schumann and Far-uv Regions," *J. Chem. Phys.* **54**, (1971) 2550-2556.
  - 2.5.14 C. Schulz, J.B. Jeffries, D.F. Davidson, J.D. Koch, J. Wolfrum, and R.K. Hanson, "Impact of UV Absorption by CO<sub>2</sub> and H<sub>2</sub>O on NO LIF in High-Pressure Combustion Applications," *Proc. Combust. Inst.*, **29**, 2735-2742 (2002).
  - 2.5.15 J.B. Jeffries, C. Schulz, D.W. Mattison, M.A. Oehlschlaeger, W.G. Bessler, T. Lee, D.F. Davidson, and R.K. Hanson, "UV Absorption of CO<sub>2</sub> for Temperature Diagnostics of Hydrocarbon Combustion Applications," *Proc. Combust. Inst.*, **30**, (2004) in press.
  - 2.5.16 L. Ma, S.T. Sanders, J.B. Jeffries, R.K. Hanson, "Monitoring and Control of a Pulse Detonation Engine Using a Diode-Laser Fuel Concentration and Temperature Sensor," *Proc. Combust. Inst.* **29**, 161-166 (2002).
  - 2.5.17 D.W. Mattison, M.A. Oehlschlaeger, C.I. Morris, Z.C. Owens, E.A. Barbour, J.B. Jeffries, R.K. Hanson, "Evaluation of Pulse Detonation Engine Modeling using Laser-Based Temperature and OH Concentration Measurements," *Proc. Combust. Inst.* **30**, (2004) in press.



## 2.6 Multiphase Diagnostics Based on Wavelength-Multiplexed Laser Extinction

The wide use of liquid fuels in many propulsion systems calls for advanced diagnostics that are capable of rapid and reliable characterization of fuel spray, fuel vapor concentration, and temperature. In this research program we: 1) developed a next generation laser diagnostic technique capable of near-real-time simultaneous characterization of droplet size, droplet volume fraction, vapor concentration, and vapor temperature in spray combustion systems; 2) designed and built an optically-accessible aerosol shock tube (partially supported by ARO) to prompt development of this diagnostic technique for studies of liquid fuel combustion; and 3) demonstrated the feasibility and utility of the diagnostic technique in a series of experiments in the aerosol shock tube facility and obtained encouraging preliminary results.

### Measurement Concepts

Previous research efforts [Ref. 2.6.1] recognized that monitoring extinction at two wavelengths could enable measurement of fuel vapor concentration in the presence of droplets. Not until now, however, has it become feasible to contemplate the potential benefits of extending this concept to include laser sources at an arbitrary number of wavelengths, each of which might be rapidly tunable over some spectral domain. This general wavelength multiplexing concept has considerable potential to improve the time response and accuracy of droplet size measurements, to increase the sensitivity of rapid vapor concentration measurements, and to realize simultaneous vapor temperature measurement.

Optical diagnostics for the simultaneous monitoring of multiphase fuels are complex in that vapor absorption and droplet extinction are coupled, as shown in the following equation:

$$\begin{aligned} \text{Transmission} = T(\lambda) &= \frac{I_t}{I_o} \\ &= \exp[-\tau_{\text{vapor}}(\lambda)] \cdot \exp[-\tau_{\text{drops}}(\lambda)] = \exp[-\alpha(\lambda) \cdot X \cdot L] \cdot \exp[-\tau_{\text{drops}}(\lambda)] \end{aligned} \quad (2.6.1)$$

In this equation,  $I_o$  and  $I_t$  are the incident and transmitted beam intensity, respectively,  $T(\lambda)$  the optical transmittance at wavelength  $\lambda$ ,  $\tau_{\text{vapor}}(\lambda)$  the vapor absorbance,  $\tau_{\text{drops}}(\lambda)$  the droplet extinction (including scattering and liquid absorption),  $\alpha(\lambda)$  the absorption coefficient of vapor,  $X$  the vapor concentration, and  $L$  the sample pathlength. In order to extract droplet and vapor information, the contribution of vapor absorption and droplet extinction must be decomposed. For the present purposes, we consider  $\alpha(\lambda)$  and  $X$  to be spatially uniform along the line of sight.

Fig. 2.6.1 depicts our approach based on wavelength-multiplexing to decouple droplet and vapor effects. At wavelengths where vapor does not absorb ( $\lambda_1$  and  $\lambda_2$  in Fig. 2.6.1), the optical transmittance is only due to droplet extinction and is given by (under the assumption that droplets are spherical):

$$T(\lambda) = \exp[-\tau_{drops}(\lambda)] = \exp\left[-\frac{3}{2} \cdot \frac{Q(\lambda, D_{32})}{D_{32}} \cdot C_v \cdot L\right] \quad (2.6.2)$$

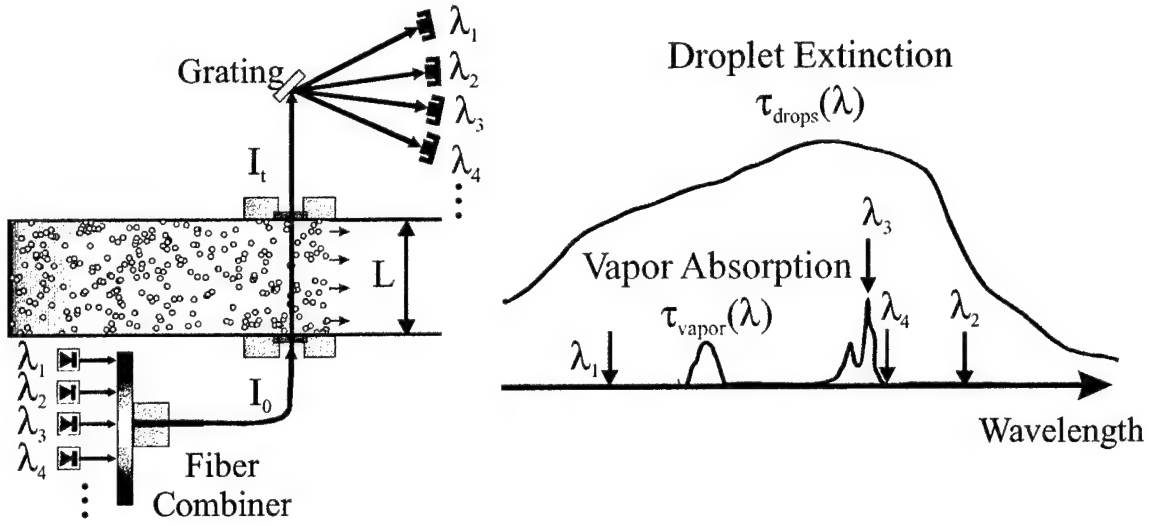


**Fig. 2.6.1** Schematic of wavelength-multiplexed sensor for simultaneous droplet and vapor measurement using a *differential absorption* strategy.

In this equation  $C_v$  is the volume fraction of droplets,  $D_{32}$  the line-of-sight average Sauter Mean Diameter (SMD) [Ref. 2.6.2] along the optical pathlength, and  $Q(\lambda, D_{32})$  the Mie scattering coefficient at wavelength  $\lambda$ . Previous studies show that  $Q(\lambda, D_{32})$  depends very weakly on the droplet size distribution for most common distribution functions [Ref. 2.6.2]. Therefore, the droplet size can be measured based on equation (2.6.2) with reasonable accuracy without knowing the droplet size distribution if  $C_v$  is known. In most cases  $C_v$  is unknown, and transmittance measurements at multiple wavelengths are needed. From equation (2.6.2) we obtain:

$$\frac{\ln T(\lambda_1)}{\ln T(\lambda_2)} = \frac{Q(\lambda_1, D_{32})}{Q(\lambda_2, D_{32})} \quad (2.6.3)$$

For given  $\lambda_1$  and  $\lambda_2$ , the right-hand side of equation (3) is a function of  $D_{32}$  and can be computed from Mie scattering theory. Hence by measuring the extinction ratio at multiple wavelengths (a minimum of two wavelengths, but more as needed to obtain a unique result) and solving equation (3), the droplet size can be inferred.

Feasibilities studies of this droplet sizing technique have been conducted in a small-scale facility ( $L=10$  cm). Fig. 2.6.2 shows an example result. In this experiment, a three-wavelength diode laser sensor probed an evaporating ethanol spray to measure the droplet size at different locations along the spray [Ref. 2.6.3]. The measurements from the diode laser sensor are compared with the measurements from a Malvern Particle Sizer (MPS), and good agreement is found. The time response of the sensor in this experiment is 1  $\mu$ s.

Theoretically, the vapor concentration could be obtained from the measurement of extinction at a single wavelength where the vapor absorbs, once the contribution from droplet extinction is known. However, this method is not applicable to many practical

applications where the contribution from droplet extinction is much larger than that from vapor absorption (i.e.,  $\tau_{\text{drops}} \gg \tau_{\text{vapor}}$ ) and the transmitted intensities may contain noise (e.g. due to beamsteering). Hence, we have sought an alternative strategy that improves the vapor detection limit. Our approach for vapor sensing takes advantage of the fact that in the droplet size range of practical propulsion systems the vapor spectra vary much more strongly with wavelength than the droplet extinction, therefore allowing a sensitive “differential absorption” measurement of vapor concentration. This concept is illustrated schematically in Fig. 2.6.1, with  $\lambda_3$  and  $\lambda_4$  as the vapor detection wavelengths.

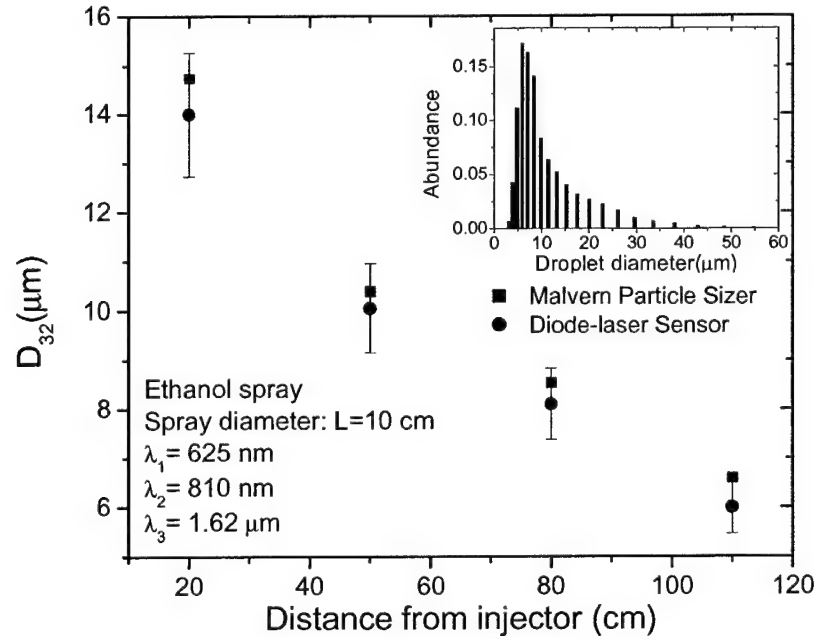


Fig. 2.6.2 Comparison of droplet size measured with diode-laser sensor and with Malvern Particle Sizer. Inset shows droplet size distribution measured by MPS 50 cm from the injector.

While extinction due to droplets exceeds the extinction due to vapor absorption (i.e.  $\tau_{\text{drops}}(\lambda_3) > \tau_{\text{vapor}}(\lambda_3)$  and  $\tau_{\text{drops}}(\lambda_4) > \tau_{\text{vapor}}(\lambda_4)$ ), thus prohibiting accurate vapor detection at a single wavelength, the *differential* vapor absorption between  $\lambda_3$  and  $\lambda_4$  can be comparable or larger than the *differential* droplet extinction (i.e.  $\tau_{\text{vapor}}(\lambda_3) - \tau_{\text{vapor}}(\lambda_4) > \tau_{\text{drops}}(\lambda_3) - \tau_{\text{drops}}(\lambda_4)$ ) if  $\lambda_3$  and  $\lambda_4$  are well-designed, therefore enabling sensitive vapor measurement. The differential absorption method may be generalized to include a large number of detection wavelengths, and this approach may allow further improvement in the vapor detection limit, as well as a possible strategy for simultaneous measurements of vapor temperature. Implementation of such a vapor sensor will require accurate knowledge of the absorption spectra and their temperature dependence.

Our initial experiments have demonstrated the high sensitivity of this technique for various hydrocarbon fuel vapors, and our calculations show the promise of this technique as a solution for the detection of vapor in fuel sprays. As an example, fundamental spectroscopic studies of ethanol vapor in the near IR spectral range have been conducted, as shown in Fig. 2.6.3, to optimize the wavelengths for ethanol vapor measurement by differential absorption. The selected wavelengths, 1.3927 and 1.3922  $\mu\text{m}$ , maximize the differential vapor absorption signal, while avoiding interference

absorption from water vapor. Fig. 2.6.4 shows the performance of the differential absorption sensor based on these wavelengths for ethanol vapor with two different initial droplet sizes.

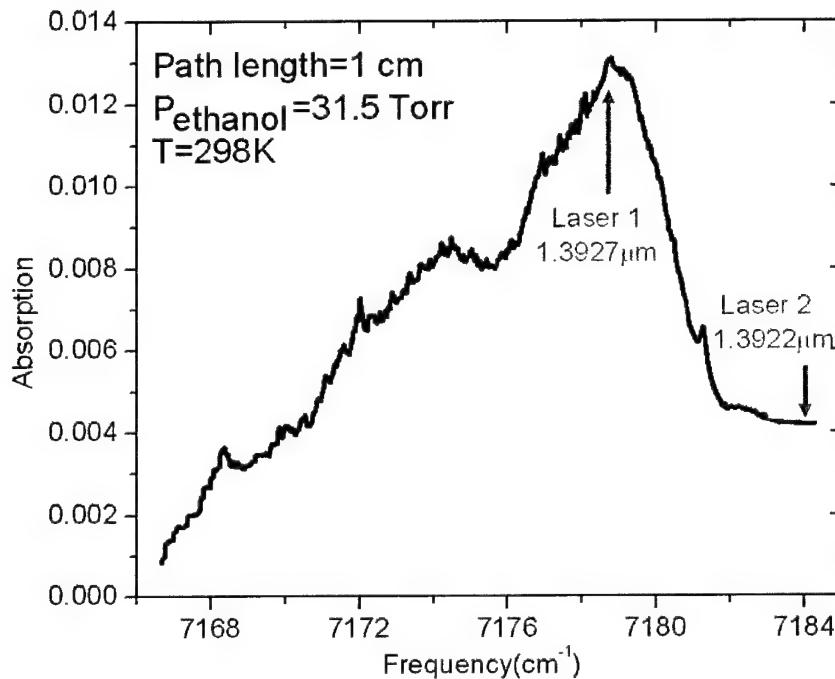
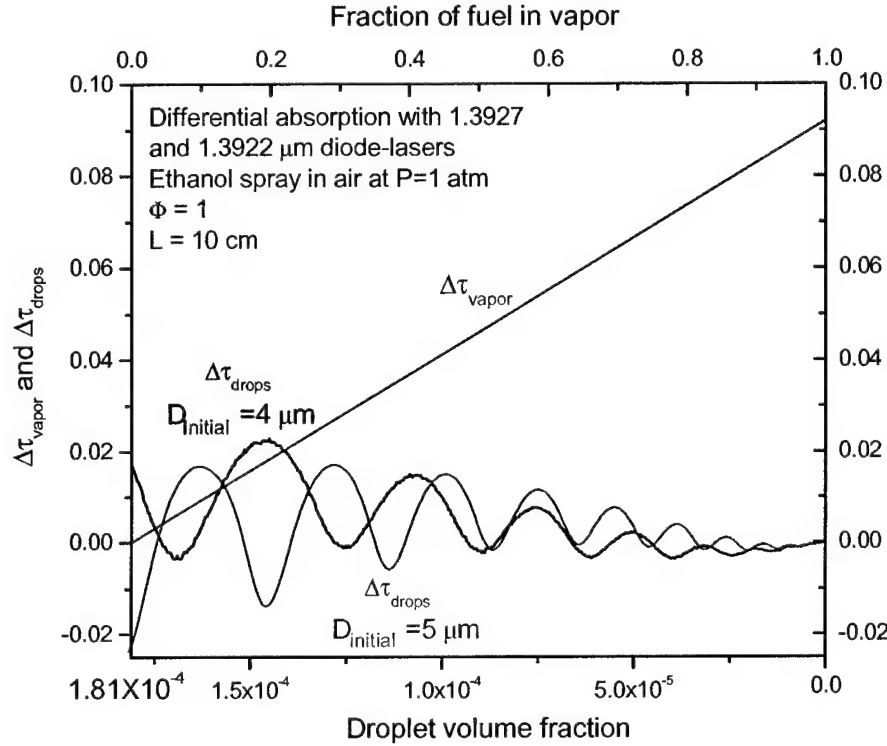


Fig. 2.6.3 Measured absorption spectrum of ethanol vapor near 1.39  $\mu\text{m}$  showing the optimized wavelengths for differential absorption.

Here we calculated the differential vapor absorption and droplet extinction signal for a mono-disperse ethanol droplet cloud, assuming uniform evaporation. Fig. 2.6.4 defines the differential droplet extinction as the difference of extinction between the two wavelengths applied, so this quantity can be positive or negative. When compared with differential vapor absorption, the absolute magnitude should be used. For an equivalence ratio of 1.0, the droplet extinction exceeds the vapor absorption over most of the droplet volume fraction range at either wavelength. But, as shown in Fig. 2.6.4, the differential vapor absorption signal ( $\Delta\tau_{\text{vapor}}$ ) starts to exceed the absolute magnitude of the droplet signal ( $\Delta\tau_{\text{drops}}$ ) after about 22% and 13% of the fuel evaporates for an initial droplet size of 4 and 5  $\mu\text{m}$ , respectively. Clearly the differential absorption technique considerably improves the vapor detection accuracy and extends the vapor sensing capability to a much wider domain.

#### **Droplet Size Distribution Measurements**

Recent work has extended the multiplexed laser extinction technique to determine droplet size distribution because, under some cases, a measurement of  $D_{32}$  is not enough to characterize the spray.



**Fig. 2.6.4** Comparison of differential vapor absorption and droplet extinction in ethanol sprays using the differential absorption technique for two different initial droplet sizes.

The transmission of monochromatic light with wavelength  $\lambda$  by a collection of polydisperse droplets is given by:

$$\ln T(\lambda) = -\frac{\pi L N}{4} \int_0^{\infty} Q(D, \lambda) f(D) D^2 dD \quad (2.6.4)$$

where  $f(D)$  is a normalized distribution function and  $N$  is droplet number density. To perform a droplet size distribution measurement before the droplet number density is known, the transmission must be measured at multiple wavelengths. For example, if transmission information is provided at two wavelengths,  $\lambda_1$  and  $\lambda_2$ , then the ratio of the transmission at these two wavelengths will be given by:

$$\frac{\ln T(\lambda_1)}{\ln T(\lambda_2)} = \frac{\int_0^{\infty} Q(D, \lambda_1) f(D) D^2 dD}{\int_0^{\infty} Q(D, \lambda_2) f(D) D^2 dD} \quad (2.6.5)$$

Thus, in equation (2.6.5) the ratio is independent of the number density. The left-hand side may be measured directly, and, since the extinction coefficient is a known function, the right-hand side is a function only of the droplet size distribution. We have developed a methodology to select optimized wavelengths to measure the droplet size distribution based on equation (2.6.5). For the droplet size range encountered in our aerosol shock tube facility (droplet diameter below 8  $\mu\text{m}$ ), the transmission measured at 10, 3.34, and

2 $\mu$ m provides valuable information about the droplet size distribution. Fig. 2.6.5 shows ratios of  $\ln T(\lambda)$  calculated from equation (2.6.5) assuming a two-parameter log-normal distribution defined by equation (2.6.6) of the droplets among these three wavelengths.

$$f(D) = \frac{1}{\sqrt{2\pi D \ln(K)}} \exp\left[-\frac{1}{2}(\ln D - \ln D_{32})^2\right] \quad (2.6.6)$$

In equation (2.6.6),  $K$  is the distribution width and  $D_{32}$  is the Sauter mean diameter for the distribution. A  $K$  of 1.1 corresponds to a very narrow size distribution and a  $K$  of 1.5 represents a very wide one.

Fig. 2.6.5 indicates that the transmission ratio between 10 and 3.4  $\mu$ m is insensitive to the distribution width; therefore, a combination of 10 and 3.4  $\mu$ m could provide a reasonably accurate  $D_{32}$  without the knowledge of the distribution width. On the other hand, the transmission ratio between 3.4 and 2  $\mu$ m is sensitive to the distribution width; therefore, this ratio provides a good measurement of the distribution width once  $D_{32}$  is determined by 10 and 3.4  $\mu$ m laser extinction. With three wavelengths, we have two independent ratios with which to make this measurement. In reality, we assume the parameters of the size distribution and find the distribution parameters that best fit our transmission data. Then we can return to equation (4) to determine  $N$ , and consequently the liquid volume fraction occupied by the liquid particles.

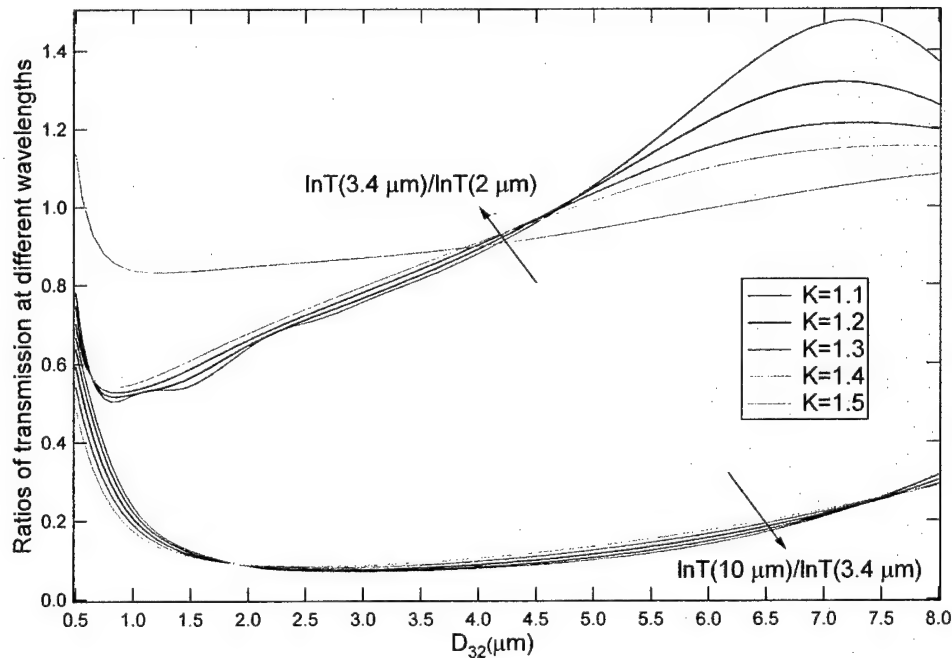
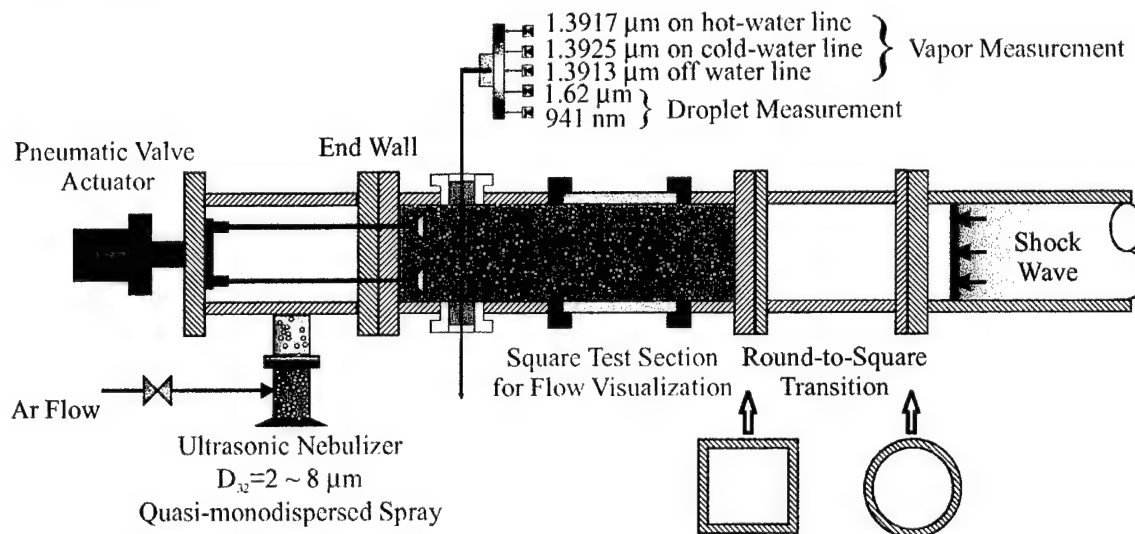


Fig. 2.6.5 Ratios of transmission at different wavelengths for a log-normal droplet size distribution with five widths.

### Experimental Facility

A unique shock tube facility has been developed to test and develop laser-based diagnostics for multi-phase flows and to apply laser-based diagnostics to study multi-phase combustion [Ref. 2.6.4]. Fig. 2.6.6 depicts our aerosol shock tube facility equipped

with laser diagnostics. Shock waves are generated by bursting lexan diaphragms with pressurized helium in a standard shock tube driver section. An ultrasonic nebulizer provides spray loading to the test gas near the end wall. The shock waves propagate into the square test section and interact with the spray, where line-of-sight laser diagnostics are deployed for time-resolved monitoring of the interactions between shock waves and liquid sprays.



**Fig. 2.6.6** Aerosol shock tube experimental facility with optical diagnostics

### Preliminary Results

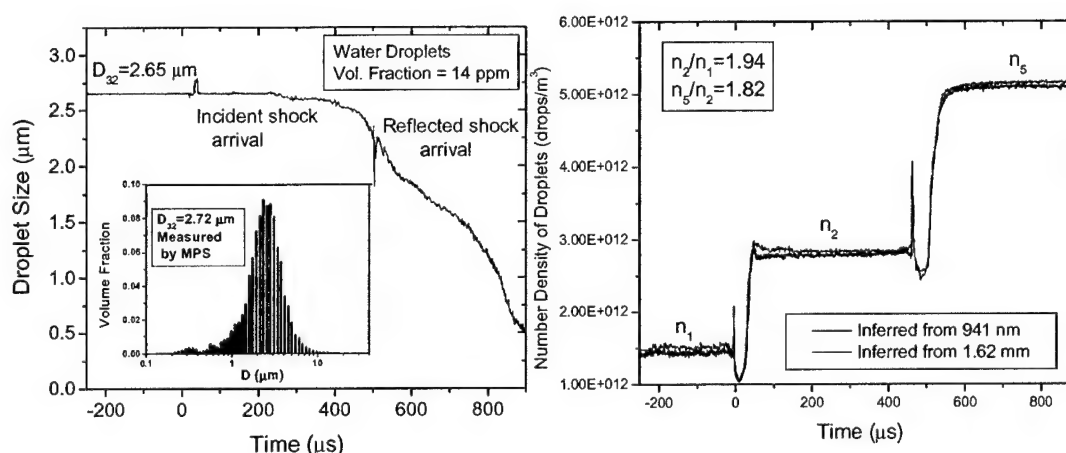
To demonstrate the feasibility and utility of the diagnostic technique, a series of experiments have been performed in the aerosol shock tube facility. In our initial experiments, we applied the laser diagnostic to study the interactions between water droplets and shock waves.

Fig. 2.6.6 provides a schematic of the experimental setup. Laser extinction was measured at five wavelengths. Two diode lasers, which emit at wavelengths of 941 nm and 1.62  $\mu\text{m}$ , are non-resonant with any water vapor absorption line and were used to characterize the mean droplet size ( $D_{32}$ ) and the droplet volume fraction based on the measurement concepts described in section 2.6.1. A water vapor concentration and temperature measurement cycle consists of three consecutive and repeatable shock wave experiments for which a third diode laser is tuned to three different wavelengths, respectively: 1.3917  $\mu\text{m}$  (the absorption center of a “hot” water vapor line whose absorption strength increases with increasing temperature), 1.3925  $\mu\text{m}$  (the absorption center of a “cold” water vapor line whose absorption strength decreases with increasing temperature), and 1.3913  $\mu\text{m}$  (away from any water vapor line). The third off-line wavelength is used to track the extinction caused by droplets for the first two on-line wavelengths. Then, when combined with an independent pressure measurement, water vapor concentration and temperature information can be extracted from those on-line wavelengths.

Fig. 2.6.7 presents the results of droplet measurements in a typical shock wave measurement cycle, and Fig. 2.6.8 presents the corresponding vapor measurements. For

these measurements, the Mach number for the incident shock is  $M_s=1.50$  and  $P_1=0.355$  atm. Incident and reflected shock conditions calculated using only the vapor component were:  $T_2=472$  K,  $T_5=683$  K,  $P_2=0.587$  atm,  $P_5=1.421$  atm,  $\rho_{21}=1.72$ ,  $\rho_{52}=1.63$ .

From the mean droplet diameter measurements in Fig. 2.6.7, we see that the pre-shock droplet size measured by multiplexed laser extinction is in good agreement with Malvern Particle Sizer measurements. This measurement also captures the droplet size history during rapid evaporation brought about by shock heating. The droplet number density measurement in Fig. 2.6.7 shows reasonable agreement with shock wave calculations. Note that once droplet size is determined, the extinction from each of the wavelengths, 941 nm and 1.62  $\mu\text{m}$ , can yield droplet number density information, as shown in the number density measurements in Fig. 2.6.7. The droplet number density measurements inferred from 941 nm and 1.62  $\mu\text{m}$  are in good agreement.



**Fig. 2.6.7** Mean droplet size and droplet number density measurements as a function of time after shock wave passage using wavelength-multiplexed laser extinction diagnostics.

Fig. 2.6.8 shows the corresponding vapor measurements. From the vapor temperature measurements, we can see that vapor temperatures immediately behind the shock passages approximate those from shock calculations. However, during evaporation in the shock-heated gas, the bulk gas temperature decreases, as expected, and the vapor partial pressure increases, as shown in the right figure in Fig. 2.6.8. These results increase our confidence in the measurement strategy.

We have developed a diagnostic technique based on wavelength-multiplexed laser extinction for multiphase flows. In experiments using a new shock tube, we demonstrated that this technique is suitable for simultaneous measurements of droplet size, droplet volume fraction, vapor temperature, and vapor concentration with fast time response. Such a diagnostic should provide a powerful tool to advance many aspects of heterogeneous combustion, including spray evaporation, droplet combustion, detonation of sprays, and combustion quenching.



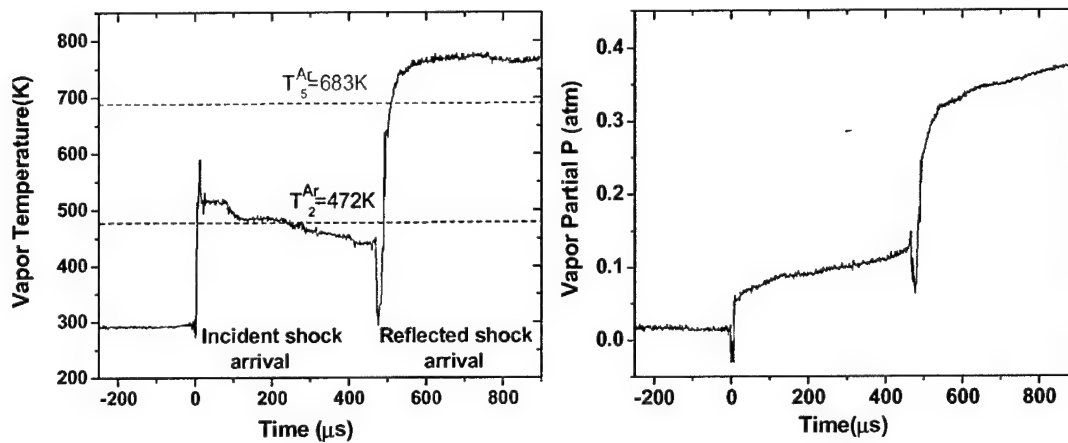


Fig. 2.6.8 Water vapor temperature and partial pressure measurements as a function of time after shock wave passage using multiplexed laser extinction diagnostics.

### **References for section 2.6**

- 2.6.1. Tishkoff, J.M., Hammond, D.C., and Chraplyvy, A.R. "Diagnostic Measurements of Fuel Spray Dispersion", *Journal of Fluid Engineering*, **104**, 313-317 (1982).
- 2.6.2. Dobbins, R.A. and Jizmagian, G.S., "Optical Scattering Cross Sections for Polydispersions of Dielectric Spheres", *Journal of the Optical Society of America*, **56**, 1345-1350 (1966).
- 2.6.3. Ma, L., Jeffries, J.B. and Hanson, R.K., "Two-phase Fuel Diagnostic Based on Diode-lasers", *AIAA 2003- 0401* (2003).
- 2.6.4. Kashdan, J.T., Hanson, T.C., Piper, E.L., Davidson, D.F. and Hanson, R.K., "A New Facility for The Study of Shock Wave-induced Combustion of Liquid Fuels", *AIAA 2004- 0468* (2004).

## 2.7 *2f Spectroscopy for Temperature Measurements in Combustion Flows*

### **Background**

Wavelength modulation, in conjunction with second-harmonic ( $2f$ ) detection, is well-known as a means to increase signal to noise ratios (SNR). Our AFOSR-sponsored research has shown that  $2f$  methods may provide additional benefits for real-time measurements of propulsion parameters, such as temperature. For temperature measurements with spectrally-isolated lines, taking  $2f$  peak ratios of absorption features and making a judicious choice of modulation indices simplifies signal interpretation and reduces the need for calibration over large temperature ranges. Also,  $2f$  strategies effectively can eliminate one of the largest sources of uncertainty and error in scanned direct-absorption measurements, i.e. baseline fitting. Baseline fitting is especially problematic in the case of weak absorption features, for which it is difficult to determine where a zero-absorption baseline begins and ends. Similarly, at elevated pressures, absorption features often combine and broaden to such an extent that the determination of a laser intensity zero-absorption baseline is not possible, especially when transmission fluctuations occur due to beam steering from thermal gradients or mechanical vibrations. In addition, small changes in the fitted baseline can alter the apparent line strength and shape of a feature significantly.  $2f$  line shapes improve SNR, as well as reduce the sensitivity to baseline fitting errors, since they are sensitive to line shape curvature ( $2^{\text{nd}}$  derivative), making them advantageous in dealing with noisy signals and weak absorption features.

In our exploratory work on this new measurement concept, multiplexed fiber-coupled diode lasers are used to probe second-harmonic line shapes of two near-infrared water absorption features, at 1343 nm and 1392 nm, in order to infer temperatures in gases containing water vapor, such as combustion flows. Wavelength modulation is performed at 170 kHz, and is superimposed on 1 kHz wavelength scans in order to recover full second-harmonic line shapes. Digital waveform generation and lock-in detection is performed using a data acquisition card installed on a PC. An optimal selection of the modulation indices is shown to simplify data interpretation over extended temperature ranges and to minimize the need for calibration when performing  $2f$  ratio thermometry.

### **Theory**

Assuming that a sinusoidal modulation is riding on a constant D.C. diode laser injection current (or a slowly varying ramp, in relation to the sinusoidal modulation frequency), the instantaneous laser frequency,  $\nu(t)$ , and output intensity,  $I_0(t)$ , may, respectively, be expressed as:

$$\nu(t) = \bar{\nu} + a \cdot \cos(\omega_m t) \quad (2.7.1)$$

$$I_0(t) = \bar{I}_0 + i_0 \cdot \cos(\omega_m t + \psi) \quad (2.7.2)$$

The modulation frequency is given by  $\omega_m$ ,  $\psi$  is the phase shift between the intensity modulation and the wavelength modulation, while  $a$  and  $i_0$  are the amplitudes of

modulation around  $\bar{\nu}$  and  $\bar{I}_0$ , which are the slowly varying values of the average wavelength and injection current. The laser intensity and wavelength are assumed to vary linearly with injection current in this analysis, which is an appropriate assumption for the hardware and modulation parameters employed here.

The Beer-Lambert relation gives the transmitted intensity,  $I_t$ , of monochromatic radiation after passing through an absorbing gas, here given for a uniform gas medium:

$$\tau(\nu) = \left( \frac{I_t}{I_0} \right)_\nu = e^{-\alpha(\nu)L} \quad (2.7.3)$$

$\tau(\nu)$  is the transmission coefficient,  $I_0$  is the incident radiation intensity,  $\alpha(\nu)$  is the absorption coefficient and  $L$  is the optical absorbing path length. The absorption coefficient is the product of line strength,  $S$  [ $\text{cm}^{-2}/\text{atm}$ ], absorbing species partial pressure,  $p_i$  [atm], and line shape function  $\phi(\nu)$  [cm]:  $\alpha(\nu) = S\phi(\nu)p_i$ .

The transmission coefficient,  $\tau(\nu) = \tau(\bar{\nu} + a \cdot \cos(\omega_m t))$ , is a periodic even function in  $\omega_m t$  and can be expanded in a Fourier cosine series,

$$\tau(\bar{\nu} + a \cdot \cos(\omega_m t)) = \sum_{k=0}^{\infty} H_k(\bar{\nu}, a) \cos(k\omega_m t) \quad (2.7.4)$$

where the functions  $H_k(\bar{\nu})$  are given as

$$H_0(\bar{\nu}, a) = \frac{1}{2\pi} \int_{-\pi}^{+\pi} \tau(\bar{\nu} + a \cdot \cos\theta) d\theta \quad (2.7.5)$$

$$H_k(\bar{\nu}, a) = \frac{1}{\pi} \int_{-\pi}^{+\pi} \tau(\bar{\nu} + a \cdot \cos\theta) \cdot \cos k\theta \cdot d\theta \quad (2.7.6)$$

For  $2f$  detection, a lock-in amplifier is used to isolate the second harmonic signal. The remaining signal, which contains the second harmonic component of the Fourier sum in Eqn. 2.7.4, is given by the relation

$$S_2(\bar{\nu}) = \frac{i_0}{2} H_3(\bar{\nu}, a) + \bar{I}_0 H_2(\bar{\nu}, a) + \frac{i_0}{2} H_1(\bar{\nu}, a) \quad (2.7.7)$$

Here we assume that the phase shift between the laser intensity modulation and the optical frequency modulation is negligible. In addition, we have ignored the effects of nonlinearities in the modulation, which create harmonic distortions that are manifested as a background  $2f$  signal.

For optically-thin samples,  $\alpha(\nu) \cdot L \ll 1$  (or less than about 0.10), the transmission coefficient reduces to

$$\tau = \exp(-\alpha \cdot L) \approx 1 - \alpha \cdot L = 1 - S \cdot \phi \cdot p_i \cdot L \quad (2.7.8)$$

and the second harmonic Fourier component simplifies as:

$$H_2(\bar{\nu}, a) = -\frac{S \cdot p_i \cdot L}{\pi} \int_{-\pi}^{+\pi} \phi(\bar{\nu} + a \cdot \cos\theta) \cos 2\theta \cdot d\theta \quad (2.7.9)$$

Therefore, the  $2f$  peak height is only complicated by the line shape function,  $\phi$ . To infer gas temperature unambiguously from a ratio of  $2f$  peak heights, it is desired that the ratio should only depend upon the well-known line strengths,  $S$ , of the selected absorption features. This simplification is possible if the integral in Eqn. 2.7.9 is either constant or varies similarly with respect to temperature for each absorption feature, since  $p_i$  and  $L$  cancel in the ratios. This optimization requires care in choosing the modulation index,  $m$ , which is defined as

$$m = \frac{a}{\Delta\nu} \quad (2.7.10)$$

where  $\Delta\nu$  is the half width at half maximum (HWHM) of the absorption line. Fig. 2.7.1 illustrates how the line-center  $2f$  peak height varies as a function of  $m$  for Gaussian (Doppler broadened) and Lorentzian (pressure-broadened) line shapes. The functionality is due entirely to the integral in Eqn. 2.7.9. The peak value occurs at  $m \sim 2.2$  for all line shapes.

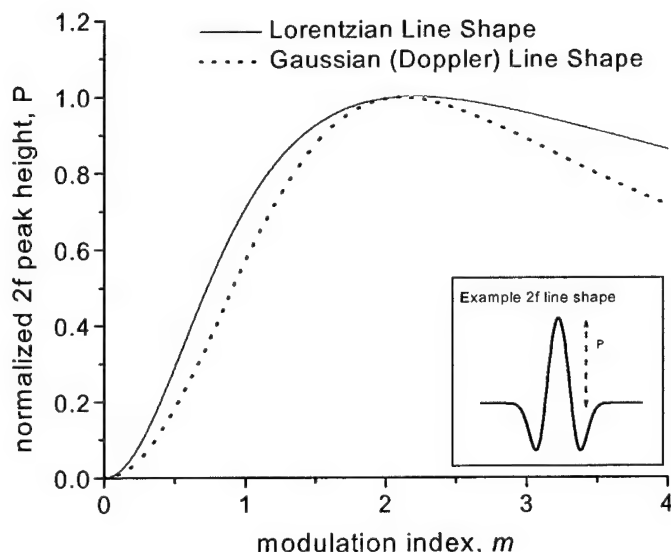


**Fig. 2.7.1** Normalized  $2f$  peak height versus  $m$  for a Lorentzian and Gaussian line shape

Temperature measurements using  $2f$  spectroscopy are influenced by the fact that the modulation index,  $m$ , varies with temperature through  $\Delta\nu$  in Eqn. 2.7.10. Doppler (Gaussian) line widths vary with the square root of  $T$ , whereas collisional (Lorentzian) widths vary with  $T$  according to an inverse power law:

$$\Delta\nu_D = 3.581 \times 10^{-7} \nu_0 \sqrt{T/M} \quad (2.7.11)$$

$$\Delta\nu_L = P \sum_j \chi_j \gamma_j^{T_0} \left( \frac{T_0}{T} \right)^{n_j} \quad (2.7.12)$$

In Eqn. 2.7.11 and Eqn. 2.7.12,  $\Delta\nu_D$  and  $\Delta\nu_L$  are the Doppler and Lorentzian half widths at half maximum (HWHM), respectively, in wavenumber ( $\text{cm}^{-1}$ ) units.  $\nu_0$  is the line-

center position of the feature in  $\text{cm}^{-1}$ ,  $T$  is the temperature in Kelvin, and  $M$  is the atomic mass (a.m.u.).  $P$  is the total pressure in atmospheres,  $\chi_j$  is the mole fraction of the  $j^{\text{th}}$  component of the gas mixture,  $\gamma_j^{T_0}$  is the pressure broadening coefficient (half width) at reference temperature  $T_0$  for the  $j^{\text{th}}$  perturbing species ( $\text{cm}^{-1}/\text{atm}$ ), and  $n_j$  is the species-dependent temperature coefficient.

For Doppler-broadened line shapes, the line shape function,  $\phi$ , only varies with temperature and is nearly identical for all absorption features probed by a multiplexed beam (assuming similar values of  $\nu_0$ ). Therefore, choosing identical modulation indices,  $m$ , for each absorption feature insures that the integral in Eqn. 2.7.9 cancels when taking  $2f$  peak ratios. For pressure-broadened lines, the Lorentzian line shape function may have a slightly different temperature and pressure dependence for each absorption line due to differing broadening parameters,  $\gamma_j^{T_0}$  and  $n_j$ . Also, spectral line widths are dependent upon gas composition, since broadening parameters are species-specific. However, by choosing identical values of  $m$  for each absorption feature near the conditions ( $P$ ,  $T$ ,  $\chi_j$ ) of interest, the  $2f$  peak ratios of pressure-broadened lines should be relatively insensitive to differences in the integral in Eqn. 2.7.9 for modest temperature, pressure, and compositional ranges. These effects may be analyzed and simulated by using parameters found in spectral databases such as HITRAN and HITEMP. The most ideal situation, clearly, is to tune the modulation amplitude such that  $m$  is near a value of 2.2 so that the integral in Eqn. 2.7.9 is maximized and, therefore, insensitive to temperature, pressure, and compositional effects for *each* individual absorption feature.

### **Validation Experiments**

Validations of this  $2f$  thermometry strategy were carried out in a heated optical cell. The absorption cell was filled with various amounts of pure water vapor ranging from 1.5 Torr to 2.5 Torr, all of which resulted in peak absorbance levels of less than 10% (satisfying equation 8). Three modulation amplitudes were used at each condition near the maximum modulation index:  $m \sim 2.2$ . Second harmonic peak ratios, at the measurement conditions stated above, are plotted for the 1392 nm and 1343 nm features in Fig. 2.7.2. Line strengths and lower state energies from the HITRAN/HITEMP database are used to calculate line strength ratios, which also are normalized and plotted in the same figures. Considering the effects of temperature uncertainty and nonuniformity in the cell ( $\sim 25\text{K}$ ), the data matches the simulated  $2f$  ratios (based on line strength ratio) well. The agreement between  $2f$  peak ratios and line strength behavior as a function of temperature demonstrates the simplifying effect of optimizing modulation depths.

The data in Fig. 2.7.2 can be presented in an alternative form to demonstrate the effectiveness of the sensor to infer temperature. In Fig. 2.7.3, the data point at 825 K, with  $m \sim 2.2$ , is used to calibrate the  $2f$  sensor. Temperatures at four hotter conditions are extrapolated by using the calibration point and the HITRAN-simulated temperature dependence of the line strength ratios. The agreement of the  $2f$  sensor measurements with the thermocouple measurements is within the uncertainty and nonuniformity of the thermocouple and furnace ( $\pm 25\text{ K}$ ).

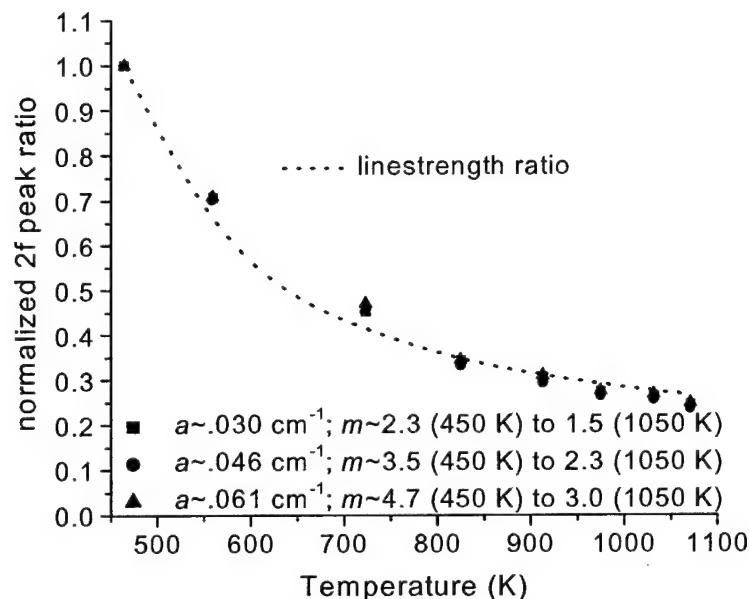


Fig. 2.7.2 Normalized 2f peak height versus  $m$  for a Lorentzian and Gaussian line shape

These scanned-2f measurements are performed with a modulation frequency of 170 kHz and a scan rate (measurement bandwidth) of 1 kHz. In cases where a fixed-wavelength 2f strategy is preferred, measurement bandwidths are determined by the lock-in filter time constant, which may be as high as 50 kHz if a 170 kHz modulation frequency is employed.

Although our validation studies are performed using two water transitions at 1392 nm and 1343 nm, the optimum selection of absorption lines depends on the particular measurement conditions anticipated. For example, high temperature measurements require the use of absorption transitions with larger lower state energies,  $E''$ . High pressure measurements may benefit from the selection of lines with smaller broadening parameters, in order to maximize 2f signal levels. Care must be taken to tailor the selection of absorption line candidates for the specific diagnostic environment of interest.

### Summary and Future Work

2f spectroscopy has been shown to offer several benefits over conventional direct absorption methods for making temperature measurements in gaseous systems relevant to propulsion. This method exhibits improvements to SNR, as well as reduced sensitivity to baseline-fitting errors. 2f peak height ratios, using optimized modulation depths, enable straightforward data interpretation, as the 2f peak height ratios are proportional to line strength ratios. The need for calibration is reduced when optimized modulation depths are employed, and the measurement range is increased.

The 2f ratio thermometry strategy recently has been extended to allow for measurements in environments with broadened and blended spectra, such as occur at high pressures [2.7.2]. 2f simulations, based upon the HITRAN spectral database and laboratory validations, allow for the interpretation of 2f peak heights in order to obtain temperature and species concentration information. The 2f signal depends critically on the modulation depth of the laser,  $a$ , which has been increased to values above those

typically achieved when performing wavelength modulation spectroscopy with diode lasers. The  $2f$  method, with large modulation depths, has been validated by using near-infrared diode lasers to probe pressure-broadened water vapor features in the 1.4 micron region over a range of temperatures from 296 to 800 K and at pressures up to 20 atm. Modulation depths as high as  $a = 0.8 \text{ cm}^{-1}$  have been attained at modulation frequencies of 50 kHz and measurement bandwidths of 15 kHz. Comparisons of experimental results with  $2f$  simulations based on the HITRAN spectral database provide confirmation of the capability of this method for rapid measurements of gas temperature and species concentration.

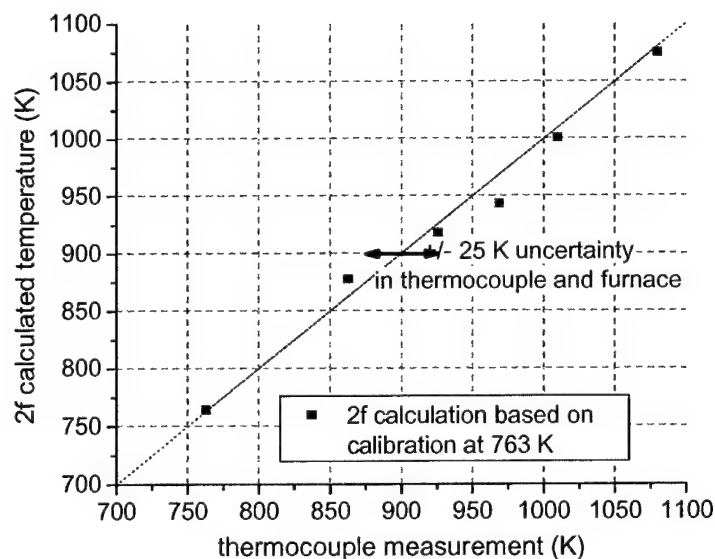


**Fig. 2.7.3** Calibrated  $2f$  temperature measurements versus thermocouple measurements (using 1392 nm / 1343 nm  $2f$  peak ratios). Ambient water vapor,  $P = 1 \text{ atm}$ ,  $m \sim 2.2$

Ongoing research is being conducted to demonstrate the  $2f$  ratio thermometry strategy in real combustion test facilities, such as a SCRAMJET engine, as well as to extend and optimize the diagnostic at elevated pressures, as may be encountered in advanced gas turbine combustors. Finally, we wish to explore the potential of  $2f$  absorption strategies for sensing fuels with highly broadened and congested spectra.

### **References for section 2.7**

- 2.7.1. Liu, J.T.C., Jeffries, J.B., and Hanson, R.K. "Wavelength Modulation Absorption Spectroscopy with  $2f$  Detection using Multiplexed Diode Lasers for Rapid Temperature Measurements in Gaseous Flows," *App. Phys. B* **78**, 503-511 (2004).
- 2.7.2. Liu, J.T.C., Jeffries, J.B. and Hanson, R.K., "Large-Modulation-Depth  $2f$  Spectroscopy with Diode Lasers for Rapid Temperature and Species Measurements in Gases with Blended and Broadened Spectra," *Applied Optics*, submitted, April, 2004.

### 3.0 Publications and Presentations

#### AFOSR SPONSORED PUBLICATIONS 2001-2003

##### REVIEWED PUBLICATIONS 2001

1. A. Ben-Yakar and R.K. Hanson, "Cavity Flame-Holders for Ignition and Flame Stabilization in Scramjets: An Overview," *J. Prop. and Power* **17**, 869-877 (2001).
2. J. Wang, S. T. Sanders, J. B. Jeffries, and R. K. Hanson, "Oxygen Measurements at High Pressures Using Vertical Cavity Surface-Emitting Lasers, *Appl. Phys. B*, **72**, 865-872 (2001).
3. S. T. Sanders, J. Wang, J. B. Jeffries, and R. K. Hanson, "VCSEL Absorption Sensor for Line-of-Sight Gas Temperature Distributions," *Applied Optics* **20**, 4404-4415 (2001).
4. S.T. Sanders, D.W. Mattison, J.B. Jeffries, and R.K. Hanson, "Rapid Temperature-Tuning of a 1.4  $\mu\text{m}$  Diode Laser with Application to High-Pressure  $\text{H}_2\text{O}$  Absorption Spectroscopy," *Optics Letters* **26**, 1568-1570 (2001).
5. B. J. Kirby, R. K. Hanson, "CO 2 Imaging with Saturated Planar Laser-Induced Vibrational Fluorescence," *Applied Optics*, **40**, 6136-6144 (2001).
6. J.T.C. Liu, R.K. Hanson and J.B. Jeffries, "High-Sensitivity Absorption Diagnostic for  $\text{NO}_2$  using a Blue Diode Laser," *J. Quant. Spectrosc. and Radiat. Transfer* **72**, 655-664 (2001).

##### REVIEWED PUBLICATIONS 2002

7. A. Ben-Yakar and R.K. Hanson, "Ultra-fast-framing Schlieren System for Studies of the Time Evolution of Jets in Supersonic Crossflows," *Experiments in Fluids* **32**, 652-666 (2002).
8. A. Ben-Yakar and R.K. Hanson, "Characterization of Expansion Tube Flows for Hypervelocity Combustion Studies in the Flight Mach 8-13 Engine," *J. Prop. and Power* **18**, 943-952 (2002).
9. J.T.C. Liu, R.K. Hanson, and J.B. Jeffries, "High-Sensitivity Absorption Diagnostic for  $\text{NO}_2$  using a Blue Diode Laser," *J. Quant. Spectros. Rad. Trans.* **72**, 655-664 (2002).
10. B.J. Kirby and R.K. Hanson, "Linear Excitation Schemes for IR PLIF Imaging of CO and  $\text{CO}_2$ ," *Applied Optics* **41**, 1190-1201 (2002).



11. W. Bessler, C. Schulz, T. Lee, J. B. Jeffries, and Ronald K. Hanson, "Strategies for laser-induced fluorescence detection of nitric oxide in high-pressure flames: I. A-X (0,0) excitation," *Applied Optics*, **41**, 3547-3557 (2002).
12. C. Schulz, J.D.Koch, D.F. Davidson, J.B.Jeffries, and R.K. Hanson, "Ultraviolet Absorption Spectra of Shock-Heated Carbon Dioxide and Water between 900 and 3050 K," *Chemical Physics Letters*, **355**, 82-88 (2002).
13. W.G. Bessler, C. Schulz, T. Lee, D.-I. Shin, M. Hofmann, J.B. Jeffries, J. Wolfrum, and R.K. Hanson, "Quantitative NO-LIF Imaging in High-pressure Flames," *Applied Physics B*, **75**, 97-102 (2002).
14. S. T. Sanders, D.W. Mattison, L. Ma, J.B. Jeffries, and R.K. Hanson, "Wavelength-Agile Diode-Laser Sensing Strategies for Monitoring Gas Properties in Optically Harsh Flows: Application in Cesium-Seeded Pulse Detonation Engine," *Optics Express*, **10**, 505-514 (2002).
15. T. Rossmann, M.G. Mungal, and R.K. Hanson, "Evolution and Growth of Large Scale Structures in High Compressibility Mixing Layers," *J. of Turbulence*, **3**, 1-18 (2002).
16. S.T. Sanders, D.W. Mattison, J.B. Jeffries, and R.K. Hanson, "Sensors for High-Pressure, Harsh Combustion Environments Using Wavelength-Agile Diode Lasers," 29<sup>th</sup> Int. Symp. on Combustion, Sapporo, Japan, July 2002; *Proc. of the Comb. Inst.* **29**, 2661-2667 (2002).
17. C. Schulz, J.B. Jeffries, J.D. Koch, D.F. Davidson, J. Wolfrum, and R.K. Hanson, "Impact of UV Absorption by CO<sub>2</sub> and H<sub>2</sub>O on NO LIF in High Pressure Combustion," 29<sup>th</sup> Int. Symp. on Combustion, Sapporo, Japan, July 2002; *Proc. of the Comb. Inst.* **29**, 2735-2742 (2002).
18. L. Ma, S.T. Sanders, J.B. Jeffries, and R.K. Hanson, "Monitoring and Control of a Pulse Detonation Engine using a Diode-Laser Fuel Concentration and Temperature Sensor," 29<sup>th</sup> Int. Symp. on Combustion, Sapporo, Japan, July 2002; *Proc. of the Comb. Inst.* **29**, 161-166 (2002).
19. T. Rossmann, M.G. Mungal, and R.K. Hanson, "Evolution and Growth of Large Scale Structures in High Compressibility Mixing Layers," *J. of Turbulence*, vol 3, No. 9, 1-18 (2002).

#### **REVIEWED PUBLICATIONS 2003**

20. A. Ben-Yakar and R. K. Hanson, "Ultra-fast-framing Schlieren System for Studies of the Time Evolution of Jets in Supersonic Crossflows," *Experiments in Fluids*, **32**, 652-666 (2003).

21. T. Rossmann, M.G. Mungal, and R.K. Hanson, "Nitric –oxide Planar Laser-induced Fluorescence applied to Low-pressure Hypersonic Flow Fields for the Imaging of Mixture Fraction," *App. Optics* **42**, 6682-6695 (2003).
22. W.G. Bessler, C. Schulz, T. Lee, J.B. Jeffries, and R.K. Hanson, "Strategies for Laser-Induced Fluorescence Detection of Nitric Oxide in High-Pressure Flames: II. A-X (0,1) Excitation," *Applied Optics*, **42**, 2031-2042 (2003).
23. D.W. Mattison, C.M. Brophy, S.T. Sanders, L. Ma, L., K.M. Hinckley, J.B. Jeffries, and R.K. Hanson, "Pulse detonation engine characterization and control using tunable diode-laser sensors," *Journal of Propulsion and Power*, **19**, 568-572 (2003).
24. S.T. Sanders, D.W. Mattison, J.B. Jeffries, and R.K. Hanson, "Time-of-flight Diode-laser Velocimetry using a Locally-seeded Atomic Absorber: Application in a Pulse Detonation Engine," *Shock Waves* **12**, 435-441 (2003).
25. J.D. Koch and R.K. Hanson, "Temperature and Excitation Wavelength Dependences of 3-Pentanone Absorption and Fluorescence for PLIF Applications," *App. Phys. B*, **76**, 319-324 (2003).
26. W.G. Bessler, C. Schulz, T. Lee, J.B. Jeffries, and R.K. Hanson, "Strategies for Laser-Induced Fluorescence Detection of Nitric Oxide in High-Pressure Flames: III. Comparison of A-X Detection Schemes," *Applied Optics*, **42**, 4922-4936 (2003).
27. W.G. Bessler, C. Schulz, T. Lee, J.B. Jeffries, and R.K. Hanson, "Carbon dioxide UV laser-induced fluorescence in high-pressure flames," *Chemical Physics Letters*, **375**, 344-349 (2003).

#### **REVIEWED PUBLICATIONS 2004**

28. J.T.C. Liu, J.B. Jeffries, and R.K. Hanson, "Wavelength Modulation Absorption Spectroscopy with 2f Detection using Multiplexed Diode Lasers for Rapid Temperature Measurements in Gaseous Flows," *App. Phys. B* **78**, 503-511 (2004).
29. J.B. Jeffries, C. Schulz, D.W. Mattison, M.A. Oelschlaeger, W.G. Bessler, T. Lee, D.F. Davidson, and R.K. Hanson, "UV Absorption of CO<sub>2</sub> for Temperature Diagnostics of Hydrocarbon Combustion Applications," *Proc. Combustion Institute*, **30**, (2004) in press.
30. W. Koban, J. Koch, V. Sick, N. Wermuth, R.K. Hanson, and C. Schulz, "Predicting LIF Signal Strength for Toluene and 3-Pentanone under Transient Temperature and Pressure Conditions," *Proc. Combustion Institute*, **30**, (2004) in press.
31. D.W. Mattison, M.A. Oehlschlaeger, C.I. Morris, Z.C. Owens, E.A. Barbour, J.B. Jeffries, and R.K. Hanson, "Evaluation of Pulse Detonation Engine Modeling using Laser-Based Temperature and OH Concentration Measurements," *Proc. Combustion Institute*, **30**, (2004) in press.

32. H. Li, R.K. Hanson, and J.B. Jeffries, "Diode Laser Induced Infrared Fluorescence of Water Vapor," *J. Measurement Science*, (2004) in press.
33. J. Koch, R.K. Hanson, W. Koban, C. Schulz, "Rayleigh-Calibrated Fluorescence Quantum Yield Measurements of Acetone and 3-pentanone," *App. Optics*, (2004) in press.
34. W. Koban, J. Koch, R.K. Hanson, C. Schulz, "Absorption and Fluorescence of Toluene at Elevated Temperatures." *Physical Chemistry Chemical Physics*, (2004) in press.
35. A. Ben-Yakar, M.G. Mungal, and R.K. Hanson, "Time Evolution of Coherent Structures and Mixing Characteristics of Hydrogen and Ethylene Jets in Supersonic Crossflow," *Physics of Fluids*, (2004) in press.
36. A. Ben-Yakar, M.G. Mungal, and R.K. Hanson, "The Effect of Velocity and Density Ratios on Transverse Jets in Supersonic Crossflows," *Physics of Fluids*, (2004) in press.
37. T. Rossmann, M.G. Mungal, and R.K. Hanson, "Mixing Efficiency Measurements using a Modified Cold-Chemistry Technique," *Experiments in Fluids*, (2004) submitted.
38. J.T.C. Liu, J.B. Jeffries and R.K. Hanson, "Large-Modulation-Depth 2f Spectroscopy with Diode Lasers for Rapid Temperature and Species Measurements in Gases with Blended and Broadened Spectra," *App. Optics*, (2004) submitted.

#### **BOOKS EDITED**

*Applied Combustion Diagnostics*, ed Katharina Kohse-Hoeinghaus and Jay B. Jeffries, Taylor and Francis (2002) 705 pages.

#### **BOOK CHAPTERS**

39. D.F. Davidson and R.K. Hanson, "Spectroscopic Diagnostics," in Handbook of Shock Waves, Vol. 1, Chapter 5.2, Academic Press, eds.G. Ben-Dor, O. Igra and T. Elperin, 2001.
40. A. McIlroy and J. B. Jeffries, "Cavity Ring-Down Spectroscopy for Concentration Measurements," in *Applied Combustion Diagnostics*, ed. K. Kohse-Hoeinghaus and J. B. Jeffries, Francis and Taylor, New York, (2002), pp. 98-127.
41. M.G. Allen, E.R. Furlong, and R.K. Hanson, "Tunable Diode Laser Sensing and Combustion Control," in *Applied Combustion Diagnostics*, ed. K. Kohse-Hoeinghaus and J.B. Jeffries, Taylor and Francis, NY, 2002, pp. 479-798.
42. J.B. Jeffries and K. Kohse-Hoeinghaus, "Continuing Developments," in *Applied Combustion Diagnostics*, ed. K. Kohse-Hoeinghaus and J. B. Jeffries, Francis and Taylor, New York, (2002), pp. 669-676.

## **MEETING MANUSCRIPTS 2001**

43. J.D. Koch and R.K. Hanson, "Ketone Photophysics for Quantitative PLIF Imaging," paper AIAA-2000-0413 at 39<sup>th</sup> Aerospace Sciences Meeting, Reno, NV, Jan. 2001.
44. T. Rossmann, M.G. Mungal, and R.K. Hanson, "High Compressibility Mixing Layer Studies in a Shock Tunnel Driven Facility," 23<sup>rd</sup> Int. Symp.on Shock Waves, Arlington, TX, July 2001.
45. T. Rossmann, M.G. Mungal, and R.K. Hanson, "Acetone PLIF and Schlieren Imaging of High Compressibility Mixing Layers," paper AIAA-2000-0290, at Aerospace Sciences Meeting, Reno, Jan. 2001.
46. W.G. Bessler, C. Schulz, T. Lee, J.B. Jeffries, and R.K. Hanson, "Laser Induced Fluorescence Detection of Nitric Oxide in High-pressure Flames with A-X (0,1) Excitation," paper 2001-239 at 2001 Joint Meeting of Combustion Institute, Oakland, CA, March 2001.
47. D.F. Davidson, D.C. Horning, M.A. Oehlschlaeger, and R.K. Hanson, "The Decomposition Products of JP-10," AIAA 01-3707 37<sup>th</sup> Joint Propulsion Conference, Salt Lake City, (2001).

## **MEETING MANUSCRIPTS 2002**

48. R.K. Hanson, "Advanced Laser Diagnostics for Reactive Flows," paper AIAA-2002-0196, 40<sup>th</sup> Aerospace Sciences Meeting, Reno, NV, Jan. 2002.
49. T. Lee, D. Shin, J.B. Jeffries, R.K. Hanson, W.G. Bessler and C. Schulz, "Laser Induced Fluorescence Detection of NO in Methane/Air Flames at Pressures between 1 and 60 bar," AIAA-2002-0399, 40<sup>th</sup> Aerospace Sciences Meeting, Reno, NV, Jan. 2002.
50. D.W. Mattison, S.T. Sanders, J.B. Jeffries and R.K. Hanson, "Diode-Laser Sensors for Pulse Detonation Engine Applications," AIAA-2002-0471, 40<sup>th</sup> Aerospace Sciences Meeting, Reno, NV, Jan. 2002.
51. L. Ma, S.T. Sanders, and R.K. Hanson, "Laser-based Fuel Diagnostics for Sensing and Control in Pulse Detonation Engines," paper AIAA-2002-0609, 40<sup>th</sup> Aerospace Sciences Meeting, Reno, NV, Jan. 2002.
52. C. Schulz, J. Gronki, J.D. Koch, D.F. Davidson, J.B. Jeffries, and R.K. Hanson, "Temperature-dependent absorption by CO<sub>2</sub>: Implications for UV diagnostics in high-temperature flames," Laser Applications to Chemical and Environmental Analysis, OSA Digest, (2002) FC2-1-3.

53. S.T. Sanders, J.B. Jeffries, J. Wang, and R.K. Hanson, "Wavelength-agile diode laser sensors for monitoring gas properties in harsh environments," *Laser Applications to Chemical and Environmental Analysis, OSA Digest*, (2002) SuB2-1-3.
54. W.G. Bessler, C.Schulz, D.I. Shin, T. Lee, J.B. Jeffries, and R.K. Hanson, "Strategies for NO Laser-Induced Fluorescence in Methane/Air Flames at Pressures between 1 and 60 bar," *Laser Applications to Chemical and Environmental Analysis, OSA Digest*, (2002) FB4-1-3.
55. L. Ma, S.T.Sanders, J.B.Jeffries, E.A. Romo, and R.K. Hanson, "Characterization and Control of Fuel Loading in Combustion Systems Using Diode Laser Sensors," Paper 33, Spring Meeting of the Western States Section of the Combustion Institute, La Jolla, CA.
56. J.D. Koch and R.K. Hanson, "3-Pentanone Photophysics for PLIF Applications: Temperature Dependences and Limitations," Paper 17, Spring Meeting of the Western States Section of the Combustion Institute, La Jolla, CA.
57. T. Rossmann, M.G. Mungal, and R.K. Hanson, "Character of Mach Wave Radiation and Convective Velocity Estimation in Supersonic Shear Layers," AIAA-2002-2571, at 8th AIAA/CEAS Aeroacoustics Conference, Breckenridge, CO, Jun 2002.
58. W.G. Bessler, C. Schulz, T. Lee, D.-I. Shin, M. Hofmann, J.B. Jeffries, J. Wolfrum, and R.K. Hanson, "Quantitative NO-LIF Imaging in High-Pressure Flames," in *Optical and Laser Diagnostics*, C. Arcoumanis and K.T.V. Grettan, Editors (Inst. of Physics, Bristol, PA, 2003) Vol. 177, pp 107-114; presented at 1<sup>st</sup> Int. Conf. on Optical and Laser Diagnostics (ICOLAD), City University, London, 12-16 Dec. 2002.
59. T. Rossmann, M.G. Mungal, and R.K. Hanson, "Laser-based Diagnostics and Scalar Imaging in High Compressibility Shear Layers," Symp. on Applications of Laser Diagnostics to Fluid Mechanics, Lisbon, July 2002.
60. J.B. Jeffries, S.T. Sanders, X. Zhou, L. Ma, D.W. Mattison, and R.K. Hanson, "Scanned Wavelength Diode-Laser Sensors for Harsh Environments," in "Diode Lasers and Applications in Atmospheric Sensing," A. Fried, ed. Proc. of SPIE, The International Society for Optical Engineering, Bellingham, WA, vol. 4817, 2002, pp. 88-95.

#### **MEETING MANUSCRIPTS 2003**

61. L. Ma, J.B. Jeffries, and R.K. Hanson, "Two Phase Fuel Diagnostic based on Diode Lasers," AIAA-2003-0401, 41th Aerospace Sciences Meeting, Reno, NV, Jan. 2003.

62. J.D. Koch and R.K. Hanson, "A Photophysical Model for 3-Pentanone PLIF: Temperature, Pressure and Excitation Wavelength Dependences," paper AIAA 2003-0403 at 41st Aerospace Sciences Meeting, Reno, NV, Jan. 2003.
63. T. Lee, J.B. Jeffries, R.K. Hanson, W.G. Bessler, and C. Schulz, "Quantitative NO LIF Imaging in High-Pressure Flames," AIAA-2003-0583, 41th Aerospace Sciences Meeting, Reno, NV, Jan. 2003.
64. D.W. Mattision, M.A. Oehlschlaeger, J.B. Jeffries, and R.K. Hanson, "Pulse Detonation Tube Characterization using Laser Absorption Spectroscopy," AIAA-2003-0713, 41th Aerospace Sciences Meeting, Reno, NV, Jan. 2003.
65. W.G. Bessler, T. Lee, C. Schulz, J.B. Jeffries, and R.K. Hanson, "Strategies for Quantitative NO Concentration and Temperature Measurements by NO LIF in High Pressure Flames," 3<sup>rd</sup> Joint Meeting of the US Sections of the Combustion Institute, Chicago, Ill, 2003.
66. W.G. Bessler, C. Schulz, T. Lee, J.B. Jeffries, and R.K. Hanson, "UV Laser Induced Fluorescence of Carbon Dioxide in High-Pressure Flames," 3<sup>rd</sup> Joint Meeting of the US Sections of the Combustion Institute, Chicago, Ill, 2003.
67. D.W. Mattision, M.A. Oehlschlaeger, J.B. Jeffries, and R.K. Hanson, "Pulse Detonation Tube Characterization Using Laser Absorption Spectroscopy," 39<sup>th</sup> AIAA/ASME/SAE/ASEE Joint Propulsion Conference, Huntsville, Al, 2003.
68. L. Ma, C.M. Brophy, D.W. Mattison, K.M. Hinckley, J.B. Jeffries, and R.K. Hanson, "Propane Fuel Monitoring in Pulse Detonation Engines Using a Diode-Laser Sensor," 39<sup>th</sup> AIAA/ASME/SAE/ASEE Joint Propulsion Conference, Huntsville, Al, 2003.
69. J.T.C. Liu, J.B. Jeffries, and R.K. Hanson, "Diode Laser Absorption Diagnostics for Measurements in Practical Combustion Flow Fields," 39<sup>th</sup> AIAA/ASME/SAE/ASEE Joint Propulsion Conference, Huntsville, Al, 2003.
70. D. W. Mattison, M. A. Oehlschlaeger, Z. C. Owens, E. A. Barbour, J. B. Jeffries, and R. K. Hanson, "UV Laser Diagnostics for Studies of Finite-Rate Chemistry in PDEs", 19th International Colloquium on the Dynamics of Explosions and Reactive Systems, Hakone, Japan, July 27 - August 1, 2003.

#### **MEETING MANUSCRIPTS 2004**

71. W.G. Bessler, H. Kronemayer, C. Schulz, T. Lee, J.B. Jeffries, and R.K. Hanson, "Quantitative Multi-Line NO-LIF Temperature Imaging in Flames over a Wide Pressure Range," presented at LACEA, Annapolis, Feb. 2004.
72. E. Barbour, M.A. Oelschlaeger, D.W. Mattison, D.F. Davidson, C. Schulz, J.B. Jeffries, and R.K. Hanson, "UV Absorption of CO<sub>2</sub> for Temperature Diagnostics," presented at LACEA, Annapolis, Feb. 2004.

73. J.T.C. Liu, J.B. Jeffries, and R.K. Hanson, "Wavelength Modulation Absorption Spectroscopy for Combustion Temperature Measurements using Multiplexed Near-Infrared Diode Lasers," paper AIAA-2004-0647 presented at 42<sup>nd</sup> Aerospace Sciences Meeting, Reno, NV, Jan. 2004.
74. T. Lee, J.B. Jeffries, R.K. Hanson, W.G. Bessler, and C. Schulz, "Carbon Dioxide UV Laser-Induced Fluorescence Imaging in High-Pressure Flames," paper AIAA-2004-0386 presented at 42<sup>nd</sup> Aerospace Sciences Meeting, Reno, NV, Jan. 2004.

### **INVITED LECTURES**

75. R. K. Hanson, "Laser Diagnostics for Combustion and Propulsion", Distinguished Lecture Series, University of Utah, February 20, 2001.
76. R. K. Hanson, "Diode Lasers for Combustion Sensing and Control", invited plenary lecture, Int. Conf. on Tunable Diode Laser Spectroscopy, Zermatt, Switzerland, July 9, 2001.
77. R. K. Hanson, "Advanced Laser Diagnostics for Reactive Flows", invited plenary lecture, Int. Conf. on Dynamics of Explosions and Reactive Systems, Seattle, WA, July 31, 2001.
78. R. K. Hanson, "Tunable Diode Laser Sensing for Combustion Monitoring and Control", invited plenary lecture, Joint (Japan/WSSCI) International Combustion Symposium, Kauai, Hawaii, Sept. 10, 2001.
79. J. B. Jeffries, Visiting Lecturer, (10 hour mini-course) "Laser-Based Diagnostics, Measurements, and Sensors for Applied Problems in Gas-Phase Reacting Flows," University of Bielefeld, November, 2001.
80. R.K. Hanson, "Advanced Laser Diagnostics for Combustion and Propulsion," University of Minnesota, December, 2002.
81. R.K. Hanson, "Advanced Laser Diagnostics for Combustion and Propulsion," University of Michigan, December, 2002.
82. J. B. Jeffries, "Laser Diagnostics and Combustion Kinetics," University of Heidelberg, August, 2003.
83. J. B. Jeffries, "Laser-Induced Fluorescence Imaging and Absorption Diagnostics for Combustion and Propulsion Applications," Ecole Centrale, Paris, September, 2003.
84. J. B. Jeffries, "Laser-Induced Fluorescence Imaging and Absorption Diagnostics for Combustion and Propulsion Applications," Cambridge University, October, 2003.



## 4.0 Personnel

Individual researchers partially or fully supported by the program during the reporting period are listed below. All the work has been carried out in the High Temperature Gasdynamics Laboratory, in the Department of Mechanical Engineering, under the supervision of Professor R. K. Hanson.

### Postdoctoral Research Associates

Jay B. Jeffries, Dong-Il Shin

### Graduate Research Associates

Brian Chung  
Brian Kirby  
Jon Koch  
Tonghun Lee  
Jonathan Liu  
Lin Ma  
Christopher Morris  
Gregory Rieker  
Tobias Rossmann  
David Rothamer  
Scott Sanders  
Jian Wang  
Michael Webber

### Ph.D Degrees Awards (2000-2003)

Brian Kirby, "Infrared Planar Laser-Induced Fluorescence Imaging and Applications to Imaging of Carbon Monoxide and Carbon Dioxide"

Christopher Morris, "Shock-induced combustion in high-speed wedge flows"

Tobias Rossmann, "An Experimental Investigation of High Compressibility Mixing Layers"

Scott Sanders, "Diode-Laser Sensors for Harsh Environments with Application to Pulse Detonation Engines"

Jian Wang, "New Strategies of Diode Laser Absorption Sensors"

Michael Webber, "Diode Laser Measurements of  $\text{NH}_3$  and  $\text{CO}_2$  for Combustion and Bioreactor Applications"

## 5.0 Significant Interactions

In addition to the interactions associated with the presentations and publications listed in Section 3 we have had numerous visitors to our laboratory during the contract period. Foreign visitors have come from Germany, China, United Kingdom, and Japan; industrial and national laboratory visitors have included representatives from:

### Industry:

- Aerometrics
- Boeing
- Horiba Instruments
- GE Research Laboratories
- Metrolaser
- Physical Sciences, Inc.
- Pratt and Whitney
- Rolls Royce
- TRW
- United Technologies
- Zolo Technologies

### Government

- Air Force Research Laboratory (WPAFB)
- Army Research Laboratories (ARL)
- NASA Ames
- NASA Lewis
- Sandia Livermore National Laboratory.

Also during this period, Professor Hanson has given invited presentations on AFOSR-sponsored diagnostics research to several industrial laboratories, universities, and government groups. Members of our group have provided technical information and advice, by telephone and mail, to several external researchers interested in duplicating or extending our diagnostics concepts.

### Transitions

Significant technical transitions of the combustion diagnostics developed under this program have occurred with several industrial and government scientists during the grant period. This work has primarily focused on the development of practical sensors using the tunable diode laser diagnostic strategies developed over the past decade at Stanford University. These significant technology transitions include:

Customer	Result	Application
Dr. Jeffery Lovett, Pratt and Whitney, East Hartford, CT (860)557-0559	Tunable diode laser diagnostics for gas temperature measurements	Sensor for temperature in Pratt combustor in sector-test rig at WPAFB
Dale T. Shouse, AFRL/PRTS, WPAFB, OH (937)255-4636	Tunable diode laser diagnostics for gas temperature measurements	Sensor for temperature in Pratt combustor in sector-test rig at WPAFB
Dr. James Gord, AFRL/PRTS, WPAFB, OH (937)255-7487	Planar laser-induced fluorescence of NO at high pressure	Diagnostics for GE vortex- stabilized combustor in sector- test rig at WPAFB
Dr. Michael Brown, ISSI, Dayton, OH (937)252-2706	Planar laser-induced fluorescence of NO at high pressure	Diagnostics for GE vortex- stabilized combustor in sector- test rig at WPAFB
Dr. T. Jenkins, MetroLaser, Irvine, CA (949)553-0688	Single diode laser diagnostic for gas temperature	Temperature sensor for industrial applications
Dr. Mark Allen PSI Corp Andover, MA (978)689-0003	Gas sensors based on tunable diode lasers using 2f techniques	Temperature sensors for practical industrial applications
Dr. Andrew Sappey Zolo Technologies Boulder, CO (303)604-5800	Wavelength-Multiplexed tunable diode laser sensor strategies	Temperature sensors for practical industrial applications
Dr. Michael Webber Pranalytica Inc Santa Monica, CA (310)458-2624	Gas sensors for NH <sub>3</sub> using tunable diode lasers	Sensors to monitor industrial refrigeration and agricultural feedlots
Dr. Campbell Carter AFRL/PR WPAFB Dayton, OH (937)255-7203	Wavelength-Multiplexed tunable diode laser sensor strategies	Sensors to monitor scramjet combustor ground test

## 6.0 Inventions

A patent disclosure was filed by Scott Sanders for an invention called "Enhanced wavelength-tuning of semiconductor lasers." This invention was supported in part by grant number F49620-01-1-0145 awarded by the Air Force Office of Scientific Research. The Stanford University patent office conducted a market survey for this invention and decided not to pursue a patent.

This invention relates to wavelength agile tuning of diode lasers to enable rapid wavelength scanned spectroscopic techniques for gas concentration and temperature measurements.

A patent disclosure was filed by Jonathan Liu, Jay Jeffries, and Ronald K. Hanson for an invention called "Method and Means for Temperature Measurements in Gases" This invention was supported in part by grant number F49620-01-1-0145 awarded by the Air Force Office of Scientific Research. The Stanford University patent office is currently evaluating financial market potential for this patent.

This invention relates generally to the use of wavelength modulated absorption spectroscopy techniques for gas temperature and concentration measurements and in particular presents a specific strategy to allow measurements of temperature and concentration when the spectra is congested and baselines to determine incident laser intensity are obscured. This occurs at high pressures because of pressure broadening as well as for large polyatomic molecular species such as hydrocarbon fuels. A crucial component of this disclosure is the realization that methods to determine temperature from ratios of wavelength modulation signals do not require the calibration normally used for single line wavelength modulation techniques.